

**UCSF**

**UC San Francisco Electronic Theses and Dissertations**

**Title**

Integration of Metabolic MR Spectroscopy for Improved Characterization and Clinical Management of Patients with Infiltrating Glioma

**Permalink**

<https://escholarship.org/uc/item/6tn0k7vk>

**Author**

Jalbert, Llewellyn

**Publication Date**

2015

Peer reviewed|Thesis/dissertation

Integration of Metabolic MR Spectroscopy for Improved Characterization and  
Clinical Management of Patients with Infiltrating Glioma

by

Llewellyn Jalbert

DISSERTATION

Submitted in partial satisfaction of the requirements for the degree of

DOCTOR OF PHILOSOPHY

in

Bioengineering



in the

GRADUATE DIVISION

of the

UNIVERSITY OF CALIFORNIA, SAN FRANCISCO

AND

UNIVERSITY OF CALIFORNIA, BERKELEY

Copyright 2015

By

Llewellyn Jalbert

*Dedicated to the many patients who have given their time, energy, patience & trust to participate in translational cancer research, without whom this work would not be possible. Thank you.*

## ACKNOWLEDGEMENTS

---

A Ph.D. takes a village and I have a large community of people to acknowledge that have helped me on my journey through graduate school. First and foremost, I would like to thank my graduate advisor and mentor **Sarah Nelson**. Sarah has been a role-model and an inspiration, and without her as a mentor I may never have pursued my Ph.D. Under her guidance, I've learned and grown immensely as a scientist and person. Along with Sarah, it's been an absolute honor to perform my graduate training alongside some of the finest scientists, physicians, and administrative staff there is. This section will highlight their individual contributions.

I would like to acknowledge the pivotal roles of **John Kurhanewicz** and **Susan Chang** in my graduate career. John and Susan served on both my qualifying exam and dissertation committees, and their advice and mentorship has been monumental in my research projects. Between John's depth of knowledge of translational nuclear magnetic resonance and Susan's expertise with neuro-oncology and patient care, I have been in incredibly skilled hands. They radiate warmth and wisdom, and they are true pioneers for the next wave of cancer imaging.

Throughout graduate school I feel incredibly lucky to have had **Dan Vigneron** in my corner as my academic advisor. His advice was critical in shaping my course-load every semester and in setting realistic goals for myself. I owe a special thank you to **Sabrina Ronen** for the opportunity to rotate in her laboratory, and for her guidance and training in tissue-culture and extraction techniques.

The degree of collaboration across departments at UCSF is phenomenal. I have many close collaborators to acknowledge including **Joanna Phillips, Christopher Hess, Joe Costello, Hikari Yoshihara, Annette Molinaro, Tracy McKnight, Brett Johnson,** and **Tali Mazor**. They each possess highly-specialized skill-sets and expertise as well as an enthusiasm to teach and share ideas. They have all made lasting contributions to these projects and my education, and give me hope in what feats can be accomplished when we work together to tackle large problems.

I would like to personally thank **Mary Mcpolin, Bert Jimenez,** and **Allison Fuller**. They taught me how to provide professional patient-care and emergency-support during scans, and every day were a genuine pleasure to work with. I would also like to extend my gratitude to all of the members of the **Margaret Hart Surbeck Laboratory for Advanced Imaging** for their many collaborations, fruitful scientific discussions, and shared laughs over the years, and for the technical support provided by **Jason Crane, Beck Olsen, Jed Chan,** and **Peter Storey**, which is above-and-beyond any that I have ever experienced.

I owe the other members of the **Brain Group** a heartfelt thank you for all of their guidance over the years, including **Yan Li, Eugene Ozhinsky, Angela Jakary, Emma Essock-Burns, Maryem Vareth, Wendy Ma, Tracy Luks, Aurelia Williams, Stojan Maleschlijski, Xiaowei Zou, Manisha Dayal, and Marisa Lafontaine**. I would like to personally thank **Adam Elkhaled** for the incredible dedication and work ethic he provides the group and the massive contributions he made to many of the NMR projects in this dissertation, as well as **Ilwoo Park** for teaching me how to work with the hyper-polarized instruments and analyze multi-nuclear spectroscopy. I would like to thank **Janine Lupo** and **Wei Bian** for the patience, education, and advice they provided to me

as a new researcher in the group. I would also thank **Evan Neill** for the statistical support and enthusiasm he provided to this work. Lastly, I would like to thank **Cathy Devine** for her wonderful and reliable administrative support.

Every Ph.D. also comes with a hefty and continuous amount of administrative work. I am very grateful to have had **SarahJane Taylor** and **Kristen Olsen** as incredible program administrators. It's unbelievable the level of support they are able to provide us, as well as how much they coordinate across the two campuses that positively contributes to our experience in the program.

This dissertation wouldn't be complete if I didn't extend my sincere gratitude to **Laurel Egenberger** and the **Center for Science & Engineering Education (CSEE)** for providing the educational internship opportunities that built my path to graduate school, as well as to **Ellie Blakely**, **Kathy Bjornstad**, and **Chris Rosen**. I will be forever grateful for their willingness to believe in me and take me in under their wing so early on in my scientific career.

While my professional life requires many acknowledgements, my personal community has several important people that I owe gratitude as well. My parents, **Lew** and **Teresa Jalbert**, have provided endless support and encouragement throughout graduate school. I count myself immensely fortunate to have them as my parents and role-models, and I am grateful for them every single day. I'd also like to thank my brother, **Jason Gorfine**, who I could always count on to have my back. Lastly, my partner **Caroline Sandifer** and close friend **Katherine Saviskas** are two incredibly special people that have been pillars of support and joy in my life. They continue to inspire me to grow as a person while bringing a level of vibrance, creativity, and happiness to my life that I never

knew was possible.

— — —

*Grant funding for this dissertation was provided by:*

NCI Brain Tumor SPORE grant, number P50CA097257, The UCSF Discovery Fellowship, Achievement Rewards for College Scientists (ARCS) Foundation, and the INDNJC Foundation.

The text of Chapter 3 is a reprint of the material as it appears in *Science Translational Medicine*:

A. Elkhaled\*, L.E. Jalbert\*, J. Phillips, H. Yoshihara, R. Parvataneni, G. Bourne, M. Berger, S.M. Chang, S. Cha, and S.J. Nelson. “Magnetic Resonance of 2-Hydroxyglutarate in *IDH1*-mutated Low-grade Gliomas”. *Science Translational Medicine*. 4, 116ra5 (2012). \*[equal contribution]



# Integration of Metabolic MR Spectroscopy for Improved Characterization and Clinical Management of Patients with Infiltrating Glioma

by

Llewellyn Jalbert

## ABSTRACT

---

The clinical paradigm for treating and monitoring cancer is evolving: an increasing number of targeted agents are available for treatment and, with them, an enhanced understanding of the genomic, epigenomic, and metabolic aspects of tumors. Novel, non-invasive imaging methods are required to keep pace with such advances and to allow for the personalization of treatment decisions based on the underlying features of the tumor. This is especially true for infiltrating gliomas, which are biologically heterogeneous in nature and highly complex in their clinical management.

Anatomic and functional magnetic resonance (MR) imaging is the clinical mainstay for monitoring patients with glioma, offering valuable information on the structural composition and vascularization of the tumor and surrounding tissue. Yet the decision of when to treat and which therapies to choose have remained controversial and have relied primarily on invasive neurosurgery, which carries significant risks to the patient.

MR spectroscopy is a powerful metabolic imaging technique that is capable of measuring the biochemical compounds present in tissue. This dissertation has investigated the utility of *in vivo* and *ex vivo* spectroscopic profiling to characterize a

large cohort of patients with recurrent glioma. The metabolic and physiological information obtained has provided critical insights as to the aggressiveness, histological subtype, and genotype of the tumors.

The results present in this dissertation strongly support the integration of MR spectroscopy into standard clinical protocols. The non-invasive and highly versatile nature of this approach would allow clinicians to better assess and manage this deadly disease. Most importantly, we hope that this study and others will ultimately improve the outcome and quality of life for these patients, as well as provide applications for other cancers.

# Table of Contents

<b>CHAPTER 1: INTRODUCTION</b> .....	<b>1</b>
<b>CHAPTER 2: BACKGROUND</b> .....	<b>4</b>
2.1 PRIMARY BRAIN TUMORS: FOCUS ON GLIOMAS .....	5
2.2 DIAGNOSIS AND HISTOPATHOLOGICAL GRADING.....	6
2.3 CLINICAL MANAGEMENT OF LOW-GRADE GLIOMAS .....	7
2.4 IDH1/2 MUTATIONS .....	8
2.5 2-HYDROXYGLUTARATE PRODUCTION AND TUMOR METABOLISM .....	10
2.6 EMERGING MOLECULAR CLASSIFICATIONS .....	11
2.7 MAGNETIC RESONANCE IMAGING AND SPECTROSCOPY .....	12
2.8 HIGH-RESOLUTION MAGIC ANGLE SPINNING.....	18
2.9 CLINICAL UTILITY OF MR SPECTROSCOPIC TECHNIQUES .....	20
2.10 REFERENCES.....	22
<b>CHAPTER 3: MAGNETIC RESONANCE OF 2-HYDROXYGLUTARATE IN IDH1- MUTATED LOW-GRADE GLIOMAS</b> .....	<b>26</b>
ABSTRACT .....	27
INTRODUCTION .....	27
RESULTS .....	29
<i>Characterization of patient population.....</i>	<i>29</i>
<i>Magnetic resonance spectroscopy of a 2HG phantom .....</i>	<i>33</i>
<i>Identification of 2HG ex vivo in tissue samples.....</i>	<i>34</i>
<i>Concordance of IDH1 mutation status and presence of 2HG .....</i>	<i>38</i>
<i>Levels of 2HG among tumor grades .....</i>	<i>39</i>
<i>Ex vivo correlations of 2HG.....</i>	<i>39</i>
<i>Tumor tissue histopathology and 2HG.....</i>	<i>42</i>
<i>In vivo correlations of ADC with 2HG.....</i>	<i>42</i>
DISCUSSION.....	45
MATERIALS AND METHODS .....	48
<i>Patient population .....</i>	<i>48</i>
<i>Preoperative MRI and spectroscopy .....</i>	<i>49</i>
<i>Postprocessing of preoperative MR exam .....</i>	<i>49</i>
<i>Image-guided brain tumor tissue sampling .....</i>	<i>50</i>
<i><sup>1</sup>H HR-MAS spectroscopy.....</i>	<i>50</i>
<i>Statistical analysis.....</i>	<i>52</i>
REFERENCES AND NOTES .....	53
ACKNOWLEDGMENTS .....	58
FUNDING SOURCES .....	58
AUTHOR CONTRIBUTIONS .....	58
SUPPLEMENTARY METHODS.....	58
<i>Histopathology and IDH1 immunohistochemistry .....</i>	<i>59</i>
<i>Tumor vascularity.....</i>	<i>60</i>
<i>Genetic sequencing .....</i>	<i>60</i>
<i>In vivo post-processing of ADC data.....</i>	<i>61</i>
<i>J-resolved spectroscopy and spectral simulation of 2HG in phantom .....</i>	<i>62</i>
<i>Ultra-high magnetic field applied to the separation of 2HG <math>\beta</math>-resonances.....</i>	<i>62</i>
SUPPLEMENTARY FIGURE AND TABLE LEGENDS.....	63

SUPPLEMENTARY REFERENCES.....	65
SUPPLEMENTARY FIGURES AND TABLES .....	66
<b>CHAPTER 4: MAGNETIC RESONANCE ANALYSIS OF MALIGNANT TRANSFORMATION IN RECURRENT GLIOMA.....</b>	<b>74</b>
ABSTRACT .....	75
INTRODUCTION .....	76
MATERIALS AND METHODS .....	77
<i>Patient accrual</i> .....	77
<i>In vivo multimodal MR imaging and spectroscopy</i> .....	78
<i>Post processing of MR exam</i> .....	79
<i>Tissue sample acquisition</i> .....	80
<i>Histopathology and IDH-analysis</i> .....	80
<i>Analysis of MR parameters</i> .....	82
<i>Heatmap generation</i> .....	84
<i>Statistical analysis</i> .....	84
RESULTS .....	85
<i>Characterization of patient population with recurrent LGG</i> .....	85
<i>Findings from the pre-surgery anatomic MR images</i> .....	87
<i>Findings from the pre-surgery diffusion weighted MR images</i> .....	89
<i>Findings from the pre-surgery perfusion weighted MR images</i> .....	90
<i>Findings from pre-surgery spectroscopic imaging data</i> .....	91
<i>Multivariate analysis of imaging parameters</i> .....	94
<i>Differences in histopathological parameters with grade and sub-type</i> .....	94
<i>Correlation of histopathology and in vivo imaging parameters</i> .....	96
DISCUSSION.....	99
FUNDING SOURCES .....	101
ACKNOWLEDGEMENTS .....	101
REFERENCES.....	101
SUPPLEMENTARY FIGURE AND TABLE LEGENDS.....	104
SUPPLEMENTARY FIGURE AND TABLES .....	105
<b>CHAPTER 5: METABOLIC PROFILING OF MALIGNANT TRANSFORMATION AND IDH-MUTATION IN DIFFUSE INFILTRATING GLIOMAS .....</b>	<b>108</b>
ABSTRACT .....	109
INTRODUCTION .....	109
METHODS .....	111
<i>Patient population</i> .....	111
<i>Presurgical In vivo MR imaging and spectroscopy</i> .....	112
<i>Post processing of MR data</i> .....	112
<i>Tissue sample acquisition</i> .....	113
<i>Histopathology and IDH-analysis</i> .....	114
<i>Ex vivo HR-MAS spectroscopy</i> .....	116
<i>Heatmap generation</i> .....	117
<i>Statistical Analysis</i> .....	117
RESULTS .....	118
<i>Characterization of the patient population</i> .....	118
<i>Metabolic differences associated with MT and IDH-mutation</i> .....	118
<i>Correlation of 2HG with metabolite levels and histopathology parameters</i> .....	121
DISCUSSION.....	124

REFERENCES.....	127
ACKNOWLEDGEMENTS .....	130
FUNDING SOURCES .....	131
SUPPLEMENTARY FIGURE CAPTIONS .....	131
SUPPLEMENTARY FIGURES.....	132
<b>CHAPTER 6: SUMMARY .....</b>	<b>134</b>

## List of Figures

Figure 2.1: Mutant IDH enzymatics.....	9
Figure 2.2: Diagram of spin magnetization after excitation.....	14
Figure 2.3: Anatomic T <sub>1</sub> and T <sub>2</sub> imaging of recurrent glioma.....	15
Figure 2.4: <sup>1</sup> H NMR spectrum of a low-grade glioma.....	17
Figure 2.5: Diagram of HR-MAS spectroscopy.....	19
Figure 3.1: Designation of tissue targets from presurgical <i>in vivo</i> imaging.....	33
Figure 3.2: IDH1 <sub>R132H</sub> immunostaining and direct sequencing of <i>IDH1</i> gDNA.....	36
Figure 3.3: <i>Ex vivo</i> spectra from mutant and WT <i>IDH1</i> tissue samples.....	37
Figure 3.4: 2HG levels according to WHO glioma grade.....	41
Figure 3.S1: <i>J</i> -coupling constants and spectral simulation of 2HG.....	66
Figure 3.S2: Separation of 2HG $\gamma$ -resonances at ultrahigh field strength.....	67
Figure 3.S3: Plots of 2HG correlations with <i>ex vivo</i> metabolites, histopathology, and <i>in vivo</i> MR imaging parameters.....	68
Figure 4.1: Multimodality MR imaging exam of a subject with a recurrent LGG that had undergone MT.....	89
Figure 4.2: Differences in lesions that had undergone malignant transformation.....	91
Figure 4.3: Heatmaps of volumetric MR parameters and clinical outcome of recurrent LGG.....	93
Figure 4.4: Heatmap of image-guided tissue samples.....	95
Figure 4.5: Network linkage map of histopathology and advanced imaging of image guided tissue samples.....	98
Figure 4.S1: Multivariate logistical regression model of malignant transformation.....	105

Figure 5.1: Flow diagram of metabolite differences associated with MT and <i>IDH</i> -mutation status.....	121
Figure 5.2: Averaged HR-MAS spectral profile from individual histological grades and <i>IDH</i> -mutation status.....	122
Figure 5.3: Metabolic spectral heatmap across histological grades.....	123
Figure 5.S1: Flow diagram of metabolite differences between astrocytoma and oligodendroglioma subtypes within histological grades.....	132
Figure 5.S2: Correlation scatterplots of 2HG levels with other metabolites and histopathological measures.....	133

## **List of Tables**

Table 3.1: Glioma patient population by tumor grade and histological subtype.....	31
Table 3.2: Classification of 2HG presence and IDH1 mutation status.....	38
Table 3.3: 2HG correlations with <i>ex vivo</i> metabolites, histopathology parameters, and <i>in vivo</i> diffusion parameters.....	44
Table 3.S1: Complete patient data for 2HG presence and IDH1 mutation status.....	69
Table 3.S2: Correlation statistics including an additional statistical method.....	73
Table 4.1: Recurrent LGG pre-surgical scans organized by grade and histopathological subtype.....	87
Table 4.S1: MR intensity and volumetric parameters for malignant transformation and <i>IDH</i> -mutation in recurrent LGG.....	106
Table 4.S2: Correlations of <i>in vivo</i> imaging of tissue sample targets.....	107
Table 5.1: Recurrent LGG patient and tissue sample population by grade, histological subtype, and <i>IDH</i> -mutation status.....	120
Table 5.2: Metabolite and histopathology correlations with 2HG levels.....	124



## CHAPTER 1: Introduction

---

Infiltrating gliomas are a diffuse class of malignant brain tumors with a wide range of clinical outcomes. In contrast to primary glioblastoma multiforme (GBM), which has an estimated median overall survival (OS) of 15 months under the current treatment management, patients diagnosed with a low-grade glioma (LGG) can survive for years or even decades. Considering that patients have a relatively long survival, a balance is often struck between treating the tumor and impacting quality of life. Yet the decision of when to treat and which therapies to choose have remained controversial and have relied primarily on invasive surgery, which carries significant risks to the patient.

The recent discovery of mutations in the *isocitrate dehydrogenase 1 & 2 (IDH1/2)* oncogenes has shifted the paradigm for patients with LGG. These mutations were present in upwards of 70-80% of lesions and provide a significant survival advantage over their wild-type counterparts. *IDH*-mutations were also found to produce millimolar concentrations of the oncometabolite 2-hydroxyglutarate (2HG), which disrupts a variety of processes in the cell. Several novel therapies targeting this pathway are currently in the testing pipeline and will require additional advanced imaging techniques to better monitor these patients.

As scientists work to unveil the distinct biological subclasses of infiltrating gliomas, the development of non-invasive imaging techniques that can better diagnose and characterize lesions has become a significant priority. Anatomic and functional magnetic

resonance (MR) imaging is the primary method for monitoring patients with glioma, offering valuable information on the structural composition and vascularization of the tumor and surrounding tissue. In terms of providing physiological information regarding the tumor, however, it is limited. For interrogating the biochemical profiles, scientists have more recently turned to utilizing MR spectroscopy, a powerful metabolic imaging technique that is capable of measuring the compounds present in tissue.

This dissertation has investigated the utility of *in vivo* and *ex vivo* spectroscopic profiling to characterize a large cohort of patients with recurrent glioma in a clinical setting. The goal of this project was to develop and apply advanced physiological imaging techniques to enhance our understanding of this devastating disease, and provide valuable biomarkers and metabolic information that can be used for improved patient care. This dissertation is organized into three major projects.

In **Chapter 2**, I review the background material necessary for fully understanding these studies. The chapter begins by discussing the current clinical paradigm and challenges surrounding brain tumor management. *IDH*-mutated glioma physiology is reviewed within the context of the known molecular subtypes of glioma. I close this chapter with a discussion of the fundamental physics concepts of magnetic resonance imaging and spectroscopy and their current applications to studying cancer.

**Chapter 3** describes a study that investigated the feasibility of using magnetic resonance spectroscopy for imaging 2HG as a novel biomarker for *IDH*-mutations. We used 1D and 2D high-resolution magic angle spinning (HR-MAS) spectroscopy to investigate the spectral profiles of patients with recurrent LGG, and discovered the

presence of 2HG and with it a strong concordance with the *IDH*-mutated genotype. We further characterized the magnetic resonance spin-system associated with 2HG and found several metabolite, histopathology, and *in vivo* imaging correlations with 2HG levels. These results provided extensive information regarding the MR spectroscopy imaging of 2HG and laid the necessary groundwork for development of future *in vivo* sequences.

**Chapter 4** is a highly collaborative project that explored the *in vivo* imaging and histopathological features of LGG that had undergone malignant transformation (MT) to higher grade lesions. We performed advanced volumetric and intensity imaging analysis at the lesion and tissue sample level, and developed multi-variate logistical regression models based on these findings that were able to predict MT. We further utilized bioinformatic heatmap and network analyses to visualize these complex datasets and better our understanding of recurrent LGG and the pathological process of malignant transformation.

Building on the prior chapter, **Chapter 5** presents a project that focused on obtaining and analyzing the *ex vivo* metabolic profiles of image-guided tissue samples using HR-MAS. We interrogated the spectral patterns associated with MT and the *IDH*-mutated genotype and found distinct spectral profiles for individuals grades of recurrence as well as the *IDH*-mutated and wild-type genotypes. We additionally found correlations between 2HG levels and several brain tumor metabolites and measures of mitosis. Taken together, these results provide improved characterization of the physiological changes related to MT and *IDH*-mutated lesions, which could be integrated into routine clinical practice.

## CHAPTER 2: Background

---

This chapter provides an overview of malignant gliomas with an emphasis on recurrent, low-grade glioma (LGG) and clinical management of the disease. Magnetic Resonance (MR) Imaging and Spectroscopy are introduced as methods for non-invasively diagnosing and monitoring patients with low-grade glioma. Advanced spectroscopic imaging techniques are introduced as an additional methodology for further characterizing lesions based on underlying genomic and physiological differences in the tumor. Lastly, the utility of these techniques in providing improved patient care is discussed within the context of the current clinical paradigm.

---

## **2.1 Primary Brain Tumors: Focus on Gliomas**

Recent estimates have shown that approximately 222 of every 100,000 people living in the United States (U.S.) have been diagnosed with a primary brain tumor. While most of these lesions are non-malignant in nature, approximately 34% of these lesions are malignant. Despite decades of research devoted to these diseases large morbidity and mortality rates are still present, and it is estimated that 13,770 people will die as a result of a primary malignant tumor of the CNS in 2015 [1].

Infiltrating gliomas comprise 80% of malignant lesions and consist of transformed glial cells, primarily astrocytes and oligodendrocytes. Glial cells make up an overwhelming 90% of the cell population of the brain, and play many critical functions including neuronal and extracellular matrix remodeling, neurotransmitter and ion balance, cerebral spinal fluid production, neuronal myelination, as well as response to injury and pathogens [2]. Tumors arising from these cell populations are characterized by their infiltrative nature and are difficult to fully resect by neurosurgery. As a result, infiltrating gliomas are invariably fatal, although patients have a wide range of different clinical manifestations of their disease [3].

## **2.2 Diagnosis and Histopathological Grading**

Primary brain tumors are diagnosed through the histopathological assessment of tissue obtained during neurosurgical resection or biopsy. Malignant gliomas span three distinct histopathological grades as defined by the World Health Organization: low-grade gliomas (LGGs, WHO Grade II) are characterized by increased cellularity, nuclear atypia, and minimal or no mitosis; anaplastic gliomas (WHO Grade III) share similar features as Grade II tumors, but with increased mitotic figures; glioblastoma multiforme (GBM, WHO Grade IV), are characterized by elevation of features of Grades II and III lesions, with the addition of complex neovascularization or necrosis [3]. GBM are the most malignant subtype, and can either arise from lower-grade lineages as a secondary lesion, or occur *de novo* as a primary lesion [4]. There have been extensive studies of primary GBM; the focus of this dissertation will be primarily based on tumors derived from LGG ancestry, which have received less attention from the research community.

### **2.3 Clinical Management of Low-grade Gliomas**

The standard-of-care for patients with a low-grade glioma consists of maximal surgical resection. Depending on the extent of resection, this may be followed by active surveillance, cytotoxic chemotherapy and fractionated radiation therapy [5]. In contrast to primary GBM, which has an estimated median overall survival (OS) of 15 months under the current clinical paradigm, patients diagnosed with a WHO Grade II glioma can survive for years or even decades [6,7]. Because of the relatively long survival, a balance is often struck between treating the tumor and impacting quality of life. More aggressive treatments are often reserved for lesions that recur after undergoing malignant transformation (MT) to an anaplastic glioma or secondary GBM [8]. Unfortunately, there has been a significant lack of diagnostic and prognostic biomarkers that are able to non-invasively assess MT and stratify clinical outcome.

## **2.4 IDH1/2 Mutations**

In 2009, Yan et al. discovered novel missense mutations in the *isocitrate dehydrogenase 1 & 2 (IDH1/2)* oncogenes. These mutations were present in upwards of 70-80% of lesions that arise from low-grade lineage and conferred a significant survival advantage over wild-type tumors [9]. Interestingly, *IDH1/2* mutations were found to be conserved across mutually exclusive pathways of *TP53* mutation and 1p19q chromosomal loss and have been implicated as the earliest known mutation event in gliomagenesis [10]. Given the limited therapeutic options available for LGGs, *IDH*-mutations have garnered significant attention as a targetable therapeutic pathway with several novel therapies on the horizon and in clinical trials [11-13].

The *IDH1/2* genes natively encode the isocitrate dehydrogenase (IDH) enzymes required for the decarboxylation of isocitrate to  $\alpha$ -ketoglutarate in several locations in the cell. *IDH1* is situated at codon R132, and controls the enzymatic binding and subsequent conversion of isocitrate in the cytosol; while *IDH2* governs the homologous region of mitochondrial DNA at R172, and plays a critical role in the enzymatic activity of the mitochondria [9].

The heterozygosity of *IDH*-mutations results in an amino-acid substitution at one of two enzymatic active sites, most commonly arginine to histidine, creating a wild-type and mutant heterodimer as diagrammed in **Figure 2.1**. The wild-type position continues the production of  $\alpha$ -ketoglutarate, while the mutant portion develops the gain-of-function ability to further convert  $\alpha$ -ketoglutarate to D-2-hydroxyglutarate (2HG), an otherwise scarce metabolite in normal cells [14]. 2HG accumulates to milli-molar concentrations in



*IDH*-mutant tumors and has profound affects on the epigenetic landscape and processes within the cell [15].

Figure 2.1 Mutant IDH enzymatics

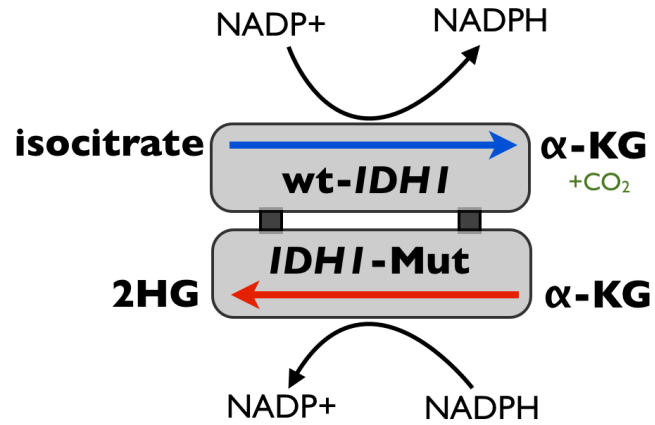


**Figure 2.1** *IDH1/2* mutations produce a wild-type and mutant heterodimer, with the gain-of-function ability to produce D-2-hydroxyglutarate (2HG).

## **2.5 2-Hydroxyglutarate Production and Tumor Metabolism**

The ability of 2HG to disregulate the cell is in large part due to the similarity in chemical structure to  $\alpha$ -ketoglutarate, which allows it to competitively inhibit  $\alpha$ -ketoglutarate dependent dioxygenases. These enzymes include those that control epigenetic modification of the DNA and histone proteins, as well as collagen synthesis and maturation. More specifically, 2HG interferes with TET-driven demethylation of cytosine residues of the DNA, resulting in a distinctive CpG island hypermethylation pattern. Beyond the DNA itself, competitive inhibition of the Jumonji C (JmjC)-domain-containing histone demethylases disrupts histone methylation, impacting both chromatin structure and regulation of the cellular transcriptome [15].

Microenvironment changes have also been observed with the inhibition of prolyl hydroxylases (PHDs) and lysyl hydroxylases (LHDs) by 2HG. This process leads to post-translational modifications of collagen, which can affect extracellular matrix stiffness and create endoplasmic reticulum (ER) stress [15]. Considering that the interaction between the ECM and tumor cells has been shown to influence progression in glioma [16], this could also contribute to mutant-*IDH* pathophysiology, albeit in unknown ways.

Additionally, PHD inhibition may also impact the glycolytic pathway of hypoxia-inducible factor (HIF-1), although this is still a matter of debate [17].

## **2.6 Emerging Molecular Classifications**

Evaluation of infiltrating gliomas based on histopathological assessment has proved insufficient for fully stratifying outcome and guiding treatment. While ~95% of primary GBM are wild-type for *IDH1/2*, approximately 20-30% of Grade II and Grade III lesions are *IDH* wild-type and have a distinctly more aggressive disease course than their mutated counterparts [18]. *IDH1/2* mutated lesions with an astrocytic lineage are commonly characterized by mutations in *TP53* and *alpha thalassemia/mental retardation syndrome X-linked (ATRX)*, while oligodendroglial tumors are marked by co-deletion of the 1p and 19q chromosomal arms that results from unbalanced translocation. *IDH*-mutant oligodendroglial tumors with 1p19q loss also often take secondary mutational hits in the tumor suppressor genes *CIC* and *FUBP1* [18]. As with many other cancers, for gliomas to conserve their replicative potential they require mechanisms to maintain their telomere length. Astrocytomas effectively lengthen their telomeres through *ATRX* mutation, while oligodendrogliomas achieve this through activating mutations in the *telomerase reverse transcriptase (TERT)* promoter region of their DNA [19, 20].

Recent molecular classifications based on variations in *IDH1/2* mutation, co-deletion of the 1p and 19q chromosomal arms, and mutation of the *TERT* promoter are now better able to predict overall survival (OS) than WHO histological grade [21]. As scientists work to unveil the distinct biological subclasses of infiltrating gliomas, the availability of non-invasive imaging techniques that can better diagnose and characterize lesions is of significant clinical interest. The subsequent chapters of this dissertation will focus on these techniques.

## **2.7 Magnetic Resonance Imaging and Spectroscopy**

Magnetic Resonance (MR) imaging and spectroscopy are an integral component of the non-invasive assessment of malignant brain tumors, owing primarily to the high soft tissue contrast in the brain and abundance of measurable metabolites. Within an MR imaging exam, many different modalities may be employed to obtain morphological and physiological information regarding the tumor lesion. In the context of brain tumor imaging, these MR modalities include: diffusion weighted imaging (DWI), which provides cellularity information due to differential brownian motion of water molecules [22]; gadolinium contrast enhanced perfusion weighted imaging (PWI), which provides an assessment of tumor neovascularization through dynamic rates of contrast leakage [23]; and spectroscopic imaging (MRSI), which provides spatially localized metabolic and chemical information [24]. Considering that DWI and PWI are becoming more routinely used in the clinic, the focus of this dissertation will be on metabolic spectroscopic imaging that requires a more detailed understanding of the MR physics involved.

Nuclear spin is an intrinsic quantum mechanical property of baryonic matter. Particles with half-integer spin constitute a class of particles known as fermions, which can either be elementary or composite in nature and are characterized by net angular momentum. Protons and neutrons are composite fermions, as well as nuclei comprised by an odd number of them, such as  $^1\text{H}$ ,  $^{13}\text{C}$ , and  $^{31}\text{P}$  [25]. When placed in an external magnetic field ( $B_0$ ), spin  $\pm 1/2$  nuclei will align with  $B_0$  and undergo precession at the Larmour frequency ( $\omega$ ), which is dependent on the gyro-magnetic ratio ( $\gamma$ ) of the nuclei (42.58 MHz/T for  $^1\text{H}$  proton) as well as the magnetic field strength, and is defined by the equation:

$$B_0 = \omega \gamma \quad (\text{Eq. 2.1})$$

Two discrete energy states are observed with regard to the direction of the magnetic field, one parallel (+1/2) and one antiparallel (-1/2), with the energy difference ( $\Delta E$ ) described by equation 2.2, where  $h$  is Plank's Constant ( $6.626 \times 10^{-34} \text{ m}^2\text{kg/s}$ ).

$$\Delta E = h/2\pi \cdot \gamma B_0 \quad (\text{Eq. 2.2})$$

When assessing the entire spin population in the system, more spins are aligned in the lower energy, parallel spin +1/2 state as defined by:

$$+1/2 / -1/2 = \exp(-\Delta E / kT) \quad (\text{Eq. 2.3})$$

where  $T$  is absolute temperature in Kelvin and  $k$  is Boltzmann's constant ( $1.381 \times 10^{-23} \text{ J} \cdot \text{K}^{-1}$ ). This results in a macroscopic net polarization of spin states, which can be perturbed using a transverse radio-frequency (RF,  $B_1$ ) pulse at the Larmour frequency:

$$f = \gamma/2\pi \cdot B_0 \quad (\text{Eq. 2.4})$$

In the classical regime, the application of a  $B_1$  pulse will tip the net magnetization vector away from  $B_0$ , at which point the transverse component of magnetization ( $M_{xy}$ ) will decay as  $\exp(-\tau/T_2)$ , while the longitudinal component ( $M_z$ ) will recover as  $1 - \exp(-\tau/T_1)$ , where  $\tau$  is time and  $T_2/T_1$  are the transverse and longitudinal relaxation constants, respectively. During the relaxation process, signal is obtained from surrounding receiver coils in the form of a free induction decay (FID) and is diagrammed in **Figure 2.2**.

**Figure 2.2 Diagram of spin magnetization after excitation**

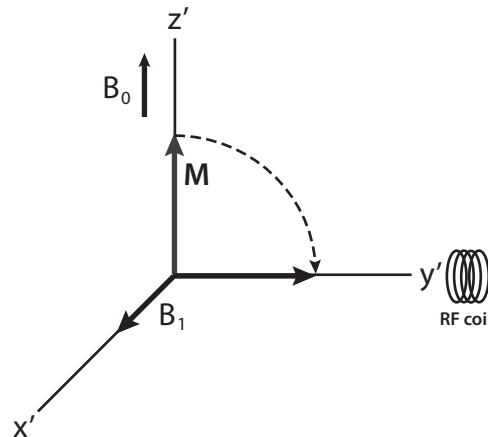


**Figure 2.2** This diagram is in the rotating frame at the Larmour frequency. After the transverse radio-frequency ( $B_1$ ) pulse is applied, the net magnetization vector ( $M$ ) tips into the x-y plane. As it recovers following  $T_1$  and  $T_2$ , signal is received through nearby RF coils.

$T_2$  is the spin-spin relaxation constant and governs the process by which  $M_{xy}$  is lost through interactions with neighboring spins, and is defined as the time in which it takes for to decay to 36.8% of its original magnetization:

$$M_{xy}(\tau) = \exp(-\tau/T_2) \quad (\text{Eq. 2.5})$$

$T_1$  is the spin-lattice relaxation constant that described the rate at which  $M_z$  recovers after excitation, due to the energy from the spins being dissipated into the surrounding environment as thermal energy, and is defined as the time in which it takes  $M_z$  to recover 63.2% of it's original magnetization:

$$M_z(\tau) = 1 - \exp(-\tau/T_1) \quad (\text{Eq. 2.6})$$

The relaxation constants  $T_1$  and  $T_2$  vary depending on their environment (e.g. grey matter versus white matter in the brain) and hold particular significance in MR imaging field, as they form the basis of generating tissue contrast within an MR image and highlighting pathology in the brain, as shown in **Figure 2.3** [25]. Based on the high natural abundance of water in the human body, the signal received and images generated

**Figure 2.3 Anatomic  $T_1$  and  $T_2$  imaging of recurrent glioma**

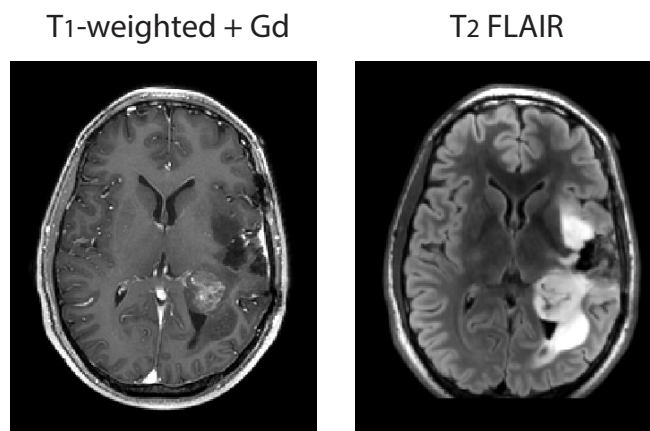


**Figure 2.3** Different types of anatomic images provide distinct functional information based on underlying tumor pathology.  $T_1$ -weighted imaging combined with paramagnetic gadolinium (Gd) contrast provides information regarding the integrity of the blood brain barrier, often compromised by infiltrative tumor, as well as to the extent of neovascularization and necrosis, which are hallmarks of higher-grade histologies.  $T_2$ -weighted imaging provides information as to the rough location and extent of a lesion, loosely demarcated by the hyper-intense signal produced a combination of tumor, edema and gliosis.

during an MR exam is predominantly from water protons, however signal from many other chemicals and metabolites is also present. Fortunately, this valuable physiological information can be discerned using MR spectroscopic techniques.

Distinguishing physiological metabolites and chemicals present within the tissue requires an understanding of the nuclear magnetic resonance (NMR) concept of chemical shift.

The electron cloud that surrounds a given nucleus provides varying levels of shielding from the external  $B_0$  field based on its own distinct chemical environment. Nuclei with

different levels of shielding therefore have different Larmour frequencies and will produce absorption lines at corresponding locations along the NMR spectrum, an example of which is shown in **Figure 2.4** and is defined by:

$$\omega_{\text{eff}} = \omega_0 (1 - \sigma) \quad (\text{Eq. 2.7})$$

where  $\omega_{\text{eff}}$  and  $\omega_0$  are the effective and unshielded Larmour frequency, respectively, and  $\sigma$  is the shielding constant for the chemical environment of a given proton.

The spectral signature of a given metabolite is largely determined by the Larmour frequency as well as a process known as scalar, J-coupling. While other effects such as dipole-dipole coupling are also observed, their impact is less evident in brain tumor  $^1\text{H}$  NMR and *in vivo* MRSI and beyond the scope of the projects in dissertation.

J-coupling is a mechanism by which energy is transferred primarily through bonding electrons to neighboring spins, resulting in distinct spectral splitting patterns. These spin-spin interactions are defined by field-independent J-coupling constants and fall into two major categories: weakly-coupled spins, whereby the magnitude of the Larmour frequencies are much larger than the magnitude of the J-coupling constants of the corresponding spins; and strongly-coupled spins, which are characterized by coupling constants on the order of the Larmour frequencies and produce highly elaborate absorption spectra. Weak coupling can be further broken down into two subcategories: simple coupling, whereby the subspectra split by neighboring spins share the same value J-coupling constant; and complex coupling, in which multiplets will have more complicated spectra produced through unequal J-coupling constants [25]. Given the field dependence of the Larmour frequency and it's relationship with J-coupling processes, understanding of these concept is critical for interpreting spectra at different field



strengths, and allow us to bridge the spectral information gleaned from high-field NMR systems to clinical field strength patient scanners.

**Figure 2.4**  $^1\text{H}$  NMR spectrum of a low-grade glioma

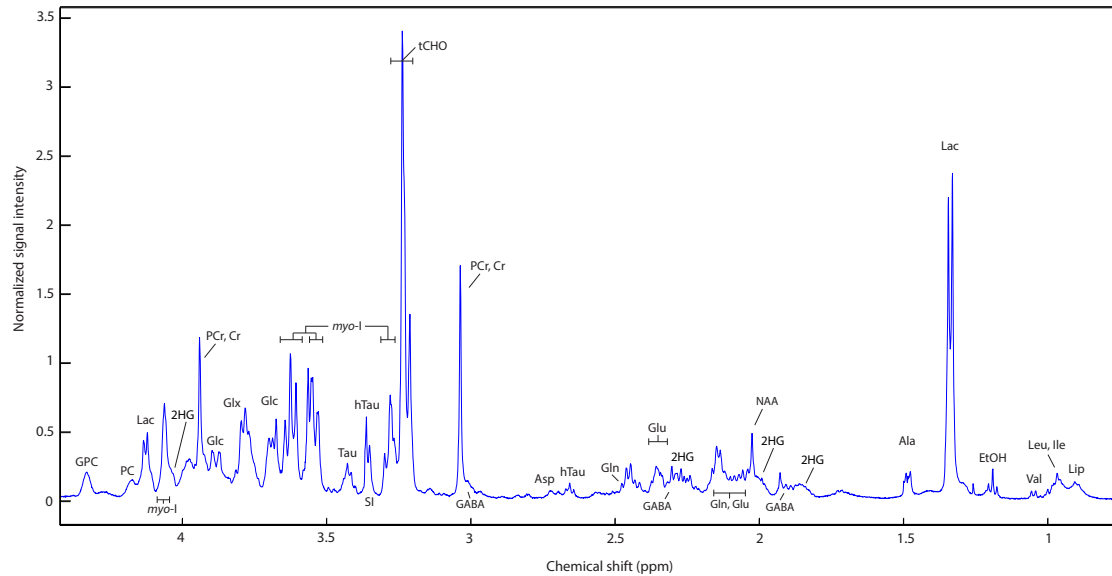


**Figure 2.4:** The NMR spectral profile of a LGG is characterized by several metabolites that are associated with physiological processes in the tumor cells. Depending on the chemical environment of the protons within these molecules, they will resonate at corresponding locations along the NMR spectrum. Abbreviations: GPC, glycerylphosphocholine; PC, phosphocholine; Lac, lactate; 2HG, 2-hydroxyglutarate; PCr, phosphocreatine; Cr, creatine; Glc, glucose; Glx, combination of Glu, Gln, and GABA; myo-I, Myo-inositol; Tau, taurine; hTau, hypo-taurine; tCho, total choline; GABA, gamma-amino-butyric-acid; Asp, aspartate; Gln, glutamine; Glu, glutamate; NAA, n-Acetyl-aspartate; Ala, alanine; etOH, ethanol; Val, valine; Leu, Leucine; Ile, isoleucine; Lip, lipid

## **2.8 High-resolution Magic Angle Spinning**

Ultra-high field strength NMR scanners are capable of probing the chemical compositions of solid state materials, solutions and biological tissue samples. Traditionally, analysis of tissue samples is complicated by significant broadening effects caused by dipolar coupling. The direct interaction between two magnetic dipoles depends on the relative position of the two nuclei, which exhibit partial alignment in tissue and therefore have residual dipolar coupling. However, the dipole interactions depend on the angle ( $\theta_{jk}$ ) between the internuclear vector and static field and are equal to zero when the following equation is satisfied:

$$2\cos^2(\theta_{jk}) - 1 = 0 \quad (\text{Eq. 2.8})$$

The solution of which yields what is referred to in NMR as the magic angle ( $\theta_{\text{magic}}$ ),

$$\theta_{\text{magic}} = \arctan(\sqrt{2}) \cong 54.74^\circ \quad (\text{Eq. 2.9})$$

Mechanically rotating a tissue sample at  $54.74^\circ$  with respect to the static magnetic field, as demonstrated in **Figure 2.5**, conveniently removes spin interaction effects [26]. This results in a solid-state signal that can achieve the narrow spectral linewidth commonly associated with solution-state NMR. This technique is known as High-resolution Magic Angle Spinning (HR-MAS) and is a powerful tool for investigating biological properties of tissue. Several chapters of this dissertation will highlight the utility of HR-MAS in interrogating brain tumor metabolism using *ex vivo* tissue samples.

**Figure 2.5 Diagram of HR-MAS spectroscopy**

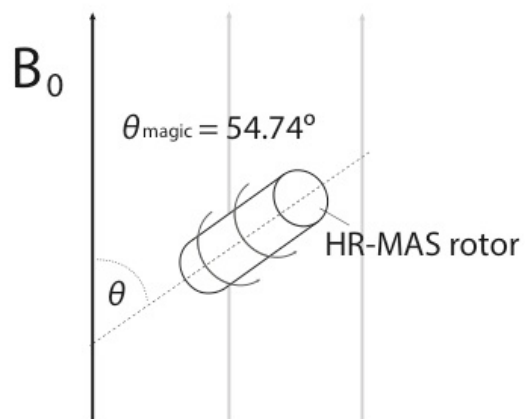


**Figure 2.5:** HR-MAS is performed by rotating the NMR sample at 54.74 degrees from the  $B_0$  field and yields narrow linewidth in solid-state samples.

## **2.9 Clinical Utility of MR Spectroscopic Techniques**

To fully appreciate the depth of physiological information provided by MR spectroscopy, we must first explore the fundamental biological differences of brain tumors that can be exploited in the context of imaging. Foremost, while non-cancerous cells derive their energy through oxidative phosphorylation, cancer cells undergo a biological process known as aerobic glycolysis, or more commonly as the Warburg effect [27]. This process is less efficient in terms of ATP production, however it achieves a tumor-promoting acidification of the extracellular pH through the production and export of lactate (Lac) [28]. Glutaminolysis serves as another important energy pathway for cancer cells through the production of glutamate (Glu), which acts as an additional energy source and stimulates cancer cell growth [29, 30]. Glycolysis and glutaminolysis both serve as critical energy production pathways for cancer metabolism that can be imaged using advanced MR spectroscopy techniques [31, 32].

Many additional compounds present in both tumor cells and normal brain tissue can be used to distinguish cancer from healthy tissue. The choline containing compounds phosphocholine (PC), glycerylphosphocholine (GPC), and free choline (Cho) are the building blocks and breakdown products of the phospholipid bilayer of the cell. In actively proliferating cancer cells, these compounds are elevated compared to normal tissue and function as an MR spectroscopy marker of viable tumor [33]. N-acetyl-aspartate (NAA) is a highly abundant molecule found in normal neuronal cell bodies and has many roles including maintaining osmolyte balance and neurotransmission [34]. As normal brain tissue is disrupted by invading cancer cells, decreases in NAA provide an excellent assessment of the associated neuronal damage. Additionally, intra-tumoral lipids (Lip)

have been shown to be a marker of necrosis present in high-grade lesions [35]. The oncometabolite 2HG, which was discussed extensively in **Section 2.5**, represents a specific marker for tumors that harbor gain-of-function mutations in the *IDH1/2* oncogenes. Taken together, these metabolites represent valuable biomarkers for magnetic resonance spectroscopic techniques and are able to probe specific biological aspects of a tumor lesion.

The integration of MR spectroscopic techniques into the clinical care of patients with LGG would have a profound impact on clinical management. Given that metabolic imaging can distinguish brain tumors at clinical presentation from various other pathologies of the brain, it can provide improved diagnosis. Detection of the presence of 2HG would allow for the further non-invasively genotyping tumors, monitoring novel therapies targeting the IDH-pathway, as well as distinguishing primary from secondary GBM. In the context of treatment planning, spectroscopic imaging sequence that elucidate the spatial distribution of physiological processes have several potential applications. They can help to define the spatial extent of an infiltrative lesion prior to neurosurgical resection or radiation therapy, much of which may not be possible through conventional MR imaging methods, and also identify areas of malignant transformation to ensure they are sampled for clinical histopathology [36, 37]. Furthermore, MR spectroscopy is a valuable tool for assessing therapeutic response, monitoring patients during routine follow-up, and evaluating tumor recurrence. The research presented in this dissertation highlights the clinical utility and novel applications of MR spectroscopy for patients with brain tumors. The ultimate goal of this work is to improve the clinical management of this disease.

## **2.10 References**

- [1] Q. T. Ostrom, H. Gittleman, P. Liao, C. Rouse, Y. Chen, J. Dowling, Y. Wolinsky, C. Kruchko, J. Barnholtz-Sloan, CBTRUS Statistical Report: Primary Brain and Central Nervous System Tumors Diagnoses in the United States in 2007-2011, *Neuro-Oncology* 16, iv1-iv63 (2014).
- [2] E. P. Widmaier, H. Raff, K. T. Strang. *Vander's human physiology : the mechanisms of body function.* -- 12th Ed, McGraw-Hill (2011).
- [3] J. T. Grier, T. Batchelor, Low-grade gliomas in adults, *Oncologist* 11, 681–693 (2006).
- [4] D. W. Parsons, S. Jones, X. Zhang, J. C. Lin, R. J. Leary, P. Angenendt, P. Mankoo, H. Carter, I. M. Siu, G. L. Gallia, A. Olivi, R. McLendon, B. A. Rasheed, S. Keir, T. Nikolskaya, Y. Nikolsky, D. A. Busam, H. Tekleab, L. A. Diaz Jr., J. Hartigan, D. R. Smith, R. L. Strausberg, S. K. Marie, S. M. Shinjo, H. Yan, G. J. Riggins, D. D. Bigner, R. Karchin, N. Papadopoulos, G. Parmigiani, B. Vogelstein, V. E. Velculescu, K. W. Kinzler, An integrated genomic analysis of human glioblastoma multiforme, *Science* 321, 1807–1812 (2008).
- [5] M. S. Ahluwalia, S. M. Chang. Medical therapy of gliomas, *J Neurooncol* 119, 503-512 (2014).
- [6] R. M. Young, A. Jamshidi, G. Davis, J. H. Sherman, Current trends in the surgical management and treatment of adult glioblastoma. *Ann Transl Med* 3, 121 (2015).
- [7] E. B. Claus, K. M. Walsh, J. K. Wiencke, A. M. Molinaro, J. L. Wiemels, J. M. Schildkraut, M. L. Bondy, M. Berger, R. Jenkins, M. Wrensch, Survival and low-grade glioma: the emergence of genetic information. *Neurosurg Focus* 38, E6 (2015).
- [8] Cancer Genome Atlas Network, et al., *N Engl. J Med* 372, 2481-98 (2015).
- [9] H. Yan, D. W. Parsons, G. Jin, R. McLendon, B. A. Rasheed, W. Yuan, I. Kos, I. Batinic-Haberle, S. Jones, G. J. Riggins, H. Friedman, A. Friedman, D. Reardon, J. Herndon, K. W. Kinzler, V. E. Velculescu, B. Vogelstein, D. D. Bigner, IDH1 and IDH2 mutations in gliomas. *N. Engl. J. Med.* 360, 765–773 (2009).
- [10] H.E. Leeper, A. A. Caron, P. A. Decker, R. B. Jenkins, D. H. Lachance, C. Giannini. IDH mutation, 1p19q codeletion and ATRX loss in WHO grade II gliomas. *Oncotarget*, (2015).
- [11] K. E. Yen, M. A. Bittinger, S. M. Su, V. R. Fantin, Cancer-associated IDH mutations: Biomarker and therapeutic opportunities. *Oncogene* 29, 6409–6417 (2010).
- [12] D. Rohle, J. Popovici-Muller, N. Palaskas, S. Turcan, C. Grommes, C. Campos, J. Tsoi, O. Clark, B. Oldrini, E. Komisopoulou, K. Kuni, A. Pedraza, S. Schalm, L.

Silverman, A. Miller, F. Wang, H. Yang, Y. Chen, A. Kernytsky, M. K. Rosenblum, W. Liu, S. A. Biller, S. M. Su, C. W. Brennan, T. A. Chan, T. G. Graeber, K. E. Yen, I. K. Mellinghoff, An inhibitor of mutant IDH1 delays growth and promotes differentiation of glioma cells. *Science*. 340, 626-30 (2013).

[13] T. Schumacher, L. Bunse, W. Wick, M. Platten, Mutant IDH1: An immunotherapeutic target in brain tumors. *Oncoimmunology* 3, e974392 (2015).

[14] L. Dang, D. W. White, S. Gross, B. D. Bennett, M. A. Bittinger, E. M. Driggers, V. R. Fantin, H. G. Jang, S. Jin, M. C. Keenen, K. M. Marks, R. M. Prins, P. S. Ward, K. E. Yen, L. M. Liau, J. D. Rabinowitz, L. C. Cantley, C. B. Thompson, M. G. Vander Heiden, S. M. Su, Cancer-associated IDH1 mutations produce 2-hydroxyglutarate. *Nature* 462, 739–744 (2009).

[15] C. Lu, P. S. Ward, G. S. Kapoor, D. Rohle, S. Turcane, O. Abdel-Wahab, C. R. Edwards, R. Khanin, M. E. Figueroa, A. Melnick, K. E. Wellen, D. M. O'Rourke, S. L. Berger, T. A. Chan, R. L. Levine, I. K. Mellinghoff, C. B. Thompson, IDH mutation impairs histone demethylation and results in a block to cell differentiation. *Nature*. 483, 474-8 (2012).

[16] L. S. Payne, P. H. Huang, The pathobiology of collagens in glioma. *Mol Cancer Res*. 12, 1129-40 (2013).

[17] S. Zhao, Y. Lin, W. Xu, W. Jiang, Z. Zha, P. Wang, W. Yu, Z. Li, L. Gong, Y. Peng, J. Ding, Q. Lei, K. L. Guan, Y. Xiong, Glioma-derived mutations in IDH1 dominantly inhibit IDH1 catalytic activity and induce HIF-1 $\alpha$ . *Science* 324, 261–265 (2009).

[18] C. L. Appin, D. J. Brat, Biomarker-driven diagnosis of diffuse gliomas. *Mol Aspects Med*, In press (2015).

[19] P. J. Killela, Z. J. Reitman, Y. Jiao, C. Bettegowda, N. Agrawal, L.A. Diaz, A. H. Friedman, H. Friedman, G. L. Gallia, B. C. Giovanella, A. P. Grollman, T. He, Y. He, R. H. Hruban, G. I. Jallo, N. Mandahl, A. K. Meeker, F. Mertens, G. J. Netto, B. A. Rasheed, G. J. Riggins, T. A. Rosenquist, M. Schiffman, L. Shih, D. Theodorescu, M. S. Torbenson, V. E. Velculescu, T. Wang, N. Wentzensen, L. D. Wood, M. Zhang, R. E. McLendon, D. D. Bigner, K. W. Kinzler, B. Vogelstein, N. Papadopoulos, H. Yan, TERT promoter mutations occur frequently in gliomas and a subset of tumors derived from cells with low rates of self-renewal. *PNAS* 110, 6021-26 (2013).

[20] K. M. Walsh, J. K. Wiencke, D. H. Lachance, J. L. Wiemels, A. M. Molinaro, J. E. Eckel-Passow, R. B. Jenkins, Telomere maintenance and the etiology of adult glioma. *Neuro Oncol*, In Press (2015).

[21] J. E. Eckel-Passow, D. H. Lachance, A. M. Molinaro, K. M. Walsh, P. A. Decker, H. Sciotte, M. Pekmezki, T. Rice, M. L. Kosel, I. V. Smirnov, G. Sarkar, A. A. Caron, T. M. Kollmeyer, C. E. Praska, A. R. Chada, C. Halder, H. M. Hansen, L. S. McCoy, P. M. Bracci, R. Marshall, S. Zheng, G. F. Reis, A. R. Pico, B. P. O'Neill, J. C. Buckner, C. Giannini, J. T. Huse, A. Perry, T. Tihan, M. S. Berger, S. M. Chang, M. D. Prados, J. Wiemels, J. K. Wiencke, M. R. Wrensch, R. B. Jenkins, Glioma Groups Based on

1p/19q, IDH, and TERT Promoter Mutations in Tumors. *N. Engl. J. Med.* 372, 2499-508 (2015).

[22] P. J. Basser, C. Pierpaoli, Microstructural and physiological features of tissues elucidated by quantitative-diffusion-tensor MRI. *J. Magn. Reson. B* 111, 209–219 (1996).

[23] J. M. Lupo, S. Cha, S. M. Chang, S. J. Nelson, Dynamic susceptibility weighted perfusion imaging of high-grade gliomas: characterization of spatial heterogeneity. *Am J Neuroradiol.* 26:1446-1454 (2005).

[24] T. R. McKnight, S. M. Noworolski, D. B. Vigneron, S. J. Nelson, An automated technique for the quantitative assessment of 3D-MRSI data from patients with glioma. *J. Magn. Reson. Imaging* 13, 167–177 (2001).

[25] Dwight G. Nishimura, *Principles of Magnetic Resonance Imaging*. Dwight G. Nishimura (2010).

[26] Malcolm H. Levitt, *Spin dynamics: basics of nuclear magnetic resonance*. John Wiley & Sons Ltd, (2001).

[27] O. A. Warburg, On the Origin of Cancer Cell. *Science* 3191, 309-14 (1956).

[28] M. Sharma, M. Astekar, S. Soi, B. S. Manjunatha, D. C. Shetty, pH Gradient reversal: An Emerging Hallmark of Cancers. *Recent Pat Anticancer Drug Discov* 10, 1-15 (2015).

[29] V. H. Villar, F. Merhi, M. Djavaheiri-Mergny, R. V. Durán, Glutaminolysis and autophagy in cancer. *Autophagy* 11, 1198-208

[30] C. Lobo, M. A. Ruiz-Bellido, J. C. Aledo, J. Marguez, I. Nunez De Castro, F. J. Alonso, Inhibition of glutaminase expression by antisense mRNA decreases growth and tumourigenicity of tumour cells. *Biochem J* 348, 257-261 (2000).

[31] I. Park, A. P. Chen, M. L. Zierhut, E. Ozturk-Isik, D. B. Vigneron, S. J. Nelson, Implementation of 3 T lactate-edited 3D <sup>1</sup>H MR spectroscopic imaging with flyback echo-planar readout for gliomas patients. *Ann. Biomed. Eng.* 39, 193–204 (2011).

[32] C. Yüksel, D. Öngür, Magnetic Resonance Spectroscopy Studies of Glutamate-related Abnormalities in Mood Disorders, *Biol Psychiatry* 68, 785-794 (2010).

[33] K. Glunde, Z. M. Bhujwala, S. M. Ronen, Choline metabolism in malignant transformation. *Nat Rev Cancer* 11, 835-848 (2011).

[34] H. D. Yan, K. Ishihara, T. Serikawa, M. Sasa, Activation of N-acetyl-L-aspartate of acutely dissociated hippocampal neurons in rats via metabotropic glutamate receptors. *Epilepsia* 44, 1153-9 (2003).

[35] E. J. Delikatny, S. Chawla, D. Leung, H. Poptani, MR-Visible Lipids and the Tumor Microenvironment. *NMR Biomed* 24, 592-611



[36] J. M. Lupo, S. J. Nelson, Advanced Magnetic Resonance Imaging Methods for Planning and Monitoring Radiation Therapy in Patients With High-Grade Glioma. *Semin Radiat Oncol* 24, 248-58 (2014).

[37] S. J. Nelson, Assessment of therapeutic response and treatment planning for brain tumors using metabolic and physiological MRI. *NMR Biomed* 24, 734-49 (2011).

## CHAPTER 3: Magnetic Resonance of 2-hydroxyglutarate in *IDH1*-mutated Low-grade Gliomas

---

In this project, we characterized the magnetic resonance features of 2HG in image-guided tissue samples from patients with recurrent low-grade glioma. We established high concordance between the presence of 2HG and histological confirmation of the mutation by immunohistochemistry and genetic sequencing. Additional analysis investigated correlations with 2HG and other *ex vivo* metabolites, *in vivo* imaging parameters, and histological measurements. This project demonstrated that 2HG is a reliable biomarker for *IDH*-mutation in gliomas and provided additional characterization of *IDH*-mutated lesions.

---

### Authors:

Adam Elkhaled, Llewellyn E. Jalbert, Joanna J. Phillips, Hikari A. I. Yoshihara, Rupa Parvataneni, Radhika Srinivasan, Gabriela Bourne, Mitchel S. Berger, Susan M. Chang, Soonmee Cha, Sarah J. Nelson

This work has previously been published in *Science Translational Medicine* and is reprinted with permission from AAAS: A. Elkhaled\*, L.E. Jalbert\*, J. Phillips, H. Yoshihara, R. Parvataneni, G. Bourne, M. Berger, S.M. Chang, S. Cha, and S.J. Nelson. "Magnetic Resonance of 2-Hydroxyglutarate in *IDH1*-mutated Low-grade Gliomas". *Science Translational Medicine*. 4, 116ra5 (2012). \*[equal contribution]

## **Abstract**

Recent studies have indicated that a significant survival advantage is conferred to patients with gliomas whose lesions harbor mutations in the genes isocitrate dehydrogenase 1 and 2 (*IDH1/2*). *IDH1/2* mutations result in aberrant enzymatic production of the potential oncometabolite D-2-hydroxyglutarate (2HG). Here, we report on the *ex vivo* detection of 2HG in *IDH1*-mutated tissue samples from patients with recurrent low-grade gliomas using the nuclear magnetic resonance technique of proton high-resolution magic angle spinning spectroscopy. Relative 2HG levels from pathologically confirmed mutant *IDH1* tissues correlated with levels of other *ex vivo* metabolites and histopathology parameters associated with increases in mitotic activity, relative tumor content, and cellularity. *Ex vivo* spectroscopic measurements of choline-containing species and *in vivo* magnetic resonance measurements of diffusion parameters were also correlated with 2HG levels. These data provide extensive characterization of mutant *IDH1* lesions while confirming the potential diagnostic value of 2HG as a surrogate marker of patient survival. Such information may augment the ability of clinicians to monitor therapeutic response and provide criteria for stratifying patients to specific treatment regimens.

## **Introduction**

Infiltrating gliomas are heterogeneous tumors of the central nervous system that include astrocytomas, oligodendrogliomas, and mixed oligoastrocytomas. Overall survival for these diseases can vary significantly depending on the grade of malignancy and histological characteristics, as defined by the World Health Organization (WHO) (1). Although patients diagnosed with infiltrating low-grade (grade II) gliomas generally live much longer than their high-grade counterparts (grades III and IV), there is substantial

heterogeneity in outcome, even for patients whose lesions share the same initial diagnosis. Because of the broad range of survival times and limited number of markers that can inform prognosis, there are several challenges for the clinical management of gliomas (1, 2). In 2009, there was a shift in the prognostic paradigm for these lesions, when more than 70% of all patients with low-grade gliomas were discovered to have mutations in the isocitrate dehydrogenase 1 and 2 (*IDH1/2*) genes, which have been associated with prolonged survival (3–6).

IDH1 and IDH2 are NADP<sup>+</sup> (oxidized form of nicotinamide adenine dinucleotide phosphate)–dependent oxidoreductases that catalyze the conversion of isocitrate to  $\alpha$ -ketoglutarate. IDH1 is found in the cytoplasm and in peroxisomes, where it plays a role in lipid metabolism. IDH2 is localized to the mitochondria and has been implicated in protecting the cell from oxidative damage (7–9). Missense mutations of *IDH1/2* genes were found to result in arginine being substituted by other amino acids at the substrate binding sites of IDH1/2 enzymes. Recent *in vitro* studies have revealed that mutation of arginine 132 (R132) in IDH1 and of arginine 172 (R172) in IDH2 prevents enzymatic oxidative decarboxylation of isocitrate and confers a new ability to convert  $\alpha$ -ketoglutarate to D-2-hydroxyglutarate (2HG) (10). The arginine mutations result in accumulation of 2HG and a vast reduction in normal IDH1/2 enzymatic activity. Although the function of both IDH-mutant enzymes and 2HG in gliomagenesis remains unclear, the improved prognosis associated with *IDH1/2* mutations suggests that the presence of 2HG may be of prognostic value as a surrogate for favorable genotypes. Given this potential, developing noninvasive *in vivo* methods for detecting 2HG in patients and evaluating other descriptive parameters of *IDH*-mutated lesions are of clinical interest.

The objective of this study was to characterize the metabolic profiles of recurrent, infiltrating low-grade gliomas using *ex vivo* proton high-resolution magic angle spinning ( $^1\text{H}$  HR-MAS) nuclear magnetic resonance (NMR) spectroscopy of tissue samples acquired by image-guided surgery. Crucial to this aim was determining whether levels of 2HG were sufficient for detection in *IDH*-mutated gliomas and, further, how the concentration of 2HG varied among gliomas that underwent a transition to a higher grade at the time of tumor recurrence. We hypothesized that if 2HG was detected from  $^1\text{H}$  HR-MAS spectra, levels of the suspected oncometabolite would be significantly higher in tissue samples that had manifest *IDH1* mutations. As an exploratory analysis, we also sought to evaluate whether histopathological or pre-operative *in vivo* MR imaging (MRI) parameters correlated with quantified levels of 2HG. Such information might be valuable for translational efforts geared toward noninvasively monitoring 2HG and predicting survival in patients with low-grade gliomas.

## **Results**

### ***Characterization of patient population***

Our institutionally approved study comprised 60 patients who had previously been diagnosed with WHO grade II glioma and were presenting for surgical resection owing to suspected disease recurrence. Presurgical *in vivo* MR examinations enabled the planning of targeted biopsies for sampling tissue from patient lesions. Imaging parameters derived from postprocessed diffusion-weighted imaging and spectroscopic data helped guide the designation of small, putatively defined tumor regions (5-mm-diameter spheres) on surgical navigation software. The criteria for planning image-guided biopsies were based on low apparent diffusion coefficients (ADCs) that represent

restricted diffusion associated with tumor cellularity and elevated choline-to-N-acetylaspartate (NAA) indices (CNIs) (Fig. 3.1, A and B), which provide measures of metabolic abnormality. *Ex vivo* HR-MAS spectra are presented to demonstrate the improved spectral resolution over conventional MR spectroscopy through the separation of individual choline-containing species that contribute to the *in vivo* total choline (tCHO) peak (Fig. 3.1C). Histological analysis of tissue samples collected from patients revealed that many had lesions that converted to a higher grade of malignancy at the time of recurrence: 25 patients had converted from WHO grade II to grade III and 6 patients converted to grade IV (Table 3.1). Eight patients (23 tissue samples) were excluded from the statistical analysis because their samples did not contain tumor, were too small for evaluation, or were contaminated by sterilizing agents used in the operating room. A total of 104 tissue samples from 52 patients remained for evaluation (Table 3.1). Complete patient data for all 60 subjects, including reasons for exclusion, are provided in table 3.S1.

	Grade	Total patients (tissue samples)	Astrocytoma patients (tissue samples)	Oligodendroglioma patients (tissue samples)	Oligoastrocytoma patients (tissue samples)
Collected	All	60 (127)	—	—	—
Excluded	All	8 (23)	—	—	—
Analyzed	All	52 (104)	21 (38)	22 (44)	9 (22)
	II→II	21 (37)	5 (8)	12 (22)	4 (7)
	II→III	25 (52)	12 (22)	9 (19)	4 (11)
	II→IV	6 (15)	4 (8)	1 (3)	1 (4)

**Table 3.1 Glioma patient population by tumor grade and histological subtype.**

Eight patients and 23 tissue samples were excluded owing to a lack of tumor cells observed by histological analysis, an insufficient amount of tissue in a sample for accurate HR-MAS analysis, or contamination of the sample with sterilizing agents. Individual patient information, including reasons for exclusion, is provided in table S1. The remaining tissue samples were classified by grade and histological subtype as astrocytoma, oligodendroglioma, or oligoastrocytoma, using criteria based on WHO II standards, as is the practice at our institution for clinical diagnosis. At the time of recurrence, most patient lesions were found to have converted to a higher grade of malignancy, whereas some remained grade II, as denoted by the arrows.

### ***IDH1 immunohistochemistry***

The IDH1 status of paired tissue samples from each patient (n = 52) was assessed to compare wild-type against mutant IDH1 spectral profiles (11). Antibody staining indicated that 38 patients had gliomas with histidine-mutated (R132H) IDH1 enzymes. Tissue samples that stained positive for the *IDH1*<sub>R132H</sub> mutation, as seen colored in brown (Fig. 3.2A), were shown to visually contrast with those that tested negative for the modified enzymes (Fig. 3.2B). An electropherogram of sequenced genomic DNA (gDNA) from an *IDH1*<sub>R132H</sub>-mutant tissue sample illustrates the most common heterozygous mutation of residue R132 (Fig. 3.2C). Immunohistochemistry results were consistent across all tissue samples from a particular patient in 94.4% of cases (table 3.S1A). Because the *IDH1*<sub>R132H</sub> antibody is only selective for histidine mutations at residue R132 of *IDH1*, it was expected that samples with other *IDH1* and *IDH2* mutations would not be detected. Genetic sequencing of a grade II sample subset (n = 21) revealed that two of the patients testing negative for IDH1-mutant enzymes by antibody staining were, in fact,

carrying the serine mutation (*IDH1*<sub>R132S</sub>) and nine carried the histidine mutation (Table 3.1B), which corroborated the antibody staining (Fig. 2). Overall, 40 patients were classified as being positive for *IDH1* mutations (*IDH1*+) and 12 as *IDH1*-negative (*IDH1*-) (Table 2B). Furthermore, 26 of the 31 (83.9%) patients whose lesions had converted to a higher grade at the time of recurrence were classified as *IDH1*+ compared to 14 of the 21 (66.7%) whose lesions had remained grade II.



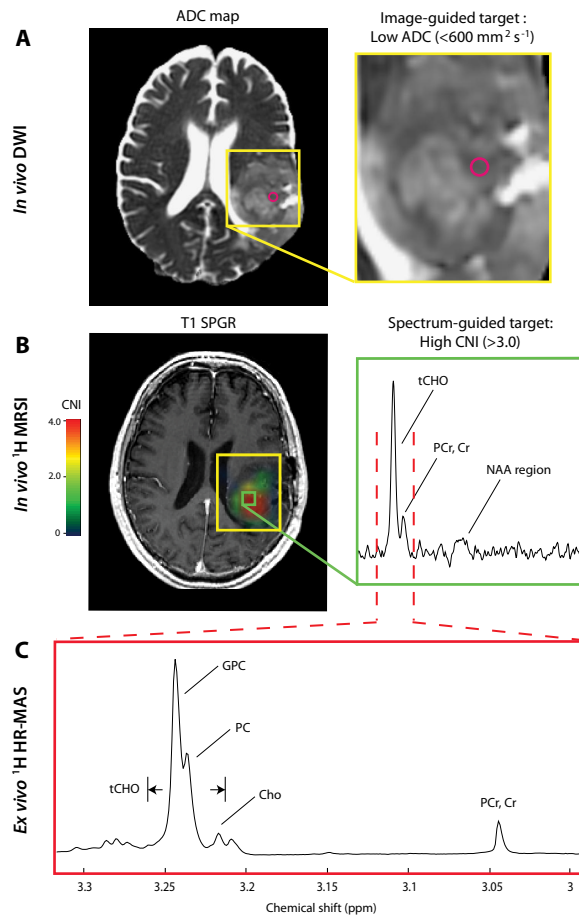


**Fig. 3.1 Designating tissue targets from presurgical *in vivo* imaging.** (A) ADC map derived from diffusion-weighted imaging (DWI) shows a hypo-intense region of low diffusion relative to normal-appearing white matter that was designated as a target for tissue sampling in a WHO grade III astrocytoma. Tissue targets were defined as 5-mm-diameter spheres on surgical navigation software. (B) *In vivo* MRSI (extent of coverage defined by yellow box) overlaid on T1-weighted spoiled gradient echo (SPGR) image along with a choline-to-NAA index (CNI) color map. A spectrum from a region of elevated CNI targeted for tissue sampling is displayed in the green box. Cr, creatine; NAA, N-acetylaspartate; PCr, phosphocreatine; tCHO, total choline. (C) Sample *ex vivo*  $^1\text{H}$  HR-MAS spectrum from tissue acquired at the site of elevated CNI for comparison *with in vivo* spectroscopy data in (B). Cho, free choline; GPC, glycerophosphocholine; PC, phosphocholine.

### ***Magnetic resonance spectroscopy of a 2HG phantom***

The one-dimensional (1D) NMR spectrum of a buffered stock solution of 2HG features four signature multiplets arising from five alkyl hydrogens: one  $\alpha$ , two  $\beta$ , and two  $\gamma$  (fig. 3.S1). Although 2HG shares the same AMNPQ spin system as glutamate (Glu), its 2-hydroxyl (2-OH) is more electron-withdrawing than Glu's 2-amino (2-NH<sub>2</sub>) substituent,

causing the  $\alpha$ -proton to resonate further downfield at 4.05 ppm (parts per million) as a doublet of doublets. The chirality of 2HG combined with the distinct chemical environment experienced by each of the resonating protons gives rise to complex vicinal and geminal coupling, which is reflected in the elaborate splitting patterns of the spectra. The  $\beta$ -protons, for example, display highly coupled resonances that are seen to have chemical shifts of 2.01 and 1.85 ppm, respectively. Situated furthest from the chiral center of the second carbon,  $\gamma$ -protons produce overlapping resonances that appear as a single 13-peak multiplet centered at 2.28 ppm. J-resolved spectroscopy experiments (Supplementary Methods) allowed for an approximation of the interproton spin-spin coupling constants ( $^2,^3J$ ), which was optimized using spectral simulation software (fig. 3.S1). Separation of the  $\gamma$  resonances (Supplementary Methods) was performed at ultrahigh magnetic field strength to demonstrate the  $\gamma$ -proton's mutual coupling with each other and  $\beta$ -protons in greater detail (fig. 3.S2).

### ***Identification of 2HG ex vivo in tissue samples***

$^1\text{H}$  HR-MAS spectra showed that most of the evaluable tissue samples contained detectable levels of 2HG (Table 3.2A). Of the 52 patients, 14 had spectra with inadequate resolution and signal-to-noise ratio (SNR) for identifying the signature peaks of 2HG, by either visual inspection or curve-fitting algorithms. This left tissue samples from 38 patients with spectra that could be analyzed. Of these patients, 33 (86.8%) were visually classified as 2HG+ and 5 as 2HG- by referencing discriminating resonances of 2HG from 1D and 2D spectra; additionally, 29 2HG+ patients had levels of 2HG that were quantified using curve-fitting algorithms. At a sample level, this translated to 58 2HG+ and 8 2HG- tissue samples (Table 3.2A). The fact that there were so few 2HG- samples precluded a statistical analysis between 2HG+ and 2HG- cohorts.

The  $T_2$ -weighted Carr-Purcell-Meiboom-Gill (CPMG) (12) sequence was chosen for its ability to eliminate broad macromolecular signals, effectively creating a smooth spectral baseline that could resolve subtle metabolite features. CPMG acquisitions provided clear delineation of 2HG from neighboring metabolites  $\gamma$ -aminobutyric acid (GABA), glutamine (Gln), and Glu and were therefore used for all further analyses in this study. CPMG spectra from patients with contrasting mutant and wild-type *IDH1* genotypes show the characteristic presence and absence of 2HG, respectively (Fig. 3.3, A and B). The blue traces represent the acquired data; red traces represent the spectral curve-fitting performed with the semiparametric high-resolution quantum estimation (HR-QUEST) algorithm. HR-QUEST used an iterative process of approximation to independently fit each of the chemical shifts of 2HG for quantification in the time domain. As shown in Fig. 3A, the 2HG  $\gamma$ -protons multiplet centered at 2.28 ppm offered the best means of visual 2HG recognition on account of its distinct splitting pattern and relative signal intensity, which was comparable to that of neighboring metabolites. Although the  $\alpha$ - and  $\beta$ -proton multiplets are seen as relatively distinct in this particular example (Fig. 3.3A), they are more likely to be obscured by overlapping resonances in 1D spectra.

The 2D total correlation spectroscopy (TOCSY) (13) spectrum provided further confirmation of the presence of 2HG on the basis of three well-defined cross peaks located along a vertical column at F2/F1, [4.05/1.85 ppm], [4.05/2.01 ppm], and [4.05/2.28 ppm] (Fig. 3.3C). Each of these resonances corresponds to either the  $\gamma$ - or  $\beta$ -proton's shared magnetization with the  $\alpha$ -proton and together constitute a spectral feature that is separable from the resonance of myo-inositol (myo-I) on account of relative chemical shifts. Although the other expected cross peaks of 2HG were detectable between 1.85 and 2.28 ppm, potential interference from the resonances of

GABA, Gln, and Glu in this region made the  $\alpha$ -proton cross peaks at 4.05 ppm a more suitable form of identification for 2HG with the TOCSY experiment (Fig. 3.3C).

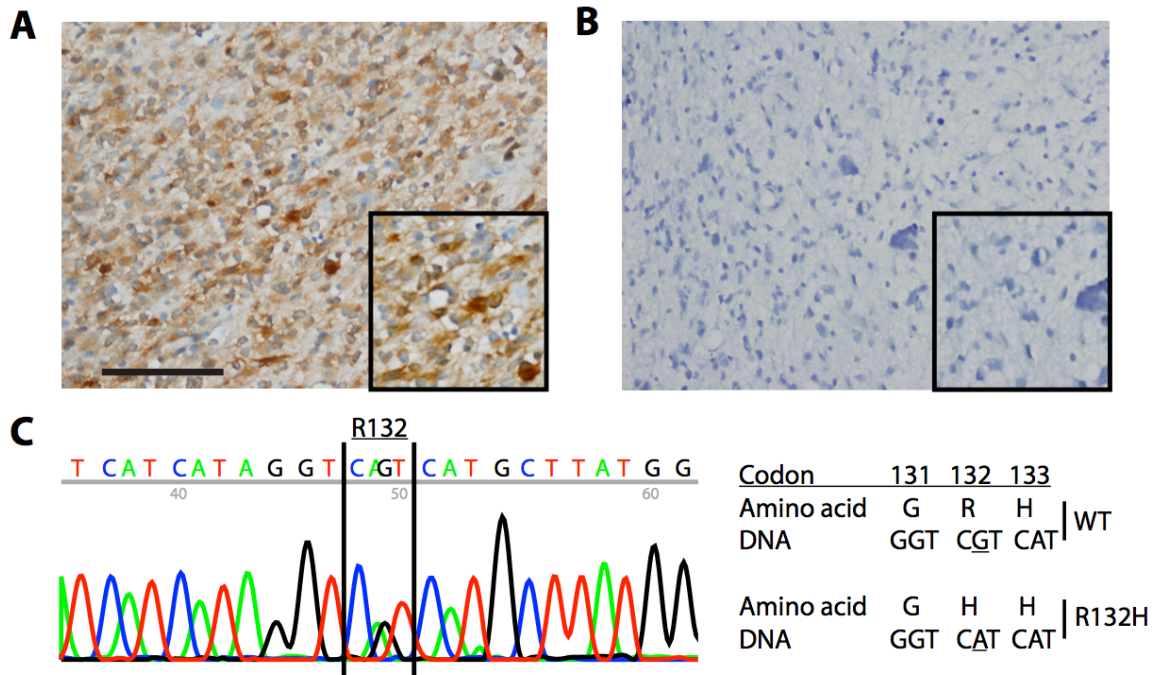


**Fig. 3.2  $IDH1_{R132H}$  immunostaining and direct sequencing of  $IDH1$  gDNA.** (A)  $IDH1_{R132H}$  antibody staining (brown) on a 2HG+ WHO grade III astrocytoma tissue sample, which was representative of 44 tissue samples. The corresponding 1D and 2D spectra for this sample are shown in Fig. 3, A and C, respectively. Scale bar, 100  $\mu$ m. (B) Complementary image of a 2HG- sample on which immunostaining for  $IDH1_{R132H}$  was also performed and no mutant enzymes were found (representative of seven samples). (C) Electropherogram of polymerase chain reaction (PCR)-amplified gDNA performed on an  $IDH1_{R132H}$ -mutant tissue sample. Codon 132 displays signal from the mutant base pair composed of an adenine (mutant) and guanine [wild-type (WT)] nucleobase, each present on complimentary strands of DNA. The heterozygous substitution of adenine at R132 results in the production of histidine at the substrate binding site of IDH1 and neomorphic enzymatic activity.

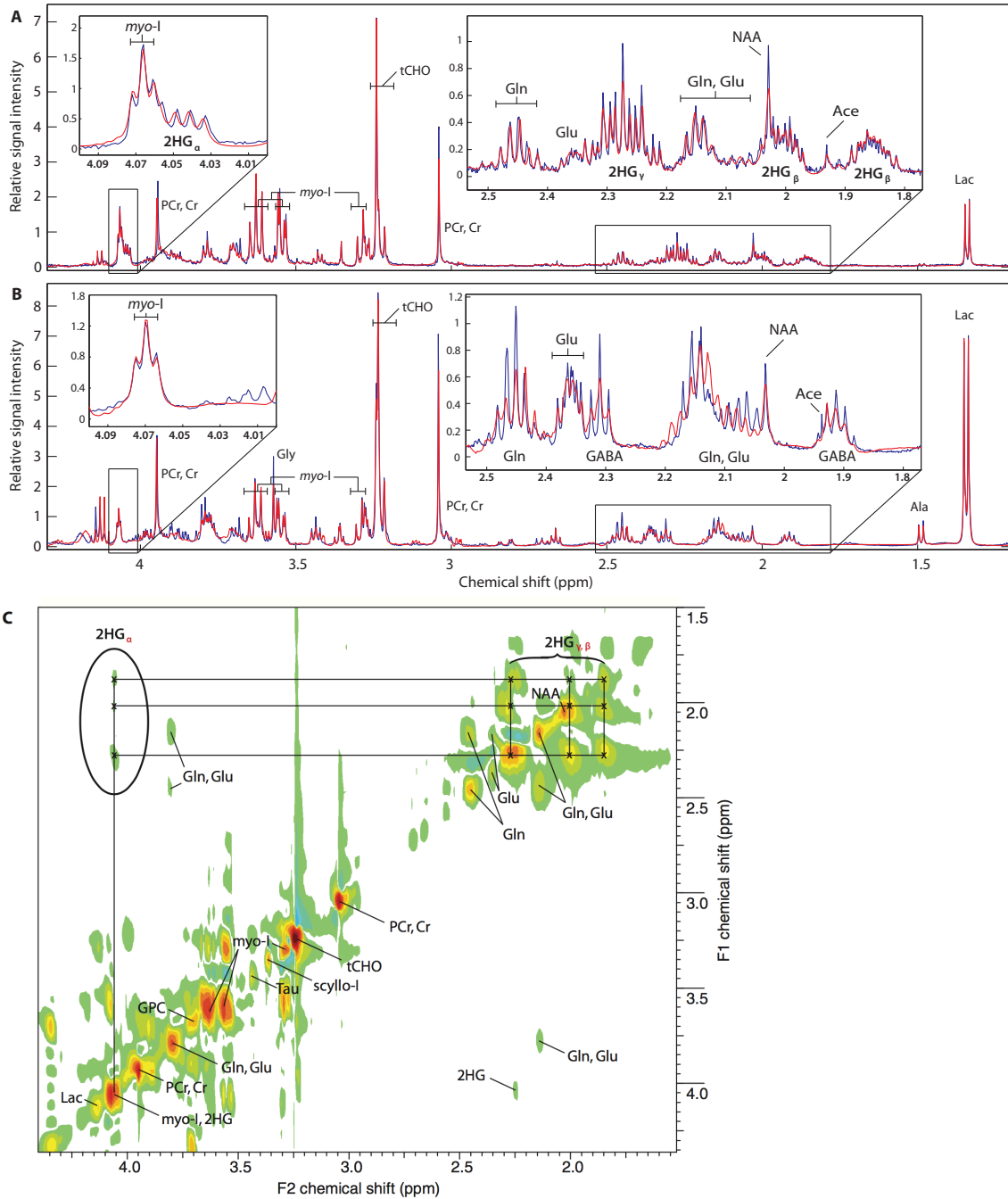


**Fig. 3.3 Ex vivo spectra from mutant 1.5 and WT *IDH1* tissue samples.** (A and B) 1D CPMG spectrum from an *IDH1*-mutant WHO grade III astrocytoma (A) and WT *IDH1* grade IV astrocytoma (B). For both (A) and (B), the blue trace represents acquired data and the red trace represents the spectral fit used for relative quantification of 2HG levels by HR-QUEST. These spectra are not normalized with respect to each other. (C) 2D TOCSY spectrum of *IDH1*-mutant tissue depicted in (A). Shared magnetization between nuclei of discrete molecular spin systems is rendered through resonant cross peaks about the F2/F1 diagonal. The correspondence among individual cross peaks of 2HG is highlighted along with the uniquely identifying spectral feature created with respect to the  $\alpha$ -proton, labeled as  $2HG_{\alpha}$ . Ace, acetate; Ala, alanine; Gln, glutamine; Glu, glutamate; Gly, glycine; Lac, lactate; myo-I, myo-inositol; scyllo-I, scyllo-inositol; Tau, taurine.

A. Tissue sample and patient-level concordance between <i>IDH</i> and 2HG							
Tissue-level (n = 104)				Patient-level (n = 52)			
<b>2HG+</b>	<b>2HG-</b>	<b>Indeterminate</b>	<b>Total</b>	<b>2HG+</b>	<b>2HG-</b>	<b>Indeterminate</b>	<b>Total</b>
58	8	38	104	33	5	14	52
<b>IDH+</b>	<b>IDH-</b>	<b>Indeterminate</b>	<b>Total</b>	<b>IDH+</b>	<b>IDH-</b>	<b>Indeterminate</b>	<b>Total</b>
73	24	7	104	40	12	0	52
<b>IDH</b>	<b>2HG-</b>	<b>2HG+</b>	<b>Agree</b>	<b>IDH</b>	<b>2HG-</b>	<b>2HG+</b>	<b>Agree</b>
R132H-	7	7	7/14	R132H-	4	5	4/9
R132H+*	1	44	44/45	R132H+*	1	28	28/29
Overall concordance	51/59 (86.4%)			Overall concordance	32/38 (84.2%)		

B. Concordance between <i>IDH</i> and 2HG according to WHO grade						
	Grade II (n = 21 patients)		Grade III (n = 25 patients)		Grade IV (n = 6 patients)	
	<i>IDH+</i> (n = 14)	<i>IDH-</i> (n = 7)	<i>IDH+</i> (n = 22)	<i>IDH-</i> (n = 3)	<i>IDH+</i> (n = 4)	<i>IDH-</i> (n = 2)
2HG+	9	2	15	3	4	0
2HG-	0	2	1	0	0	2
2HG indeterminate	5	3	6	0	0	0
<b>Agreement</b>	11/13		15/19		6/6	
2HG+/ <i>IDH-</i>	2		3		0	
2HG-/ <i>IDH+</i>	0		1		0	

\*The *IDH+* category includes two R132S mutations found from sequencing.

**Table 3.2 Classification of 2HG presence and *IDH1* mutation status.** (A) The presence of 2HG in HR-MAS spectra was assessed visually from the 1D spectrum and confirmed by the presence of signature cross peaks in the 2D TOCSY spectrum. *IDH1* mutation analysis was performed with the R132H antibody and further sequencing of gDNA from a subset of patients who had been randomly selected. The concordance between *IDH* mutations and the presence of 2HG was assessed for both tissue samples and patients. This table assumes 2HG presence as positive if at least one tissue sample from a particular patient had detectable 2HG; *IDH* status was assumed positive if at least one tissue sample was confirmed positive by sequencing or antibody staining. Samples that were designated as indeterminate for 2HG presence were excluded from analysis on the basis of insufficient tissue for analysis or inadequate resolution from acquired spectra. Samples were classified as “indeterminate” for *IDH* mutation if there was insufficient tissue for immunohistochemical analysis. (B) Comparison between the assessments of *IDH* mutation and 2HG presence in 52 patients stratified by glioma grade, as determined by clinical pathology.

#### **Concordance of *IDH1* mutation status and presence of 2HG**

There was an 86.4% concordance (51 of 59 tissue samples; 32 of 38 patients) between the presence of 2HG, as detected by <sup>1</sup>H HR-MAS spectroscopy, and *IDH1* mutation status, as determined by antibody staining and genetic sequencing (Fig. 3.2 and Table 3.2A). A breakdown of this concordance according to glioma grade is presented in Table 3.2B. Of the eight discordant tissue samples, one had a level of 2HG that fell below the threshold for visual spectroscopic detection, perhaps as a result of sectioning the tissue

sample such that most of the tumor was contained in the portion analyzed for pathology. The remainder of discordant samples came from biopsies with insufficient tissue (<0.5 mg) for validation by genetic sequencing but may have harbored alternative *IDH1* or *IDH2* mutations (table 3.S1). Two of the samples classified by sequencing as *IDH1*<sub>R132S</sub> that had not been identified by the *IDH1*<sub>R132H</sub> antibody staining were also found to contain detectable levels of 2HG. Although this was an expected outcome, because the *IDH1*<sub>R132H</sub> antibody is only specific for histidine mutations, it proves that MR methodologies are capable of identifying multiple mutations of the *IDH1* gene.

### ***Levels of 2HG among tumor grades***

Relative abundance of 2HG in tissue samples suggests varied accumulation in gliomas of different grades. 2HG abundance was reported in relative levels (unitless) because of the  $T_2$  relaxation time dependence of the CPMG acquisition and metabolite-tissue interactions, which precluded absolute quantification. Mean 2HG levels were shown to increase across the 29 patients with spectra quantified for 2HG from grade I ( $0.36 \pm 0.22, n=8$ ) to grade III ( $0.56 \pm 0.38, n=17$ ) to grade IV ( $0.77 \pm 0.20, n = 4$ ) (Fig. 4A). When analyzed with an exact Wilcoxon rank-sum test, there was a statistically significant difference found between 2HG abundance in grade II and IV samples ( $P = 0.016$ ) (Fig. 3.4A), whereas the broad range of values shown by tissue from grade III lesions prevented distinction from the other grades. After these levels were normalized by average cellularity (calculated as the number of cells per 200 $\times$  field), the statistical relationship between grades II and IV no longer existed ( $P = 0.38$ ) (Fig. 3.4B).

### ***Ex vivo correlations of 2HG***

The levels of several metabolites that were quantified from <sup>1</sup>H HR-MAS spectra of biopsy

samples were found to correlate with 2HG abundance (table 3.S2 and fig. 3.S3). These were *ex vivo* metabolites commonly associated with tumor, including all of the choline-containing species: free choline (Cho), phosphocholine (PC), and glycerophosphocholine (GPC), as well as the combined measure of tCHO. As an *in vivo* marker of cell membrane turnover, tCHO has been used extensively to discern tumor regions with increased cellularity. Its elevation is currently one of the best spectroscopic markers of tumor presence, especially when evaluated alongside attenuated levels of NAA, which indicate diminished neuronal functioning due to neoplastic infiltration. Other brain metabolites related to malignancy, such as aspartate (Asp), GABA, threonine (Thr), hypotaurine (hypo-Tau), creatine and phosphocreatine (Cr, PCr), betaine (Bet), glycine (Gly), lactate (Lac), glutathione (GSH), phosphoethanolamine (PE), Glu, and Gln, were also seen to increase with 2HG levels.



These relationships reflect 2HG's association with several aspects of tumor metabolism: Cr and PCr are commonly used as measures of bioenergetics, Lac is typically a product of anaerobic respiration under hypoxic conditions, GSH is an antioxidant that is thought to combat the extreme oxidative stress caused by reactive oxygen species, and Glu and Gln often signal changes in mitochondrial activity (14). Furthermore, the myo-I-to-tCHO index (MCI) was negatively correlated with levels of 2HG (fig. 3.S3 and table 3.S2). MCI serves as a novel *in vivo* parameter for evaluating the relative contributions of tumor and treatment-affected tissue, pathologically defined as gliosis (15). Therapeutically treated tissues, although often mimicking tumor on radiographic imaging, express higher levels

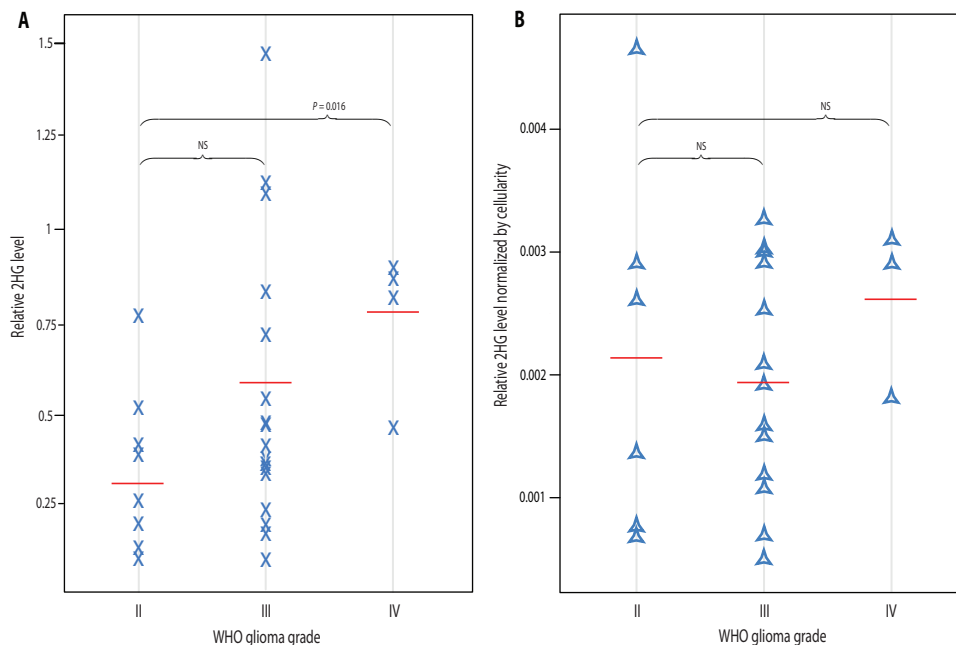


**Fig. 3.4 2HG levels according to WHO glioma grade.** (A) Plot of relative 2HG levels quantified by HR-QUEST in relation to malignancy grades. Mean relative levels per patient (n = 29 total: 7, grade II; 18, grade III; 4, grade IV) were evaluated by an exact Wilcoxon rank-sum test. Brackets indicate the statistical comparison of grade II 2HG levels with those of gliomas that had transformed to a higher grade; significance was defined as  $P < 0.05$ . (B) These levels are also shown normalized with respect to cellularity (number of cells per 200 $\times$  field) for those patients whose tissue samples could be evaluated for this parameter (n = 22 total: 6, grade II; 13, grade III; 3, grade IV). NS, not significant.

of myo-I compared to tCHO and thus show a characteristic elevation in this index. The fact that 2HG levels correlate with MCI and the list of tumor-related metabolites helps confirm the association of 2HG with malignant tissue.

### ***Tumor tissue histopathology and 2HG***

There was a positive correlation observed between levels of 2HG and mitotic activity, as measured by the MIB-1 index (for evaluating the proportion of cells undergoing mitoses via immunostaining), relative tumor content [scored by the contribution of tumor to overall cellularity (“tumor score”)], and cellular density (Table 3, fig. 3.S3, and table 3.S2). 2HG levels were negatively correlated with the presence of delicate vasculature found in normal brain tissues using factor VIII staining of vessel lumen. Axonal disruption, as measured by neurofilament antibody staining, was not found to be linked to changes in 2HG concentration in tumor tissue.

### ***In vivo correlations of ADC with 2HG***

To test whether MRI parameters were able to provide additional information regarding *IDH*-mutant lesions, we assessed their correlations with levels of 2HG quantified from HR-MAS spectra. By using the coordinates of each targeted biopsy acquired during surgery, it was possible to relate presurgical *in vivo* patient imaging to sampled tissue. ADCs derived from *in vivo* diffusion-weighted imaging represent the relative diffusivity of water through tissue. Restricted diffusion in the brain, corresponding to low intensities on ADC maps, is often associated with highly cellular regions of tumor (16). 2HG levels showed a negative correlation with ADC, as well as ADC normalized by normal-appearing white matter in the brain (Table 3.3 and fig. 3.S3), indicating a regional association with tumor.

Also correlated with 2HG were the eigenvalues describing the magnitude of water diffusion along orthogonally related principal and secondary directions, denoted as  $\lambda_1$  and  $\lambda_2$ , respectively (Table 3.3 and fig. 3.S3). Because ADC is mathematically derived from constituent eigenvalues, this information provides further detail for characterizing how diffusion phenomena in tumor relate to 2HG. These were important parameters to evaluate, because diffusion imaging is routinely used by clinicians to assess treatment response and tumor progression.

A similar analysis was performed on metabolite levels acquired from *in vivo* spectroscopic measures of Cr, tCHO, NAA, and Lac + lipid; however, owing to the limited coverage volume of our spectroscopy, many of the tissue samples did not have associated metabolite data. Partial voluming with tissue surrounding the primary lesion further limited spectroscopic correlations on the basis of lower *in vivo* resolution. Despite these limitations, the higher-resolution *ex vivo* spectroscopy suggests that *in vivo* tCHO, Cr, and Lac are likely to be elevated in *IDH*-mutant lesions and to correlate with levels of 2HG, along with other metabolites found significant from *ex vivo* analyses (Table 3.3).

<b>Variables correlated with 2HG</b>	<b>Number of patients</b>	<b>Number of tissue samples</b>	<b>Regression coefficient</b>	<b><i>P</i></b>
<b>Ex vivo metabolites</b>				
PC	23	40	0.27	0.003
GPC	25	43	0.15	0.003
tCHO	25	45	0.12	<0.001
Cr, PCr	25	44	0.16	0.03
PE	25	43	0.18	<0.001
GSH	18	28	0.45	0.001
Glu	25	45	0.19	<0.001
Gln	25	43	0.16	0.001
GABA	11	11	6.49	0.02
Ala	12	15	0.92	0.02
Gly	24	39	0.14	0.01
Bet	19	27	12.76	<0.001
Hypo-Tau	10	16	2.68	0.009
Lac	25	45	0.11	<0.001
MCI	25	45	-0.09	0.024
<b>Histopathology parameters</b>				
Average cell density	18	33	<0.001	0.002
Tumor score	22	39	0.25	0.004
MIB-1 index	21	38	0.11	0.006
Delicate vascularity	21	38	-0.21	0.004
<b>In vivo diffusion parameters</b>				
ADC	21	40	<0.001	<0.001
<i>n</i> ADC	21	40	-0.36	<0.001
$\lambda_1$	18	31	<0.001	0.007
<i>n</i> $\lambda_1$	18	31	-0.47	0.009
<i>n</i> $\lambda_2$	18	31	-0.32	0.024

**Table 3.3 2HG correlations with *ex vivo* metabolites, histopathology parameters, and *in vivo* diffusion parameters.** Each of the study parameters correlated with 2HG is presented. This statistical method used a simple regression model and evaluated all of the tissue samples collectively while correcting for correlated responses via bootstrap estimation. *P* values were obtained by testing the probability of correlation slopes deviating a given value from zero. *n* $\lambda_1$  and *n* $\lambda_2$  represent the normalized eigenvalues of the principal and secondary components of diffusion, respectively. Bet, betaine; GSH, glutathione; Hypo-Tau, hypotaurine; MCI, myo-I-to-tCHO index; PE, phosphoethanolamine.

## **Discussion**

This study has demonstrated the feasibility of detecting 2HG and quantifying its relative abundance in *IDH1*-mutated gliomas using  $^1\text{H}$  HR-MAS spectroscopy. There was a strong concordance established between *IDH1*-mutant tissue samples acquired from patients and the presence of 2HG. These data corroborate the previously identified relationship between *IDH1* mutation and the aberrant production of this metabolite that was validated using liquid chromatography–mass spectrometry analysis (10). Because our study design constrained the acquisition of targeted biopsies to relatively small regions with homogeneous *in vivo* imaging characteristics, the sampled tissue was in some cases not ideal for spectroscopic analysis. Despite this limitation, it was possible to obtain an accurate assessment of the presence and absence of 2HG for most of the patients evaluated. When present, the levels of 2HG were on par with those of the chemically related metabolites Glu and Gln, which are readily detected using  $^1\text{H}$  HR-MAS spectroscopy.

We noted several important correlations between 2HG levels in human tissue and parameters that are associated with gliomas. Relationships between levels of 2HG and other *ex vivo* metabolites may aid in our understanding of the altered metabolic state of *IDH*-mutated glioma and in determining whether 2HG is a contributing factor. The standing hypothesis that 2HG is a tumor-promoting oncometabolite (3) currently lacks full mechanistic support; however, there are advantages to elucidating the biochemical pathways that are influenced by 2HG and may lead to improved survival for patients with *IDH* mutations. The correlations between histopathology parameters and levels of 2HG that were observed in our study indicated that lesions with *IDH1*-mutant enzymes have increased mitotic activity, with elevated tumor scores and cell density. The strong

correlation between these parameters is consistent with there being higher cellularity in *IDH*-mutant gliomas where 2HG is present. This implies that *in vivo* levels of 2HG may be able to contribute not only to the classification of glioma but also to characterizing the spatial extent of infiltrative lesions.

The negative correlation between 2HG and normal delicate vascularity may assist in designing strategies for treating lesions with mutant IDH1 enzymes. 2HG has been associated in the literature with the competitive inhibition of oxygen-sensing prolyl hydroxylases (PHDs) and histone demethylases (17, 18). Restraining PHD activity is hypothesized to result in an up-regulation of proangiogenic growth factors, including a common chemotherapy target, vascular endothelial growth factor (VEGF). It is therefore of clinical interest whether patients harboring IDH mutations may be ideal candidates for therapies that target 2HG production as well as antiangiogenic agents that promote vascular normalization. With regard to histone demethylases as chromatin-modifying enzymes, their inhibition could alter the regulation of gene expression such that oncogenesis is provoked (18), another potential reason to therapeutically reduce levels of 2HG.

We also found a significant relationship between IDH1 mutants— as identified via 2HG levels in tissue—and *in vivo* MR diffusion parameters, which supports the potential role of diffusion imaging in evaluating whether the tissue architecture of mutant gliomas is distinct from that of other neoplasms. The elevation of tCHO that we observed from the *ex vivo* spectra of *IDH1*-mutant gliomas suggests that *in vivo* levels of tCHO may also be important for evaluating these lesions. Because MR diffusion and spectroscopy measures are readily obtained on most clinical MR scanners, they may be useful in defining regions of interest for studying variations in levels of 2HG.

The fact that the observed levels of 2HG from tissue samples expressing *IDH1* mutations were similar to those of other routinely detected metabolites, such as Gln and Glu, supports the potential clinical use of 2HG as a noninvasive biomarker for *IDH1*. Given that tissue samples taken from disparate regions of tumor were homogeneous in their mutation status, it is reasonable to assume that 2HG will be present throughout lesions expressing aberrant enzymes. The elevated levels of 2HG in gliomas that had converted to a higher grade at the time of recurrence were attributable to differences in cellularity. This is an important finding because it suggests that the amount of 2HG produced per tumor cell remains unchanged during malignant transformation. From the correlation between levels of 2HG, tumor score, and tissue cellularity, it seems likely that 2HG will contribute to determining the extent of recurrent tumor in an *in vivo* setting. This will be valuable in differentiating tumor from treatment effects, especially in difficult cases where ambiguous anatomic imaging complicates interpretation by a neuroradiologist.

This study has provided important information that should be considered carefully in the development of technology for translating 2HG detection into an *in vivo* setting. One of the main challenges is providing a robust *in vivo* method for resolving 2HG from neighboring metabolites that are of a similar concentration and will have overlapping resonances at clinical field strengths. There have been three preliminary studies that have reported on the detection of *in vivo* 2HG peaks in patients with *IDH1*-mutated gliomas (19, 20, 21). These used different acquisition parameters and reported varying accuracies for estimated metabolite levels based on the Cramar-Rao bounds derived using the LCModel algorithm for spectral quantification. Spectral editing and more sophisticated data acquisition methods, including variants of the 2D experiment used in our study, may be useful in separating these components and verifying individual

resonances (21). From our data, it appears that focusing on the unobstructed spectral feature created by the  $\alpha$ -proton may be of interest for improving the specificity and accuracy of detecting 2HG *in vivo*.

Considering the survival benefits associated with *IDH1/2* mutations, the presence of 2HG may have significant prognostic value for patients with low-grade gliomas. The characterization of IDH-mutated lesions using MR methods could also hold implications for the study of other human cancers that share these genetic abnormalities, including colorectal cancer, prostate cancer, and acute myeloid leukemia, which shows an adverse prognosis for *IDH1/2* mutations, in contradistinction with gliomas (22, 23). Recent evidence suggests that many of these cancers carry chemosensitive properties that could enhance treatment efficacy and inform clinicians on how to stratify patients for different therapies (5). If D-2HG truly bears oncogenic properties (3), then testing for mutations in the *IDH* gene will probably not be sufficient for the clinical management of glioma patients; additional monitoring of 2HG levels would become important, especially for therapies targeting the IDH1 pathway (24, 25). Finally, as a potential marker for tumor *in vivo*, 2HG may prove especially helpful to clinicians attempting to discern disease recurrence from treatment effects in patients whose radiographic imaging is considered suspect. This information may help clinicians identify candidates for the most appropriate therapies or clinical trials and assist in the monitoring of treatment.

## **Materials and Methods**

### ***Patient population***

This study was approved by our Institutional Review Board before patient recruitment. Informed consent was obtained from each participating subject. A total of 60 patients



whose initial diagnosis was WHO grade II glioma and who were presenting for surgical resection owing to suspected recurrence were enrolled. All participants had previously received standard-of-care treatments that included surgical resection, radiation therapy, and/or chemotherapy. Six patients were excluded because of methanol contamination from the operating room, one patient was excluded because of a lack of tumor cells present in their tissue samples, and one patient was excluded because of insufficient tissue size (<0.5 mg) and degraded cellular integrity. This left 52 patients to be analyzed by this study. A complete list of patients and tissue samples is provided in table S1 along with exclusion criteria.

### ***Preoperative MRI and spectroscopy***

Preoperative MR examinations were conducted on a 1.5 T or 3 T EXCITE GE Signa Echospeed scanner (GE Healthcare Technologies) using an eight-channel phased-array headcoil (MRI Devices). Functional imaging included six-directional diffusion-weighted imaging acquired in the axial plane [repetition time (TR)/echo time (TE) = 1000/108 ms, voxel size =  $1.7 \times 1.7 \times 3 \text{ mm}^3$ ,  $b = 1000 \text{ s/mm}^2$ ] and Lac-edited 3D MR spectroscopic imaging ( $^1\text{H}$  MRSI) using point-resolved spectroscopic selection (PRESS) for volume localization and very selective saturation (VSS) pulses for lipid signal suppression (excited volume =  $80 \times 80 \times 40 \text{ mm}^3$ , overpress factor = 1.5, TR/TE = 1104/144 ms, field of view =  $16 \times 16 \times 16 \text{ cm}^3$ , nominal voxel size =  $1 \times 1 \times 1 \text{ cm}^3$ , flyback echo-planar readout gradient in the SI direction, 712 dwell points and 988 Hz sweep width) (26).

### ***Postprocessing of preoperative MR exam***

The *in vivo* data from the preoperative examination were transferred to a Sun Ultra 10 workstation (Sun Microsystems), and in-house software was applied to derive estimates

of *in vivo* diffusion and spectroscopic parameters. Maps of the ADC were generated on a pixel-by-pixel basis according to a published algorithm (27). MRSI data were processed to quantify tCHO and NAA levels, from which maps of the CNI could be derived. CNI values were generated from a linear regression-based algorithm (28) and represent the changes in choline and NAA levels relative to normal voxels.

### ***Image-guided brain tumor tissue sampling***

Regions demonstrating either abnormally decreased ADC and/or elevated CNI values, consistent with viable tumor, were evaluated for the purpose of planning which tissue to biopsy during surgery. One to four tumor tissue samples from each patient were designated as 5-mm- diameter spherical targets on co-registered MR images using BrainLAB surgical navigation software (BrainLAB Inc.). To minimize risks to the patient, no control tissue (normal brain) was acquired. Image-guided navigation was applied to locate tissue corresponding to planned targets and to acquire safely accessible samples. Upon excision, tissue samples were immediately bisected: half were snap-frozen in liquid nitrogen and stored at -80°C for <sup>1</sup>H HR-MAS spectroscopy; the other half was fixed in 10% zinc formalin, dehydrated by graded ethanols, and embedded in Paraplast Plus wax (McCormick Scientific) using standardized techniques for tissue processing and immunohistochemistry.

### ***<sup>1</sup>H HR-MAS spectroscopy***

Tissue samples weighing between 0.78 and 28.14 mg (mean = 9.56 mg) were loaded into a 35- $\mu$ l zirconia rotor (custom-designed by Varian) with 3  $\mu$ l of 99.9% atom-D deuterium oxide containing 0.75 wt % 3-(trimethylsilyl)propionic acid (Sigma-Aldrich) for chemical shift referencing. Data were acquired at 11.7 T, 1°C, 2250 Hz spin rate in a 4-

mm gHX nanoprobe with a Varian INOVA 500 MHz multinuclear spectrometer. The nanoprobe gHX is an inverse probe, optimized for the direct detection of protons and the indirect detection of X-nuclei ( $^{13}\text{C}$ ,  $^{31}\text{P}$ ,  $^{15}\text{N}$ ) and was equipped with a magic angle gradient coil. A 40 mM phantom solution of 2HG at pH 7 was scanned using the same parameters to provide a basis spectrum for metabolite fitting.

A rotor-synchronized 1D CPMG pulse sequence was run with TR/TE = (4 s)/(144 ms), 512 scans, 40,000 acquired points,  $90^\circ$  pulse, and 20 kHz spectral width for a total time of 35 min. The electronic reference to access *in vivo* concentrations (ERETIC) method was used to generate an artificial electronic signal that served as an external standard for estimation of metabolite levels in 1D spectra (29). A rotor-synchronized adiabatic 2D TOCSY spectrum was acquired with a 40-ms mixing time, 25 transients, 64 increments, saturation delay of 1 s,  $90^\circ$  pulse, and 20 kHz spectral width for a total time of 62 min (13). TOCSY spectra display a signal intensity map of metabolite cross peaks, based on the transferred magnetization between J-coupled protons. Information derived from this sequence is useful for identifying metabolites by their unique spin systems and separating overlapping chemical signals.

Preprocessing of HR-MAS spectra was done in the time domain using the Java-based magnetic resonance user interface (jMRUI) (30). Quantification of relative 1D metabolite levels was achieved with the semiparametric algorithm HR-QUEST, which fits a customized basis set of metabolites to a given spectrum (31). The HR-QUEST basis set used in this study was composed of spectra from 26 metabolites that are commonly studied in the human brain, as well as spectra acquired from a stock solution of 2HG (Sigma-Aldrich) (14). Metabolite levels with less than 10% Cramer-Rao error estimates were included for statistical analysis. Two experienced spectroscopists also evaluated

each spectrum to qualitatively assess goodness of metabolite fits and whether low resolution or SNR compromised its analysis. Tissue samples found by these spectroscopists to have ambiguous or indeterminate interpretations were eliminated from subsequent analyses, whereas the remainder was classified visually as either 2HG-positive (+) or 2HG-negative (-). This enabled a query of the relative prevalence of aberrant 2HG production among glioma grades and histological subtypes, even in cases where 2HG levels were insufficient for HR-QUEST fitting.

### ***Statistical analysis***

All analyses were performed with the statistical software R (version 2.13). To determine differences in 2HG levels by grade, we applied an exact Wilcoxon rank-sum test from the library `coin` to pairwise compare the distribution of 2HG levels between grades. To identify parameters that were related to levels of 2HG, we performed a correlation analysis. In one method, a single tissue sample was selected at random from each patient and the resulting data set was fit according to a simple regression and Kendall tau model. This process was carried out a total of 100 times, with a correlation being considered statistically significant if the  $P$  value for the Kendall tau correlation coefficient was  $\leq 0.05$  in at least 70% of the individual trials. The second method used a simple regression model, which evaluated all of the tissue samples collectively and correcting for correlated responses from the same patient via boot-strap estimation. All statistical methods are presented in Supplementary Material, whereas the latter simple regression model with bootstrapping is presented as the primary analysis (32, 33). Owing to the exploratory nature of this study, adjustment for multiple comparisons was not made and regression coefficients significant at  $P < 0.05$  are summarized as predictors of 2HG concentration.

In all cases, 2HG was treated as the outcome. Note that the correlation analysis excluded those patients and tissue samples with an undetermined or negative *IDH1* mutation status and spectra that could not be fit for 2HG, even if it was visually identified. This reduced the data analyzed for correlations to 25 patients and 46 tissue samples. There were two tissue samples from one patient in which the presence of 2HG had been assumed on the basis of histologic confirmation of *IDH1* mutation, but was not corroborated by HR-MAS spectroscopy. 2HG levels in these samples were set to zero for analysis, because their perceived absence was likely owing to concentrations that fell below the level of detection.

### **References and Notes**

1. J. T. Grier, T. Batchelor, Low-grade gliomas in adults. *Oncologist* 11, 681–693 (2006).
2. M. J. Riemenschneider, G. Reifenberger, Molecular neuropathology of low-grade gliomas and its clinical impact. *Adv. Tech. Stand. Neurosurg.* 35, 35–64 (2010).
3. H. Yan, D. W. Parsons, G. Jin, R. McLendon, B. A. Rasheed, W. Yuan, I. Kos, I. Batinic-Haberle, S. Jones, G. J. Riggins, H. Friedman, A. Friedman, D. Reardon, J. Herndon, K. W. Kinzler, V. E. Velculescu, B. Vogelstein, D. D. Bigner, IDH1 and IDH2 mutations in gliomas. *N. Engl. J. Med.* 360, 765–773 (2009).
4. D. W. Parsons, S. Jones, X. Zhang, J. C. Lin, R. J. Leary, P. Angenendt, P. Mankoo, H. Carter, I. M. Siu, G. L. Gallia, A. Olivi, R. McLendon, B. A. Rasheed, S. Keir, T. Nikolskaya, Y. Nikolsky, D. A. Busam, H. Tekleab, L. A. Diaz Jr., J. Hartigan, D. R. Smith, R. L. Strausberg, S. K. Marie, S. M. Shinjo, H. Yan, G. J. Riggins, D. D. Bigner, R. Karchin, N. Papadopoulos, G. Parmigiani, B. Vogelstein, V. E. Velculescu, K. W. Kinzler, An integrated genomic analysis of human glioblastoma multiforme. *Science* 321, 1807–1812 (2008).

5. C. Houillier, X. Wang, G. Kaloshi, K. Mokhtari, R. Guillevin, J. Laffaire, S. Paris, B. Boisselier, A. Idbah, F. Laigle-Donadey, K. Hoang-Xuan, M. Sanson, J. Y. Delattre, IDH1 or IDH2 mutations predict longer survival and response to temozolomide in low-grade gliomas. *Neurology* 75, 1560–1566 (2010).
6. C. Hartmann, B. Hentschel, W. Wick, D. Capper, J. Felsberg, M. Simon, M. Westphal, G. Schackert, R. Meyermann, T. Pietsch, G. Reifenberger, M. Weller, M. Loeffler, A. von Deimling, Patients with IDH1 wild type anaplastic astrocytomas exhibit worse prognosis than IDH1-mutated glioblastomas, and IDH1 mutation status accounts for the unfavorable prognostic effect of higher age: Implications for classification of gliomas. *Acta Neuropathol.* 120, 707–718 (2010).
7. H.J.Koh, S.M.Lee, B.G.Son, S.H.Lee, Z.Y.Ryoo, K.T.Chang, J.W.Park, D.C.Park, B.J.Song, R. L. Veech, H. Song, T. L. Huh, Cytosolic NADP<sup>+</sup>-dependent isocitrate dehydrogenase plays a key role in lipid metabolism. *J. Biol. Chem.* 279, 39968–39974 (2004).
8. S.H.Jo, M.K.Son, H.J.Koh, S.M.Lee, I.H.Song, Y.O.Kim, Y.S.Lee, K.S.Jeong, W.B.Kim, J. W. Park, B. J. Song, T. L. Huh, Control of mitochondrial redox balance and cellular defense against oxidative damage by mitochondrial NADP<sup>+</sup>-dependent isocitrate dehydrogenase. *J. Biol. Chem.* 276, 16168–16176 (2001).
9. S. M. Lee, H. J. Koh, D. C. Park, B. J. Song, T. L. Huh, J. W. Park, Cytosolic NADP<sup>+</sup>-dependent isocitrate dehydrogenase status modulates oxidative damage to cells. *Free Radic. Biol. Med.* 32, 1185–1196 (2002).
10. L. Dang, D. W. White, S. Gross, B. D. Bennett, M. A. Bittinger, E. M. Driggers, V. R. Fantin, H. G. Jang, S. Jin, M. C. Keenen, K. M. Marks, R. M. Prins, P. S. Ward, K. E. Yen, L. M. Liau, J. D. Rabinowitz, L. C. Cantley, C. B. Thompson, M. G. Vander Heiden,

- S. M. Su, Cancer-associated IDH1 mutations produce 2-hydroxyglutarate. *Nature* 462, 739–744 (2009).
11. D. Capper, H. Zentgraf, J. Balss, C. Hartmann, A. von Deimling, Monoclonal antibody specific for IDH1 R132H mutation. *Acta Neuropathol.* 118, 599–601 (2009).
  12. S. Meiboom, D. Gill, Modified spin-echo method for measuring nuclear relaxation times. *Rev. Sci. Instrum.* 29, 688–691 (1958).
  13. M. G. Swanson, K. R. Keshari, Z. L. Tabatabai, J. P. Simko, K. Shinohara, P. R. Carroll, A. S. Zektzer, J. Kurhanewicz, Quantification of choline- and ethanolamine-containing metabolites in human prostate tissues using <sup>1</sup>H HR-MAS total correlation spectroscopy. *Magn. Reson. Med.* 60, 33–40 (2008).
  14. V. Govindaraju, K. Young, A. A. Maudsley, Proton NMR chemical shifts and coupling constants for brain metabolites. *NMR Biomed.* 13, 129–153 (2000).
  15. R. Srinivasan, J. J. Phillips, S. R. Vandenberg, M. Y. Polley, G. Bourne, A. Au, A. Pirzkall, S. Cha, S. M. Chang, S. J. Nelson, Ex vivo MR spectroscopic measure differentiates tumor from treatment effects in GBM. *Neuro Oncol.* 12, 1152–1161 (2010).
  16. S. J. Nelson, Assessment of therapeutic response and treatment planning for brain tumors using metabolic and physiological MRI. *NMR Biomed.* 24, 734–749 (2011).
  17. S. Zhao, Y. Lin, W. Xu, W. Jiang, Z. Zha, P. Wang, W. Yu, Z. Li, L. Gong, Y. Peng, J. Ding, Q. Lei, K. L. Guan, Y. Xiong, Glioma-derived mutations in IDH1 dominantly inhibit IDH1 catalytic activity and induce HIF-1 $\alpha$ . *Science* 324, 261–265 (2009).
  18. R. Chowdhury, K. K. Yeoh, Y. M. Tian, L. Hillringhaus, E. A. Bagg, N. R. Rose, I. K. H. Leung, X. S. Li, E. C. Y. Woon, M. Yang, M. A. McDonough, O. N. King, I. J. Clifton, R. J. Klose, T. D. W. Claridge, P. J. Ratcliffe, C. J. Schofield, A. Kawamura, The oncometabolite 2-hydroxyglutarate inhibits histone lysine demethylases. *EMBO Rep.* 12, 463–469 (2011).

19. C. Choi, G. Sandeep, R. DeBerardinis, Z. Kovacs, R. Bachoo, J. Pascual, I. Dimitrov, B. Mickey, C. Malloy, E. Maher, In vivo detection of IDH mutations in gliomas by 1H-MRS. *Proc. Intl. Soc. Mag. Reson. Med.* 19, 181 (2011).
20. R. Nagarajan, M. A. Thomas, W. B. Pope, R. M. Prins, N. Wilson, N. Salamon, L. M. Liau, Detection of 2-hydroxyglutarate in mutant brain tumors in vivo using proton magnetic resonance spectroscopy. *Proc. Intl. Soc. Mag. Reson. Med.* 19, 184 (2011).
21. O. C. Andronesi, G. Kim, E. Gerstner, T. Batchelor, A. A. Tzika, V. R. Fantin, M. G. Vander Heiden, A. G. Sorensen, Detection of 2-hydroxyglutarate in IDH-mutated glioma patients by in vivo spectral-editing and 2D correlation magnetic resonance spectroscopy. *Sci. Transl. Med.* 4, 116ra4 (2012).
22. P. Paschka, R. F. Schlenk, V. I. Gaidzik, M. Habdank, J. Krönke, L. Bullinger, D. Späth, S. Kayser, M. Zucknick, K. Götze, H. A. Horst, U. Germing, H. Döhner, K. Döhner, IDH1 and IDH2 mutations are frequent genetic alterations in acute myeloid leukemia and confer adverse prognosis in cytogenetically normal acute myeloid leukemia with NPM1 mutation without FLT3 internal tandem duplication. *J. Clin. Oncol.* 28, 3636–3643 (2010).
23. M. Aghili, F. Zahedi, E. Rafiee, Hydroxyglutaric aciduria and malignant brain tumor: A case report and literature review. *J. Neurooncol.* 91, 233–236 (2009).
24. K. E. Yen, M. A. Bittinger, S. M. Su, V. R. Fantin, Cancer-associated IDH mutations: Biomarker and therapeutic opportunities. *Oncogene* 29, 6409–6417 (2010).
25. Z. J. Reitman, H. Yan, Isocitrate dehydrogenase 1 and 2 mutations in cancer: Alterations at a crossroads of cellular metabolism. *J. Natl. Cancer Inst.* 102, 932–941 (2010).



26. I. Park, A. P. Chen, M. L. Zierhut, E. Ozturk-Isik, D. B. Vigneron, S. J. Nelson, Implementation of 3 T lactate-edited 3D 1H MR spectroscopic imaging with flyback echo-planar readout for gliomas patients. *Ann. Biomed. Eng.* 39, 193–204 (2011).
27. P. J. Basser, C. Pierpaoli, Microstructural and physiological features of tissues elucidated by quantitative-diffusion-tensor MRI. *J. Magn. Reson. B* 111, 209–219 (1996).
28. T. R. McKnight, S. M. Noworolski, D. B. Vigneron, S. J. Nelson, An automated technique for the quantitative assessment of 3D-MRSI data from patients with glioma. *J. Magn. Reson. Imaging* 13, 167–177 (2001).
29. M. J. Albers, T. N. Butler, I. Rahwa, N. Bao, K. R. Keshari, M. G. Swanson, J. Kurhanewicz, Evaluation of the ERETIC method as an improved quantitative reference for 1H HR-MAS spectroscopy of prostate tissue. *Magn. Reson. Med.* 61, 525–532 (2009).
30. D. Stefan, F. Di Cesare, A. Andrasescu, E. Popa, A. Lazariev, E. Vescovo, O. Strbak, S. Williams, Z. Starcuk, M. Cabanas, D. van Ormondt, D. Graveron-Demily, Quantitation of magnetic resonance spectroscopy signals: The jMRUI software package. *Meas. Sci. Technol.* 20, 104035 (2009).
31. H. Ratiney, M. J. Albers, H. Rabeson, J. Kurhanewicz, Semi-parametric time-domain quantification of HR-MAS data from prostate tissue. *NMR Biomed.* 23, 1146–1157 (2010).
32. Z. Feng, D. McLerran, J. Grizzle, A comparison of statistical methods for clustered data analysis with Gaussian error. *Stat. Med.* 15, 1793–1806 (1996).
33. F. E. Harrell Jr., *Regression Modeling Strategies: With Applications to Linear Models, Logistic Regression and Survival Analysis* (Springer, New York, 2001).

### **Acknowledgments**

We would like to acknowledge support from the Brain Tumor Research Center at University of California, San Francisco (UCSF) in collecting the tissue samples, as well as the Magnetic Resonance Laboratory personnel at UCSF for the use of their spectrometer. We would also like to express our gratitude to S. Ronen, J. Kurhanewicz, K. Keshari, and R. Iman for their assistance and guidance during this project, and to J. Crane and B. Olson for the development of the SIVIC software package and the implementation of HR-QUEST.

### **Funding sources**

This work was supported by funds from the NIH, which included the Brain Tumor SPORE P50CA097257 and K08 NS063456 grants.

### **Author contributions**

G.B. performed the patient consenting, presurgical MR scanning, and tissue sample planning. G.B. and M.S.B. acquired the tissue samples. A.E., L.E.J., and H.A.I.Y. performed the NMR experiments and analyzed the data. J.J.P. performed the *IDH1* immunohistochemistry, genetic sequencing, and pathology analysis. R.P. performed the statistical analyses. A.E. and L.E.J. wrote the paper with assistance from H.A.I.Y., J.J.P., and S.J.N. M.S.B., R.S., S.M.C., S.C., and S.J.N. conceived and designed the experiments and analyzed the data. Competing interests: The authors declare that they have no competing interests.

### **Supplementary Methods**

### ***Histopathology and IDH1 immunohistochemistry***

All biopsies were reviewed and scored by a board-certified neuropathologist blinded to the 2HG status of the tumor. The following antibodies were used: rabbit polyclonal MIB-1 anti-Ki67 (30- 9) (Ventana Medical Systems) at 2 µg/ml for 32 min at 37°C; mouse anti-SMI-31 (Covance) at 1.5 µg/ml for 8 min at 37°C; rabbit polyclonal Factor VIII (Dako) at 1.2 µg/ml for 20 min at 37°C; and mouse monoclonal anti-*IDH1*<sub>R132H</sub> (DIA H09) (Dianova) at 1:50 µg for 32 min at 37°C (11). Heat antigen retrieval for MIB-1 was performed for 30 min in citrate buffer at pH 6. *IDH1*<sub>R132H</sub> and Factor VIII staining was performed in Tris-EDTA buffer at pH 8. Following antigen retrieval, sections were treated with 3% methanol-hydrogen peroxide for 16 min at 22°C. All immunohistochemistry assays were performed on the Ventana Medical Systems Benchmark XT.

Slides stained with H&E, MIB-1, and SMI-31 were then scored. For H&E-stained slides, a tumor score was given on the basis of the contribution of tumor cellularity to total cellularity. A score of 0 denoted neuropil without tumor; 1 indicated an infiltrating tumor margin containing detectable but not abundant—numbers of tumor cells; 2 denoted a more cellular-infiltrated zone; 3 denoted highly cellular tumor with few non-neoplastic cells. Total cell-density was also determined as an average number of cells per 200" field to complement measures of tumor score and to provide a means of normalizing *ex vivo* metabolite levels. Tissue samples with a tumor score of 0 were excluded from analysis.

For MIB-1-stained slides, a labeling index [(MIB-1-positive nuclei per total tumor cells counted per 200x field) " 100%] was calculated based on the evaluation of at least three fields and >1000 cells. A score was then generated by subdividing the labeling index

according to approximate grade ranges for mitotic activity: 1 (<4); 2 (4-<10); 3 (10-20); 4(>20). For SMI31- stained slides, a score was assigned to each slide on the basis of the extent of disruption of the normal axonal architecture. A score of 0 denoted no disruption; 1 denoted minimal disruption; 2 denoted mild disruption; 3 denoted severe disruption.

For *IDH1*<sub>R132H</sub>-stained slides, each biopsy was qualitatively scored on the basis of the percentage of tumor cells that stained positive for R132H using a four-tier scale: 0, no immunostaining; 1, >0 and < 25% positive; 2, between 25 and 75% positive; and 3, >75% tumor cells positive.

### ***Tumor vascularity***

On the basis of H&E staining and Factor VIII immunohistochemistry, the microvascular morphology was graded as delicate (resembling normal cerebral vessels), simple vascular hyperplasia (circumferential hyperplasia with definitive lumen), or complex microvascular hyperplasia (glomeruloid-type vessels). An overall score for Factor VIII was derived from its relative contribution to total vascularity using a four-tier ordinal scale (0, no contribution; 1, minimal; 2, prevalent; 3, extensive) at a magnification of 200x. Digital images were captured using a microscope (Olympus, Model BX41TF) and digital camera (Olympus, Model DP70).

### ***Genetic sequencing***

Genetic analysis of *IDH1* mutation status was determined on genomic DNA extracted from formalin-fixed paraffin-embedded tumor tissue. Briefly, a 129-bp length fragment spanning the catalytic domain of *IDH1*, including codon 132, was amplified by PCR (S1). PCR products were purified using the PCR Purification kit (Qiagen) and the amplicon

was sequenced in both the forward (5'-ACCAAATGGCACCATACGA-3') and reverse (5'-GCAAATCACATTATTGCCAAC-3') directions for *IDH1*. The cycling conditions were 95°C for 5 min; 30 cycles of 95°C for 30 s, 56°C for 40 s, and 72°C for 50 s; and 72°C for 5 min. Sequencing was performed in order to probe for non-histidine mutations in discordant patients, as well as further corroborate R132H antibody staining in concordant cases. A total of 10 samples were sequenced, including 3 discordant cases, 4 concordant cases, and positive and negative control cases. Electropherograms were generated with 4 Peaks visualization software (Mekentosj). *IDH2* mutations were not examined in this study.

#### ***In vivo post-processing of ADC data***

The acquisition of diffusion tensor images enabled the calculation of eigenvalues, from which a number of descriptive measures of diffusion were evaluated. The first eigenvalue ( $\lambda_1$ ) is the magnitude of the primary direction of diffusion, while the combination of  $\lambda_2$  and  $\lambda_3$  provides a measure of radial diffusivity that was defined as  $(\lambda_2 + \lambda_3)/2$  ( $S_2$ ). Eigenvalues and parameter maps derived from *in vivo* DWI and MRSI data were evaluated at the originating site of each tissue sample. Tissue sample locations were defined using the spatial coordinates captured by BrainLAB software at the time of surgery. Intensities from a 5-mm-diameter ROI centered on the site of tissue extraction were analyzed. Image intensities were normalized by the mode of their values in a ROI corresponding to the overall brain tissue, as calculated from the histogram of ADC values. This normalization factor agreed well with the median ADC value in normal-appearing white matter.

### ***J-resolved spectroscopy and spectral simulation of 2HG in phantom***

2D *J*-resolved spectra (S3) were acquired at 500 MHz with a 5 mm inverse probe at pH 7.0 and 1°C. The pulse sequence consisted of a 2-s low-power pulse to saturate the water resonance, followed by a 90° hard pulse, a varying delay with a 180° hard pulse and a second delay of the same length, then an acquisition of 204.6 ms. The spectral width in F2 was 2766 Hz and 60 Hz in F1, with 128 increments. Spectra were processed in magnitude mode with unshifted sine-bell window functions in both dimensions and rotated 45° to place the multiplet cross-peaks orthogonal to the F2 axis. This experiment allowed sufficient resolution of the peaks to determine all the chemical shifts and deconvoluted the  $\alpha$ - and  $\gamma$ -proton multiplets such that their respective *dd* and *ddd* coupling constants could be obtained. The  $\beta$ -multiplets remained too complicated for first-order analysis, but the  $J_{\beta_1-\beta_2}$  was measured using the selective excitation and refocusing (SERF) variant of the *J*-resolved experiment (S4) with an excitation band-selective uniform response pure phase (EBURP) pulse to selectively excite the  $\beta_1$ -multiplet and a refocusing EBURP pulse to refocus both  $\beta_1$  and  $\beta_2$  resonances. Spectral simulation was performed using NUTS software (Acorn NMR Inc.).

### ***Ultra-high magnetic field applied to the separation of 2HG $\beta$ -resonances***

A 40 mM phantom solution of 2HG dissolved in D<sub>2</sub>O with pH 7 was scanned on a 800 MHz Bruker 18.8 Tesla NMR spectrometer using a cryoprobe. For chemical referencing, 1.5  $\mu$ l of 99.9% atom-D D<sub>2</sub>O containing 0.75 wt% 3-(trimethylsilyl)propionic acid (Sigma Aldrich) were added to the phantom. A pulse-acquire presaturation (PRESAT) sequence defined by the Bruker ZGPR pulse program was employed with sweep width = 40 kHz, TR = 7 s, 300 scans at 2 s each, and 5 s for presaturation of the water resonance. Post-

processing of acquired PRESAT spectra was performed using Bruker TOPSPIN and ACD 1D NMR Processor software.

### **Supplementary Figure and Table Legends**

**Fig. 3.S1 *J*-coupling constants and spectral simulation of 2HG.** (A) Chemical structure of 2HG is presented alongside corresponding spectra: the blue trace shows the reference CPMG spectrum of 2HG acquired from a phantom using  $^1\text{H}$  HR-MAS spectroscopy; the red trace represents the optimized spectral simulation achieved (Acorn NUTS). The table contains the vicinal and geminal *J*-coupling constants and chemical shifts determined from the simulation of 2HG's molecular spin system after performing *J*-resolved experiments to find estimates for some of these parameters. (B and C) An enhanced view of the spectra in (A) is shown for the  $\alpha$ -proton (B) and  $\beta$ - and  $\gamma$ -protons (C).

**Fig. 3.S2 Separation of 2HG  $\gamma$ -resonances at ultrahigh field strength.** PRESAT spectrum acquired from a 2HG phantom using an 800 MHz 18.8 Tesla NMR spectrometer. The  $\gamma$ -resonances previously referenced in fig. S1 are separable at the high magnetic field strength owing to the enhanced spectral resolution. Each of the respective resonances displays a splitting pattern of seven peaks that is defined by  $\gamma$ -protons' mutual coupling with one another and the  $\beta$ -protons.

**Fig. 3.S3 Plots of 2HG correlations with *ex vivo* metabolites, histopathology, and *in vivo* MR imaging parameters.** These plots were analyzed with the simple regression model, which evaluated all of the tissue samples collectively and corrected for correlated responses from the same patient via bootstrap estimation. Regression coefficients ( $\beta$ ) and the number of tissue samples evaluated for each parameter (*n*) are presented along

with statistical significance. All metabolite levels are given in relative units. Tumor score is shown as a three-tier classification based on the relative contribution of tumor cells to overall cellularity. The MIB-1 index measures the proportion of tumor cells undergoing mitosis to overall cellularity and was divided into four tiers for classification. Delicate vascularity was characterized using a four-tier scale for Factor VIII immunostaining. Bet, betaine; GSH, glutathione; MCI, *myo*-inositol-to-tCHO index;  $n\lambda_1$  and  $n\lambda_2$ , normalized eigenvalues for principle and secondary components of water diffusion, respectively.

**Table 3.S1 Complete patient data for 2HG presence and IDH1 mutation status. (A)**

Clinicopathological data are presented for included patients ( $n = 52$ ), with *IDH1* and 2HG results for each tissue sample analyzed ( $n = 104$ ). 2HG presence was visually confirmed as present (1), absent (0), or indeterminate on the basis of inadequate spectral quality.

*IDH1* immunohistochemistry (IHC) was qualitatively scored on the basis of the percentage of tumor cells that stained positive for R132H using a four-tier scale: 0, no immunostaining; 1, >0 and <25% positive; 2, between 25 and 75% positive; and 3, >75% tumor cells positive. The IHC score was used in conjunction with genetic sequencing of a 10-patient subset to determine *IDH1* mutation status. Concordance was evaluated on the basis of the agreement between the presence of 2HG and *IDH1* mutations by IHC or sequencing of genomic DNA (C, concordant; D, discordant). (B) Some samples were excluded from analysis ( $n = 23$ ). Tissue samples contaminated by methanol during surgery ( $n = 14$ ) or were too small to scan ( $n = 6$ ) were not analyzed with neuropathology. Spectra obtained from the samples that did not contain tumor ( $n = 3$ ) were also excluded. Glioma histological subtypes: AS, astrocytoma; OA, oligoastrocytoma; OD, oligodendroglioma.

**Table 3.S2 Correlation statistics including an additional statistical method.** Each of



the study parameters correlated with 2HG is presented along with the statistical methods that were used to report significance. Method A summarizes the median simple regression coefficient and *P* value from the repeated random sampling. Method B used only a simple regression model and evaluated all of the tissue samples collectively while correcting for correlated responses via bootstrap estimation. NS, not significant.

### **Supplementary References**

1. I.F. Pollack, R.L. Hamilton, R.W. Sobol, M.N. Nikiforova, M.A. Lyons-Weiler, W.A. Laframboise, P.C. Burger, D.J. Brat, M.K. Rosenblum, E.J. Holmes, T. Zhou, R.I. Jakacki, IDH1 mutations are common in malignant gliomas arising in adolescents: a report from the Children's Oncology Group. *Childs Nerv. Syst.* **27**, 87-94 (2010).
2. P. Mukherjee, J.I. Bermann, S.W. Chung, C.P. Hess, R.G. Henry, Diffusion tensor imaging and fiber tractography: theoretical underpinnings. *Am. J. Neuroradiol.* **29**, 632-641 (2008).
3. W. P. Aue, J. Karhan, R. R. Ernst, Homonuclear broad band decoupling and two-dimensional *J*-resolved NMR spectroscopy, *J. Chem. Phys.* **64**, 4226–4227 (1976).
4. T. Fäcke, S. Berger, SERF, a new method for H,H spin-coupling measurement in organic chemistry, *J. Magn. Reson.* **113**, 114–116 (1995)

## Supplementary Figures and Tables

Fig. 3.S1 J-coupling constants and spectral simulation of 2HG.

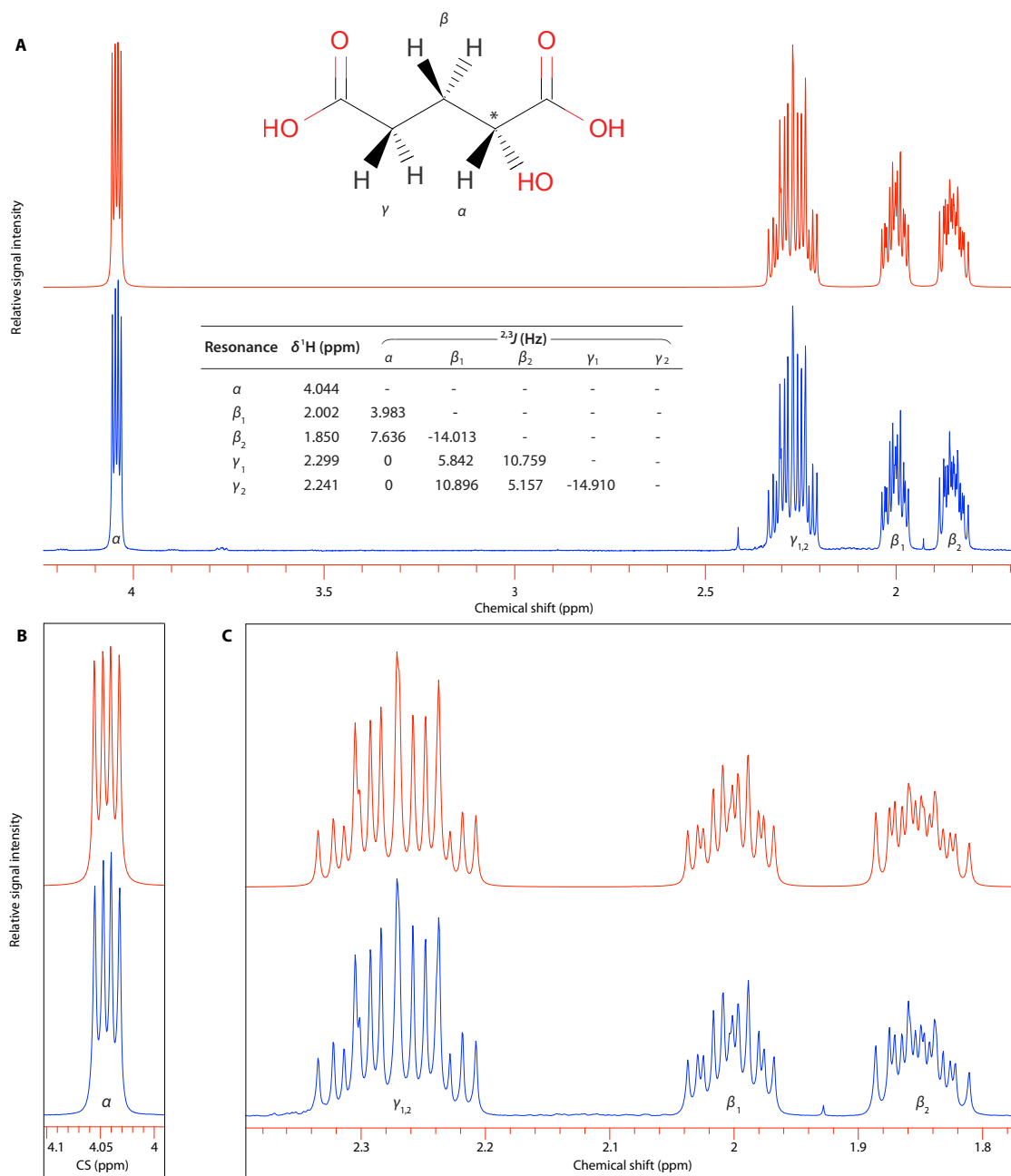


**Fig. 3.S2 Separation of 2HG  $\beta$ -resonances at ultrahigh field strength.**

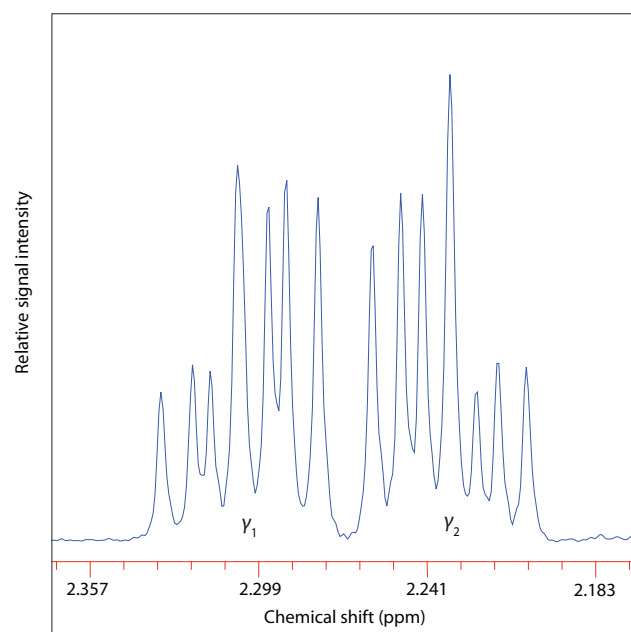


**Fig. 3.S3 Plots of 2HG correlations with ex vivo metabolites, histopathology, and in vivo MR imaging parameters.**

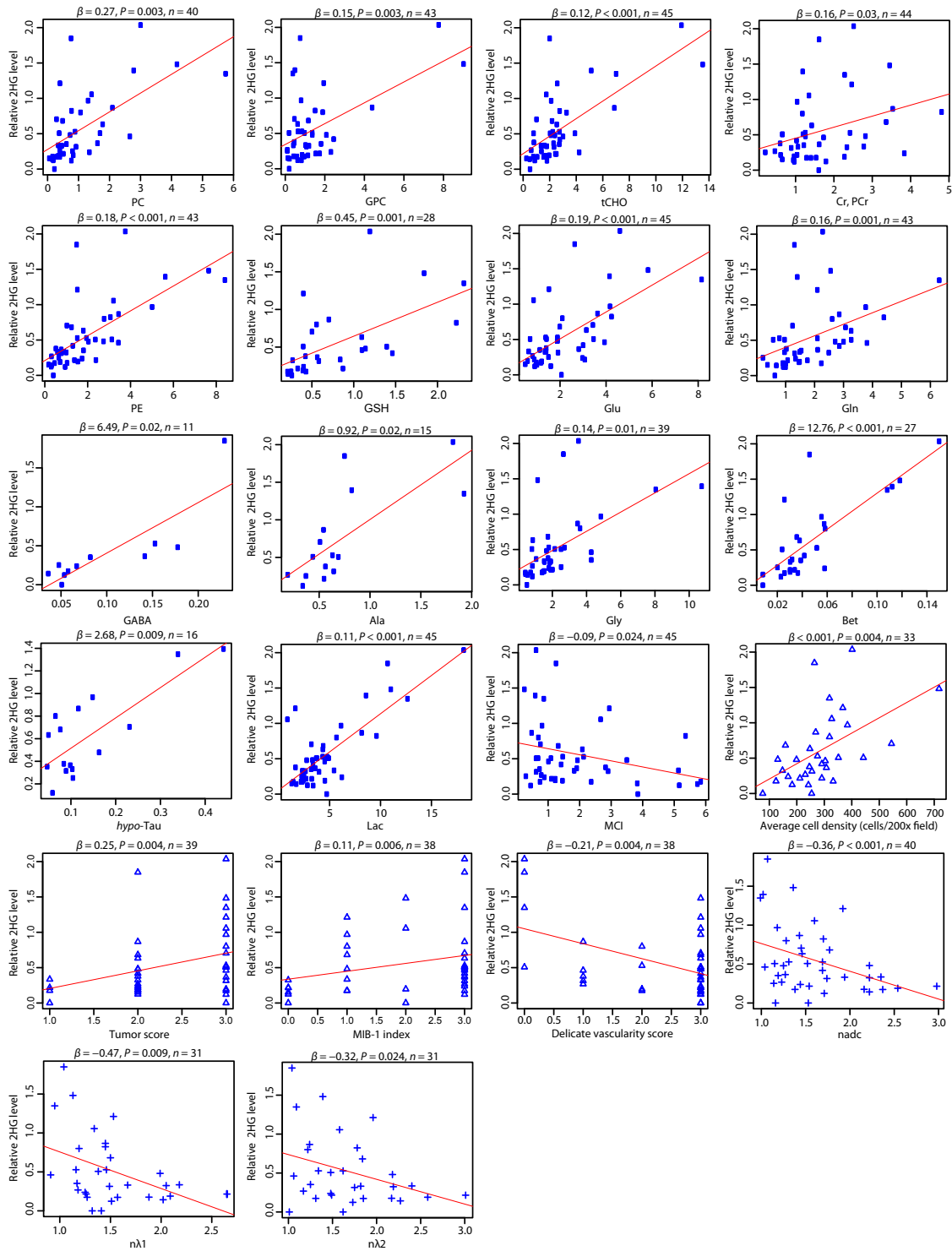


**Table 3.S1 Complete patient data for 2HG presence and IDH1 mutation status.**

(A) Samples included in analysis ( <i>n</i> = 52 patients, for a total of 104 tissue samples)											
Subject ID	Age at diagnosis	Gender	Histological tumor classification	WHO tumor grade	Tissue ID	Tissue mass (mg)	2HG presence	IDH1 <sub>R132H</sub> IHC score	DNA seq.	Tissue sample concordance	Ex vivo 2HG levels
1	33	Female	OD	2	1A	15.82	1	2	R132H	C	NA
2	40	Male	AS	3	2A	4.18	1	Indeterminate	-	Indeterminate	1.0561
					2B	9.75	1	3	R132H	C	1.2118
3	30	Female	OA	2	3A	8.78	1	0	-	D	0.77511
4	35	Female	AS	2	4A	1.54	Indeterminate	2	-	Indeterminate	NA
					4B	2.74	Indeterminate	2	-	Indeterminate	NA
5	40	Female	AS	3	5A	13.26	1	Indeterminate	-	Indeterminate	0.18919
					5B	7.58	Indeterminate	2	-	Indeterminate	NA
6	36	Female	AS	3	6A	14.22	Indeterminate	Indeterminate	R132H	Indeterminate	NA
					6B	14.09	Indeterminate	3	-	Indeterminate	NA
					6C	11.22	Indeterminate	3	-	Indeterminate	NA
7	55	Male	OA	2	7A	5.45	1	1	-	C	0.15138
8	70	Male	OD	3	8A	11.01	1	0	-	D	0.8666
					8B	19.42	1	2	-	C	0.23798
9	24	Male	AS	2	9A	4.01	Indeterminate	0	-	Indeterminate	NA
10	40	Female	OD	2	10A	9.76	1	2	-	C	0.48086
					10B	10.24	1	2	-	C	0.32429
11	47	Female	OD	2	11A	1.88	Indeterminate	0	-	Indeterminate	NA
12	33	Male	OD	2	12A	8.46	1	3	-	C	0.21623
13	44	Male	OD	3	13A	12.42	1	3	-	C	2.0359
					13B	20.3	1	3	-	C	0.17338
14	36	Male	OA	3	14A	20.84	Indeterminate	1	-	Indeterminate	NA
15	41	Male	OA	2	15A	15.3	0	0	-	C	NA
					15B	11.44	0	0	-	C	NA
16	52	Female	OD	3	16A	16.01	0	3	R132H	D	NA

					16B	9.8	0	0	-	C	NA
17	54	Male	OD	3	17A	17.91	Indeterminate	1	-	Indeterminate	NA
					17B	16.29	1	3	-	C	1.4816
18	40	Male	OD	2	18A	12.15	Indeterminate	2	-	Indeterminate	NA
					18B	10.9	Indeterminate	3	-	Indeterminate	NA
19	32	Female	AS	2	19A	4.9	0	0	-	C	NA
20	62	Female	OA	3	20A	5.05	1	0	-	D	0.841
					20B	12.92	1	0	-	D	NA
					20C	4.02	Indeterminate	Indeterminate	-	Indeterminate	NA
21	30	Female	OD	2	21A	9.5	Indeterminate	1	-	Indeterminate	NA
					21B	8.94	1	3	-	C	0.12361
					21C	4.63	Indeterminate	3	-	Indeterminate	NA
22	44	Female	OD	3	22A	9.53	1	3	-	C	0.50618
					22B	10.91	1	3	R132H	C	0.96739
					22C	2.55	1	3	-	C	0.70465
23	58	Female	AS	4	23A	22.39	1	3	-	C	0.46153
					23B	8.02	1	3	-	C	1.3481
24	35	Male	AS	3	24A	4.5	1	2	R132H	C	0.21546
					24B	8.9	Indeterminate	2	R132H	Indeterminate	NA
25	54	Female	OD	4	25A	6.45	1	3	-	C	0.26797
					25B	1.69	1	3	-	C	0.50681
					25C	8.19	1	3	-	C	1.8485
26	34	Male	OD	3	26A	19.45	1	Indeterminate	-	Indeterminate	0.68134
					26B	5.87	1	1	-	C	0.17424
27	46	Female	AS	2	27A	12.44	Indeterminate	3	-	Indeterminate	NA
					27B	0.78	Indeterminate	3	-	Indeterminate	NA
28	38	Male	OD	2	28A	7.25	Indeterminate	3	-	Indeterminate	NA
					28B	2.32	Indeterminate	3	-	Indeterminate	NA
29	45	Female	AS	2	29A	1.61	Indeterminate	0	-	Indeterminate	NA
					29B	9.13	1	0	-	D	0.27862
30	42	Male	AS	4	30A	23.12	0	0	-	C	NA
					30B	12.6	Indeterminate	0	-	Indeterminate	NA
31	41	Male	OA	4	31A	13.44	1	2	-	C	0.4187
					31B	20.36	1	2	-	C	0.63296
					31C	8.89	1	2	-	C	0.47866
					31D	25.46	1	3	-	C	0.36482
32	50	Male	AS	3	32A	18.32	1	1	R132H	C	NA
					32B	2.95	Indeterminate	3	-	Indeterminate	NA
33	20	Female	OA	2	33A	2.3	Indeterminate	0	-	Indeterminate	NA
					33B	8.37	Indeterminate	Indeterminate	-	Indeterminate	NA
					33C	4.78	Indeterminate	0	-	Indeterminate	NA
34	41	Male	OD	3	34A	4.11	1	0	R132S	C	0.37777
					34B	6.57	Indeterminate	0	-	Indeterminate	NA
35	44	Female	OD	3	35A	5.08	Indeterminate	2	-	Indeterminate	NA
					35B	10.44	Indeterminate	2	-	Indeterminate	NA
36	55	Female	OD	2	36A	6.26	1	3	-	C	0.33096

					36B	10.3	1	3	-	C	0.52739
37	69	Male	OD	3	37A	12.31	1	3	-	C	NA
					37B	9.86	1	2	-	C	0.12027
38	41	Female	OD	2	38A	4.88	1	2	-	C	NA
					38B	1.3	Indeterminate	2	-	Indeterminate	NA
39	47	Male	AS	3	39A	3.36	Indeterminate	3	-	Indeterminate	NA
40	62	Male	OA	3	40A	7.98	Indeterminate	3	-	Indeterminate	NA
					40B	4.82	Indeterminate	3	-	Indeterminate	NA
					40C	3.44	Indeterminate	3	-	Indeterminate	NA
41	48	Male	AS	3	41A	23.19	1	0	-	D	0.36647
					41B	14.97	1	Indeterminate	-	Indeterminate	NA
42	38	Female	AS	3	42A	14.94	1	3	-	C	0.14237
					42B	18.02	1	2	-	C	0.82295
43	35	Male	OD	3	43A	14.4	1	3	-	C	0.50748
					43B	4.54	1	3	-	C	0.19561
44	37	Female	AS	3	44A	9.09	1	0	R132S	C	0.17568
					44B	23.26	1	Indeterminate	-	Indeterminate	0.33454
45	41	Female	AS	3	45A	3.66	Indeterminate	0	R132H	Indeterminate	NA
46	54	Female	AS	4	46A	8.3	1	2	-	C	0.25229
					46B	2.71	1	2	-	C	1.3945
47	41	Male	OA	3	47A	4.3	1	3	-	C	0.31436
					47B	4.25	1	3	-	C	0.80039
					47C	4.9	1	3	-	C	NA
					47D	8.9	1	2	-	C	0.35262
48	44	Male	AS	3	48A	4.05	1	0	-	D	0.39061
49	43	Male	OD	2	49A	7.56	1	3	-	C	NA
					49B	4.95	Indeterminate	3	-	Indeterminate	NA
50	55	Female	OD	2	50A	8.11	1	3	-	C	0.52825
					50B	10.21	1	3	-	C	NA
51	35	Female	OD	2	51A	3.07	Indeterminate	3	-	Indeterminate	NA
					51B	2.78	Indeterminate	1	-	Indeterminate	NA
52	70	Male	AS	4	52A	28.14	0	0	-	C	NA
					52B	11.72	0	0	-	C	NA

(B) Samples excluded from analysis ( $n = 8$  patients;  $n = 23$  tissue samples)

Subject ID	Age	Gender	Histological tumor classification	WHO tumor grade	Tissue ID	Reason(s) for exclusion	Type of exclusion
14	36	Male	OA	3	14B	Methanol contamination	Sample only
17	54	Male	OD	3	17C	Too small / Poor tissue integrity	Sample only
24	35	Male	AS	3	24C	Methanol contamination	Sample only
30	42	Male	AS	4	30C	No tumor cells present	Sample only
35	44	Female	OD	3	35C	Methanol contamination	Sample only
					35D	Too small / Poor tissue integrity	Sample only
39	47	Male	AS	3	39B	Too small / Poor tissue integrity	Sample only
43	35	Male	OD	3	43C	Methanol contamination	Sample only
45	41	Female	AS	3	45B	Too small / Poor tissue integrity	Sample only
48	44	Male	AS	3	48B	Too small / Poor tissue integrity	Sample only
53	61	Female	OD	2	53A	Too small / Poor tissue integrity	Patient

54	27	Female	AS	2	54A	No tumor cells present	Patient
					54B	No tumor cells present	-
55	43	Male	OA	3	55A	Methanol contamination	Patient
56	59	Male	OD	3	56A	Methanol contamination	Patient
					56B	Methanol contamination	-
					56C	Methanol contamination	-
57	35	Male	OD	2	57A	Methanol contamination	Patient
					57B	Methanol contamination	-
58	54	Female	OA	3	58A	Methanol contamination	Patient
59	41	Male	AS	3	59A	Methanol contamination	Patient
					59B	Methanol contamination	-
60	28	Female	AS	3	60A	Methanol contamination	Patient



**Table 3.S2 Correlation statistics including an additional statistical method.**

	<b>Variables correlated with 2HG</b>	<b>Number of patients</b>	<b>Number of tissue samples</b>	<b>Statistical method A [coefficient (<i>P</i> value)]</b>	<b>Statistical method B [coefficient (<i>P</i> value)]</b>
<b>Ex vivo metabolites</b>	PC	23	40	0.29 (< 0.001)	0.27 (0.003)
	GPC	25	43	NS	0.15 (0.003)
	Cho	25	43	0.48 (0.05)	NS
	tCHO	25	45	0.12 (<0.001)	0.12 (<0.001)
	Cr, PCr	25	44	NS	0.16 (0.03)
	PE	25	43	0.18 (<0.001)	0.18 (<0.001)
	GSH	18	28	0.5 (0.008)	0.45 (0.001)
	Glu	25	45	0.2 (<0.001)	0.19 (<0.001)
	Gln	25	43	0.2 (0.016)	0.16 (0.001)
	Asp	15	22	0.18 (0.034)	NS
	GABA	11	11	6.49 (0.001)	6.49 (0.02)
	Ala	12	15	0.91 (0.005)	0.92 (0.02)
	Gly	24	39	0.13 (0.002)	0.14 (0.01)
	Thr	19	27	0.47 (0.012)	NS
Bet	19	27	12.54 (<0.001)	12.76 (<0.001)	
	<i>hypo</i> -Tau	10	16	NS	2.68 (0.009)
	Lac	25	45	0.11 (<0.001)	0.11 (<0.001)
	MCI	25	45	NS	-0.09 (0.024)
<b>Histopathology parameters</b>	Average cell density	18	33	<0.001 (0.004)	<0.001 (0.002)
	Tumor score	22	39	NS	0.25 (0.004)
	MIB-1 index	21	38	NS	0.11 (0.006)
	Delicate vascularity	21	38	NS	-0.21 (0.004)
<b>In vivo diffusion parameters</b>	ADC	21	40	NS	<0.001 (<0.001)
	<i>n</i> ADC	21	40	NS	-0.36 (<0.001)
	$\lambda_1$	18	31	NS	<0.001 (0.007)
	<i>n</i> $\lambda_1$	18	31	NS	-0.47 (0.009)
	<i>n</i> $\lambda_2$	18	31	NS	-0.32 (0.024)

## **CHAPTER 4: Magnetic Resonance Analysis of Malignant Transformation in Recurrent Glioma**

---

In this project, we performed advanced analysis of multi-parametric MR imaging and spectroscopy to characterize patients with recurrent glioma that had undergone malignant transformation to a higher-grade lesion. We utilized volumetric and intensity imaging analysis, bioinformatics data-visualization, and multi-variate logistical regression modeling to improve our understanding and ability to non-invasively detect this transformation.

---

Authors:

Llewellyn E. Jalbert, Evan Neill, Joanna J. Phillips, Janine M. Lupo, Marram P. Olson, Annette M. Molinaro, Mitchel S. Berger, Susan M. Chang, and Sarah J. Nelson

## **Abstract**

**Introduction:** Patients with low-grade glioma have a relatively long survival and a balance is often struck between treating the tumor and impacting quality of life. While lesions may remain stable for many years, they may also undergo malignant transformation (MT) at the time of recurrence and require more aggressive intervention. Here we report on a state-of-the-art multiparametric magnetic resonance (MR) imaging study of patients with recurrent LGG.

**Methods:** One-hundred and twenty-one patients previously diagnosed with a LGG were scanned in either a 1.5 or 3T MR scanner at the time of recurrence. Volumetric and intensity parameters were estimated from anatomic, diffusion, perfusion and metabolic MR data. Direct comparisons of histopathological markers from image-guided tissue samples with metrics derived from the corresponding locations on the *in vivo* images were made. A bio-informatics approach was applied to visualize and interpret these results that included imaging heatmaps and network analysis. Multivariate linear-regression modeling was utilized for predicting malignant transformation.

**Results:** Many advanced imaging parameters were found to be significantly different for patients with tumors that had undergone MT versus those that had not. Imaging metrics calculated at the tissue sample locations highlighted the distinct biological significance of the imaging and the heterogeneity present in recurrent LGG, while multivariate modeling yielded an accuracy of 76.04% for predicting MT.

**Conclusion:** The acquisition and quantitative analysis of such multiparametric MR data may ultimately allow for improved clinical assessment and treatment stratification for patients with recurrent low grade glioma.

## **Introduction**

Infiltrating low-grade gliomas (LGGs) are a class of terminal central nervous system tumors that comprise malignant neuroglia. Histopathological diagnosis of tumor grade is performed using criteria set by the World Health Organization (WHO) and is based on factors that include nuclear atypia, proliferative capacity, tumor neovascularization, and necrosis [1]. The clinical outcome for patients with LGG is variable, with some lesions following a more indolent disease course, while others recur more rapidly and often after undergoing MT to a higher grade [2]. Lesions that have upgraded to a Grade III anaplastic glioma or Grade IV secondary glioblastoma multiforme (GBM) are managed with additional, more aggressive treatments. To date, little is known regarding the nature of recurrent disease, and the most significant prognostic factors for patients diagnosed with a LGG are the presence of somatic driver mutations in the *Isocitrate Dehydrogenase 1 & 2 (IDH1/2)* oncogenes and the co-deletion of the 1p and 19q chromosomal arms, which have been associated with increased survival and sensitivity to the treatment given [2-5].

*IDH*-mutations have been implicated as an initiating event in gliomagenesis and are key to reprogramming the tumor epigenome and metabolome, largely through neomorphic production and accumulation of 2-Hydroxyglutarate (2HG) [6]. Given uncertainties regarding the effectiveness of options available for treating LGGs, *IDH*-mutations have garnered significant attention as a targetable therapeutic pathway and there are several novel therapies on the horizon [7-9]. Until these therapeutics become available, the clinical mainstay of treatment for patients with LGG consists of surgical resection, with radiation therapy and alkylating chemotherapy being typically reserved for recurrences that were either sub-totally resected or have undergone MT.

MR imaging is an integral component of brain tumor diagnosis and monitoring. Recent advances in state-of-the-art techniques have enabled the non-invasive assessment of tumor morphology and physiology, with primary GBM having been studied most extensively. Although the ability to non-invasively detect MT would be of significant clinic interest for diagnosis and treatment planning, there have been few studies which have focused on addressing this question. Multiparametric MR imaging holds significant promise for comprehensively characterizing the structural and physiological properties of the tumor. We hypothesize that these advanced imaging techniques may also provide improved characterization of MT in patients with recurrent LGG.

The objective of this study was to establish multiparametric MR imaging profiles of patients with tumors prior to image guided surgery in order to relate metrics obtained from these methodologies to histopathological grade. Volumetric regions with abnormal imaging features were calculated to provide a robust assessment of the entire recurrent tumor lesion. Regions of viable tumor were targeted for image-guided tissue sampling, in order to associate *in vivo* parameters with histopathological features and to strengthen our understanding of the link between glioma tumor biology and parameters from non-invasive imaging.

## **Materials and Methods**

### ***Patient accrual***

Institutional Review Board approval was obtained to study patients who had an original pathological diagnosis of a WHO Grade II glioma. Patients were recruited immediately

prior to surgical resection for a suspected recurrence, when MT to a higher grade is often observed.

### ***In vivo multimodal MR imaging and spectroscopy***

MR examinations were performed on either a 1.5 T or 3 T EXCITE GE Signa Echospeed scanner (GE Healthcare Technologies) using an eight-channel phased-array headcoil (MRI Devices). Standard anatomical imaging included T<sub>2</sub>-weighted (FLuid Attenuated Inversion Recovery (FLAIR) and Fast Spin Echo (FSE)) as well as T<sub>1</sub>-weighted pre- and post-gadolinium contrast images. Diffusion Weighted Imaging (DWI) was obtained in the axial plane with 6 gradient directions and two-fold acceleration with sensitivity encoding parallel imaging [repetition time (TR)/echo time (TE) = 1000/108 ms, voxel size = 1.7 × 1.7 × 3 mm<sup>3</sup>, b = 1000 s/mm<sup>2</sup>]. Dynamic Susceptibility Contrast (DSC) Perfusion Weighted Imaging (PWI) was obtained with a 5ml/s bolus injection of 0.1mmol/kg body weight gadolinium diethyltriamine pentaacetic acid (Gd-DTPA) acquired using a series of T<sub>2</sub>\*-weighted echo-planar images [TR/TE/Flip-angle = 1250-1500/35-54 ms/30-35 degrees, 128 × 128 matrix, slice thickness = 3-5mm, 7-15 slices with 60-80 time points] before, during, and after injection. Lactate-edited 3D proton MR spectroscopic imaging (MRSI) was applied using point-resolved spectroscopic selection (PRESS) for volume localization and very selective saturation (VSS) pulses for lipid signal suppression [approximate excited volume = 80 × 80 × 40 mm<sup>3</sup>, TR/TE = 1104/144 ms, overpress factor = 1.5, field of view = 16 × 16 × 16 cm<sup>3</sup>, nominal voxel size = 1 × 1 × 1 cm<sup>3</sup>, flyback echo-planar readout gradient in the SI direction, 988 Hz sweep width and 712 dwell points] [10].

### ***Post processing of MR exam***

The *in vivo* data were de-identified and transferred to a local Linux workstation. Software developed in house was applied to estimate relevant DWI, PWI, and MRSI parameters and normalize between field strengths using estimates from Normal Appearing Brain Tissue (NABT). Maps of the normalized Apparent Diffusion Coefficient (ADC) were generated on a voxel-by-voxel basis according to a published algorithm [11]. Perfusion datasets were non-rigidly aligned using the VTK CISG software package [12].

Normalized Cerebral blood volume (CBV), percent  $\Delta R2^*$  signal recovery (%-REC),  $\Delta R2^*$  peak height (PH), and recirculation factor were calculated for each voxel using software developed by our lab. CBV intensities and PH parameters were obtained by fitting the dynamic perfusion data by a modified gamma-variate function with a recirculation parameter [13]. Peak height and percent recovery values were also estimated using a simplified nonparametric procedure [14].

Lactate-edited MRSI data were reconstructed and the signal from the individual channels combined to quantify total choline (tCho), N-acetyl-aspartate (NAA), creatine (Cr), lactate (Lac) and lipid (Lip) levels. The choline-to-N-acetyl-aspartate index (CNI) and choline-to-creatine index (CCRI) values were generated from a linear regression based algorithm, which represents changes in choline and NAA or Cr levels compared to voxels in NABT. Excess choline (exCho) and excess creatine (exCr) was calculated using the formulas  $(tCho - [tCho/NAA]_{NABT} * NAA) / tCho_{NABT}$  and  $(Cr - [Cr/NAA]_{NABT} * NAA) / Cr_{NABT}$  [15], respectively. Imaging data were aligned to the post-Gadolinium scan using FMRIB's Linear Image Registration Tool (FLIRT). Anatomic imaging was resampled for overlay with DWI, PWI, and MRSI and the SIVIC software package was used to select target locations for intra-operative tissue sampling [16]. An example of the multimodal MR

imaging data is shown in Figure 4.1.

### ***Tissue sample acquisition***

Tissue sample targets were planned for each patient based on surgically accessible regions of abnormally decreased ADC, decreased %-REC and increased PH and CBV, as well as elevated CNI, which are expected to represent viable, cellular regions of tumor with elevated proliferation and neovascularization. These locations were designated as 5-mm-diameter spherical targets on co-registered MR images using the surgical navigation software (BrainLAB Inc.). Intra-operative navigation guided the neurosurgeons to these designated locations and tissue samples were excised if it was possible to do so safely. A research assistant was present in the operating room to obtain 3D screenshots and coordinates of the precise location where the tissue sample was removed. Samples were immediately bisected with half being fixed in 10% zinc formalin, dehydrated by graded ethanols, and embedded in Paraplast Plus wax (McCormick Scientific) using standardized techniques for tissue processing and immunohistochemistry and the other half being snap-frozen in liquid nitrogen and stored at 80°C for <sup>1</sup>H High Resolution Magic Angle Spinning (HR-MAS) spectroscopy. The results of the *ex vivo* metabolic analysis of a subset of these patients have been published by our group in previous manuscripts [17-19].

### ***Histopathology and IDH-analysis***

Tissue samples were reviewed and scored for standard WHO II criteria by a board-certified neuropathologist. Antibodies used in the assessment of the samples included



rabbit polyclonal MIB-1 anti-Ki67 (30-9) (Ventana Medical Systems) at 2  $\mu\text{g}/\text{ml}$  for 23 min at 37°C; mouse anti-SMI-31 (Covance) at 1.5  $\mu\text{g}/\text{ml}$  for 8 min at 37°C; rabbit polyclonal Factor VIII (Dako) at 1.2  $\mu\text{g}/\text{ml}$  for 20 min at 37°C; and mouse monoclonal anti-*IDH1R132H* (DIA H09) (Dianova) at 1:50  $\mu\text{g}$  for 32 min at 37°C [20]. Heat antigen retrieval for MIB-1 was performed for 30 min in citrate buffer at pH 6. *IDH1R132H* and Factor VIII staining was performed in Tris-EDTA buffer at pH 8. Following antigen retrieval, sections were treated with 3% methanol-hydrogen peroxide for 16 min at 22°C. All immunohistochemistry assays were performed on the Ventana Medical Systems Benchmark XT.

Slides stained with H&E, MIB-1, SMI-31, and *IDH1R132H* were scored to assess histological characteristics. For the H&E-stained slides, a tumor score was given on the basis of the contribution of tumor cellularity to total cellularity. A score of 0 denoted neuropil without tumor; 1 indicated an infiltrating tumor margin containing detectable but not abundant—numbers of tumor cells; 2 denoted a more cellular-infiltrated zone; 3 denoted highly cellular tumor with few non-neoplastic cells. Tissue samples with a tumor score of 0 were excluded from analysis. Total cell-density was also determined as an average number of cells per 200x field. For MIB-1-stained slides, a labeling index [(MIB-1-positive nuclei per total tumor cells counted per 200x field) x 100%] was calculated based on the evaluation of at least three fields and >1000 cells. A score was then generated by subdividing the labeling index according to approximate grade ranges for mitotic activity: 1 (<4); 2 (4-10); 3 (10-20); 4(>20). For SMI31- stained slides, a score was assigned to each slide on the basis of the extent of disruption of the normal axonal architecture. A score of 0 denoted no disruption; 1 denoted minimal disruption; 2

denoted mild disruption; 3 denoted severe disruption. For *IDH1*R132H -stained slides, each biopsy was qualitatively scored on the basis of the percentage of tumor cells that stained positive for R132H using a four-tier scale: 0, no immunostaining; 1, >0 and < 25% positive; 2, between 25 and 75% positive; and 3, >75% tumor cells positive.

Microvascular morphology was graded based upon H&E staining and Factor VIII immunohistochemistry as delicate (resembling normal cerebral vessels), simple vascular hyperplasia (circumferential hyperplasia with definitive lumen), or complex microvascular hyperplasia (glomeruloid-type vessels). An overall score for each vascular component (delicate, simple vascular hyperplasia, and complex microvascular hyperplasia) based on Factor VIII was derived from its relative contribution to total vascularity using a four-tier ordinal scale (0, no contribution; 1, minimal; 2, prevalent; 3, extensive) at a magnification of 200x. A sum of Factor VIII score across all vascular components was also calculated as a measure of total extent of vascularization. Digital images were captured using a microscope (Olympus, Model BX41TF) and digital camera (Olympus, Model DP70). Continuous values of cell density were converted into an ordinal scale defined as the following: 0 = 0-100 cells/field, 1 = 100-200 cells/field, 2 = 200-400 cells/field, 3 = 300-400 cells/field.

### ***Analysis of MR parameters***

Normalization factors were defined for each study using the mode of the histogram from the whole brain minus the region of hyperintensity on T<sub>2</sub>-weighted FLAIR images. This was previously shown to be representative of values in NABT. Regions of interest (ROIs) were defined manually for the T<sub>2</sub>-hyperintensity (T2ALL), contrast enhancement (CEL), necrosis (NEC), non-enhancing lesion (NEL). In house software was applied to quantify

normalized intensity values at a patient level within each  $T_2$ -lesion and to evaluate the 10th percentile, median, and 90th percentile values of parameters estimated from DWI, PWI, and MRSI.  $T_1$  difference subtraction images were obtained through registration and subtraction of the  $T_1$  pre-contrast images from the  $T_1$  post-contrast images after normalization to make their intensities consistent.

To assess variations in the spatial extent of the anatomic lesion, the volumes of regions with intensities in the  $T_1$  post-Gadolinium image from the CEL ROI  $> 1.2x$  NABT ( $T1c12$ ) or  $> 1.2x$  NABT in the image obtained after  $T_1$  difference subtraction ( $T1s12$ ) were evaluated. Additionally, we analyzed volumes of regions with abnormal ADC, the normalized ADC  $< 1.5$  or  $< 1.25$  times NABT in the T2ALL ( $ADC15$ ,  $ADC125$ ); the perfusion volumes of normalized CBV  $> 2$  or  $3$  ( $CBV2$ ,  $CBV3$ ), non-parametric PH  $> 2$  or  $3$  ( $PH2$ ,  $PH3$ ); spectroscopy volumes of CNI  $> 2$  or  $3$  within the T2ALL ( $CNI2t$ ,  $CNI3t$ ), and the region with CNI  $> 2$  or  $3$  that overlapped with T2ALL ( $CNI2p$ ,  $CNI3p$ ).

To compare imaging parameters with histological findings, normalized intensity values were calculated at the individual tissue-target locations using 5mm spherical ROIs centered at the locations from where the samples were acquired. A weighted-average model-curve was generated at each image-guided sample location to increase the SNR of the dynamic perfusion data and goodness of fit for the model fitting of the CBV calculation. This was performed by determining the percentage of the tissue sample mask within each perfusion voxel and automatically excluding unquantifiable voxels of noise, before taking a weighted average of the remaining curves based on percent overlap with the mask [21].

### ***Heatmap generation***

Histopathology data were categorized by histology and grade, imported into Gitoos version 2.2.1 ([www.gitools.org](http://www.gitools.org)) [22] and a linear, hierarchical clustering algorithm was performed within grade as well as within grade and histologic subtype. Heatmaps of abnormal imaging volumes were generated based on the difference from the median values within each parameter and normalized by the 90<sup>th</sup>-percentile for relative visualization. The data then were categorized by grade, imported into Gitoos and a linear, hierarchical clustering algorithm was performed at the patient level, and a header column of the mean parameter values was generated.

### ***Statistical analysis***

A Wilcoxon rank sum test was used to assess the statistical significance of imaging parameters between lesions that had remained Grade II and those that had undergone MT. Kaplan Meier curves were generated using Stata version 11 [23]. If the curves did not cross, the association of parameter and outcome was assessed via the log-rank test, otherwise the Tarone-Ware test was employed. Statistical significance was assessed at  $p < 0.05$ .

In order to identify variables that could play a role in predicting MT, we built logistic regression models implementing a forward/backward selection process using the minimum Akaike Information Criterion (AIC) in JMP Pro 11.0. Between anatomic, diffusion, perfusion, and spectroscopic modalities there were a total of 80 variables included in this selection process and included both volumetric and intensity measurements. This selection process indicated around a dozen variables for a logistic

model, which decreased the smallest outcome group to between 40-50 patients due to missingness in the variables.. To maximize the number of patients included we constrained the final predictive models to at most four variables. We chose models for which (1) variables came from multiple different imaging modalities, and (2) prediction error rate estimations via Leave-one-out cross-validation on our patient data set were minimized. A custom R script (version 3.1.2) [24] was used to iterate over the different variable combinations to determine several models that satisfied these criteria. The model presented in the results had the lowest overall error rate of those generated.

The Kendall tau rank correlation test was used to assess pair-wise correlations between tissue sample level histopathology and imaging parameters. The Holmes Step-Down algorithm was used to determine a conservative  $p$  value cutoff of  $p < 0.00008$  to account for multiple testing in our correlation analysis. Network analysis and visualization was performed using Cytoscape version 3.2.0 ([www.cytoscape.org](http://www.cytoscape.org)) [25]. Due to the exploratory nature of this type of network analysis, a cutoff value of  $p < 0.05$  was applied.

## **Results**

### ***Characterization of patient population with recurrent LGG***

A total of 120 patients with recurrent LGG were recruited to the study. Nine patients were excluded due to diagnosis inconsistent with LGG, leaving 111 patients for analysis. Ten patients received scans at two distinct recurrence timepoints, giving a total of 121 scans for analysis. The population included 54 females and 57 males, with a median age of 36

(range 15-70) at their original diagnosis and 43 (range 18-70) at the current surgery. The median time to the surgery being considered was 2244 days (6.1 years), and for the patients who had records available 26% had received prior radiation therapy, 43% had been treated with TMZ and 25% with other experimental agents. For the majority of cases there had been one or more prior recurrences, but the surgery considered was the first since their original diagnosis. It was observed that 59% of scans were of patients that had undergone MT to a higher grade lesion: 50 patients (41%, 92 tissue samples) remained Grade II, while 55 patients (46%, 107 tissue samples) had upgraded to anaplastic glioma (Grade II→III) and 16 patients (13%, 37 tissue samples) to secondary GBM (Grade II→IV). There were 55 subjects with astrocytoma (AS), 45 with oligodendroglioma (OD), and 21 with mixed oligoastrocytoma (OA) histologic subtypes (see Table 1). *IDH*-mutation status was assessed in 100 patients with sufficient size tissue, with 19 patients (19%) having lesions that were *IDH*-wild-type and 81 patients (81%) having lesions that were mutated. Deletion status for 1p-19q had been evaluated for 61 patients, of whom 33 (54%) were co-deleted and 28 (46%) were not. A total of 52 patients had p53 mutation status assessed, among whom 37 (71%) were mutated.

For patients who had clinical follow-up available (109/113), the median progression free survival (PFS) from the time of the current surgery was 27 months (95% confidence interval 21 to 32 months), with the time for subjects who remained Grade II being 28 months (95% confidence interval 21 to 40 months), for subjects in the Grade II→III cohort being 31 months (95% confidence interval 19 to 46 months), and for subjects in the Grade II→IV cohort being 13 months (95% confidence interval 3 to 19 months). PFS and overall survival (OS) curves are presented in Figure 4.2. Although there was insufficient follow-up to assess the median OS for the cohort that remained Grade II, the

median OS for the Grade II→III cohort was estimated to be 52 months (95% confidence interval 38 months up with 25 subjects dead and 26 subjects censored) and for the Grade II→IV cohort was 22 months (with 95% confidence interval 12 to 26 months and all 18 subjects having died).

	Grade	Total patient scans (samples)	Astrocytoma (samples)	Oligodendroglioma (samples)	Oligoastrocytoma (samples)
Acquired	All	130 (251)	—	—	—
Excluded	All	9 (15)	—	—	—
Analyzed	All	121 (236)	55 (105)	45 (85)	21 (46)
	II	50 (92)	9 (16)	29 (52)	12 (24)
	II→III	55 (107)	30 (52)	16 (33)	9 (22)
	II→IV	16 (37)	16 (37)	—	—

**Table 4.1 Recurrent LGG pre-surgical scans organized by grade and histopathological subtype.** The population comprised astrocytoma, oligodendroglioma, and mixed oligoastrocytoma histological subtypes. Nine patients and 15 tissue samples were excluded due to them having diagnoses other than LGG. 10 of the 121 patient scans were scanned at two distinct recurrences.

### ***Findings from the pre-surgery anatomic MR images***

The right hand rows in the heatmap shown in Figure 4.2C give a visual interpretation of the volumetric imaging data from individual subjects and Figure 4.3 shows summary parameters separated by grade and histological sub-type. Recurrent lesions with larger T<sub>2</sub>-lesions were associated with a higher probability of MT (see Supplementary Table 1). The median volumes of the T<sub>2</sub>-lesion for the 47 subjects who remained Grade II was 15.6 cc, for the 47 subjects in the Grade II→III cohort was 30.9 cc and for the 18 subjects in the Grade II→IV cohort was 69.7 cc. Only eight of the lesions had visually identifiable regions of necrosis, of which corresponded to 4 lesions with a diagnosis of

Grade III oligodendroglioma and 4 lesions with a diagnosis of GBM.

Of the cohort that remained Grade II, only 13/47 (28%) were characterized as having small regions of enhancement on post-contrast T<sub>1</sub>-weighted images, while 23/47 (49%) for the Grade II→III cohort were enhancing and all of the lesions for the Grade II→IV cohort were enhancing. Visual assessment of the volume of contrast enhancement, as well as analysis of intensities in the post-contrast T<sub>1</sub>-weighted image and in T<sub>1</sub>-subtraction images indicated that these regions were relatively small compared with the T<sub>2</sub>-lesion, but were larger for cases that had undergone MT. Oligodendrogliomas tended to have modest T<sub>2</sub>-lesion volumes but were more likely to have regions of contrast enhancement (69% of the Grade II→III oligodendrogliomas compared with 37% of the Grade II→III astrocytomas, see Figure 4.3A and B). Univariate statistical analysis indicated that several parameters derived from the histograms of intensities within the T<sub>2</sub>-lesion were also significantly different between lesions that remained Grade II compared with those that had undergone MT. These included the median and 90<sup>th</sup>-percentile values from T<sub>1</sub>-subtraction and T<sub>1</sub>-post contrast images as presented in Supplementary Table 4.1.



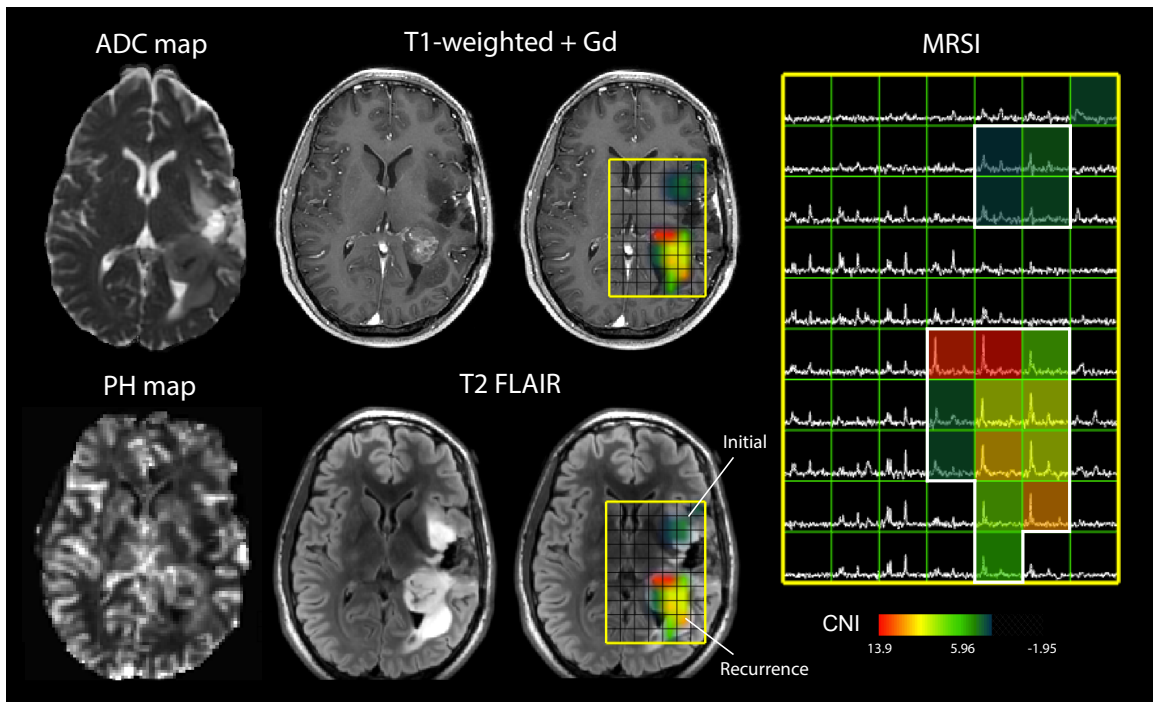


**Figure 4.1 Multimodality MR imaging exam of a subject with a recurrent LGG that had undergone MT.** Neurosurgical tissue targets were planned based on regions of suspected tumor using additional functional MR techniques. The imaging revealed a heterogeneously enhancing region of recurrent tumor situated in the left posterior temporal and parietal white matter. An additional, mass-like non-contrast enhancing region of residual tumor was also seen in the left insular white matter. This lesion was consistent with residual low-grade neoplasm with marked differences in ADC, PH, and CNI (abnormal regions highlighted in white.)

#### ***Findings from the pre-surgery diffusion weighted MR images***

Analysis of diffusion parameters within the T<sub>2</sub>-lesion indicated that the 10<sup>th</sup>-percentile of the ADC and radial diffusion ( $\lambda$ -rad) were significantly lower for lesions that had undergone MT. While this trend held for all three histological sub-types, it was noted that lesions with oligodendroglioma sub-type had lower median ADC values than astrocytomas. As can be seen in Supplementary Table 4.1 the larger overall T<sub>2</sub>-lesion volumes and lower ADC values associated with MT translated to the diffusion volume metrics (ADC<sub>15</sub>, ADC<sub>125</sub>) for these lesions being significantly larger relative to lesions

that had remained Grade II. When separated based upon histological sub-type, it was noted that astrocytomas transforming to Grade III had median ADC15 volumes that were similar to those remaining Grade II (see Figure 4.2C). The heatmap in Figure 4.2 also revealed a subset of the lesions that remained Grade II with similar diffusion volumes as their higher grade counterparts.

***Findings from the pre-surgery perfusion weighted MR images***

As shown in Supplementary Table 4.1, the 90<sup>th</sup>-percentile CBV values and 75<sup>th</sup>-percentile non-parametric PH values were significantly higher for lesions that had undergone MT. When considering the volumes of regions with elevated CBV and PH within the T<sub>2</sub>-lesion, it was clear that lesions transforming to GBM and to Grade III oligodendroglioma also had larger abnormal perfusion volumes (CBV2, CBV3, PH2 and PH3) as shown in Figure 4.2D. Interestingly, as can be seen in the heatmap, the same group of patients who had remained Grade II and had larger diffusion volumes also had larger abnormal perfusion volumes.

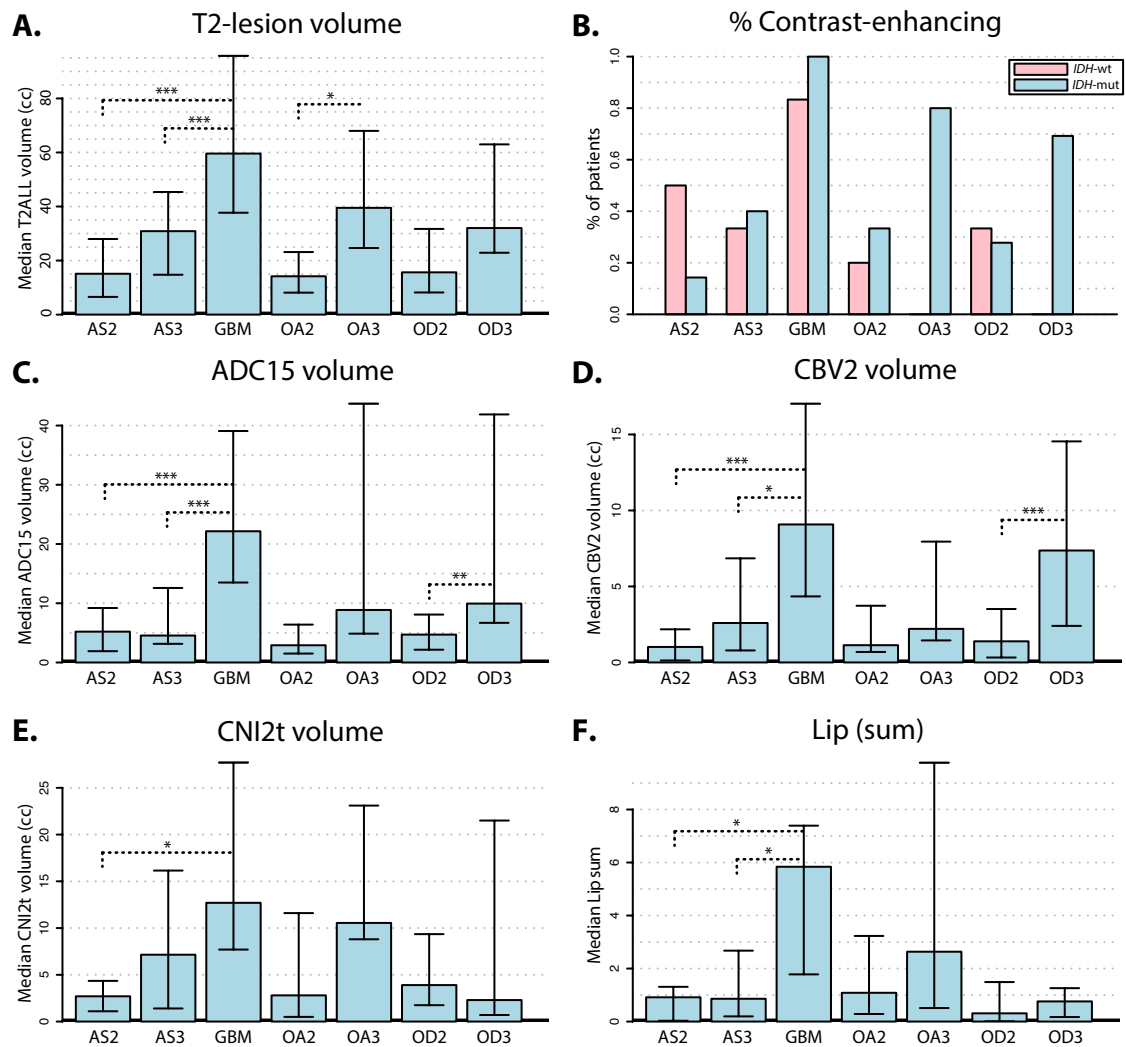


**Figure 4.2 Differences in lesions that had undergone malignant transformation.** The bar plots represent median differences of volumetric imaging parameter values between the various histological grades and subtypes. Error bars are representative of the 25<sup>th</sup>- and 75<sup>th</sup>- percentile. Statistical significance was assessed using a Wilcoxon rank sum test at  $p < 0.05$  (\*),  $p < 0.01$  (\*\*), and  $p < 0.005$  (\*\*\*)

### **Findings from pre-surgery spectroscopic imaging data**

Although there were less patients for whom pre-surgery spectroscopic imaging data were acquired (83/113) there were a number of metabolic intensity parameters significantly different for lesions that had undergone MT. These included the median,

90<sup>th</sup>-percentile, and maximum values of excess choline, 90<sup>th</sup>-percentile and maximum values of CCRI, maximum values of CNI, and tCho levels, and the minimum and 10<sup>th</sup>-percentile values of creatine (see Supplementary Table 4.1). The assessment of volumes of abnormal metabolism (CNI2t, CNI2p, CNI3t, and CNI3p) were all significantly larger for cases that had undergone MT. As was the case with abnormal perfusion volumes, the same group of subjects who had larger abnormal diffusion volume also had larger metabolic lesions (see Figure 4.3). When evaluated by histological sub-type, oligodendrogliomas tended to have lower CNI, Lac and Lip than astrocytomas and oligoastrocytomas. The subjects with lesions that had transformed to GBM had the highest integrated CNI, Lac and Lip values in the CNI2t region (see Figure 4.2F).

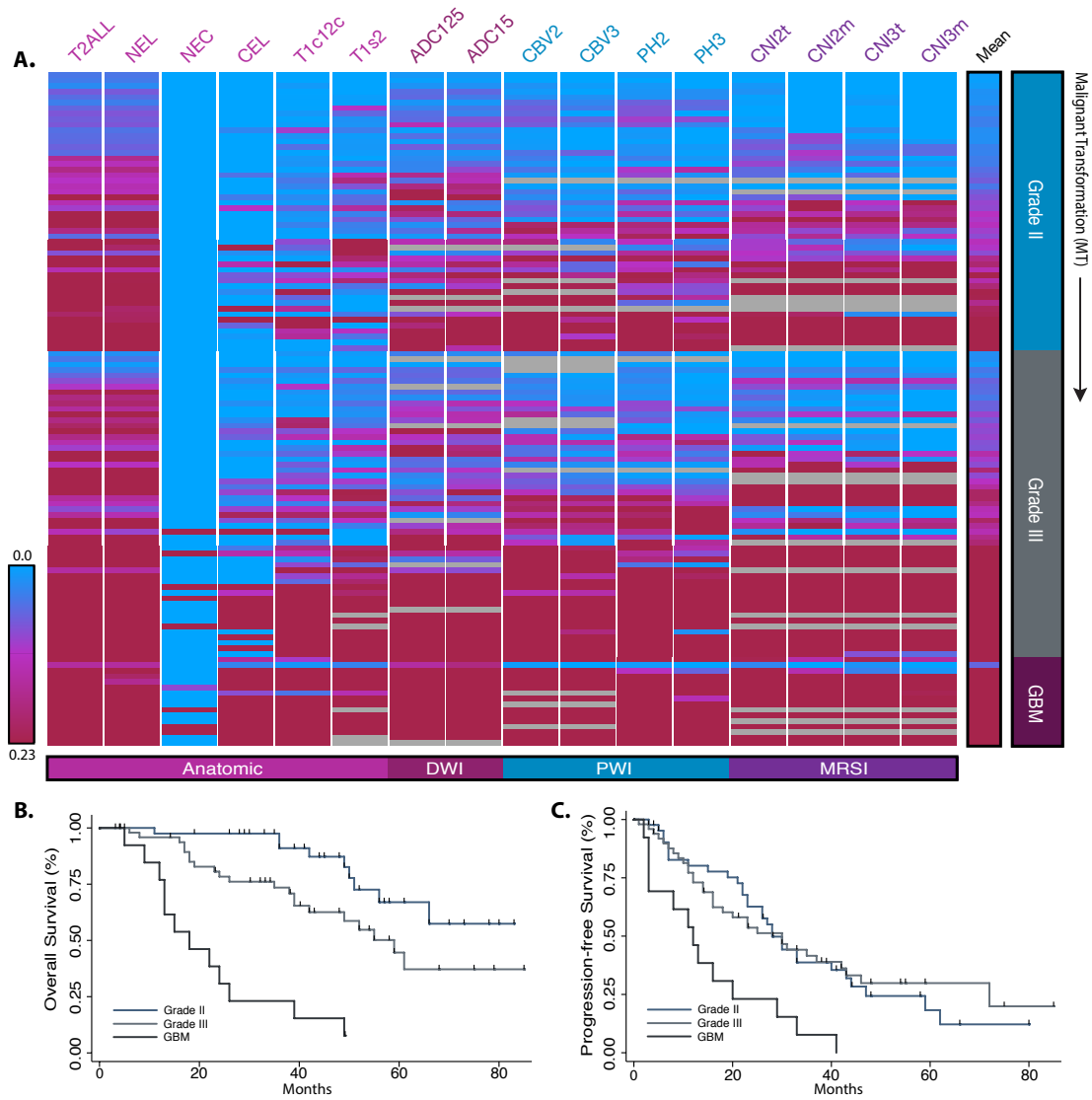


**Figure 4.3 Heatmaps of volumetric MR parameters and clinical outcome of recurrent LGG.** Kaplan Meier curves generated from overall survival (A) and progression-free survival (B) demonstrated statistically significant differences between WHO Grades for OS between Grade II and Grade II→III ( $p = 0.006$ ), Grades II/II→III and GBM ( $p < 0.001$ ), while PFS only distinguished GBM from Grade II and Grade II→III lesions ( $p < 0.001$ ). (C) The heatmap was generated using patient scans that were organized by row and the data were normalized within each imaging parameter (by column). Data were hierarchically clustered within each tumor grade, revealing subgroups of Grade II and Grade III lesions that displayed similar abnormal imaging features similar to GBM. Zero volume is shown in blue and approximately twice the median normalized volume is shown in red. Grey cells denote cases when there were no data available.

### ***Multivariate analysis of imaging parameters***

In an effort to provide predictive modeling that utilized the strongest statistical differentiators of MT, we developed several multivariate logistical regression models utilizing parameters that spanned multiple MR modalities and both volumetric and intensity parameters measurements. The model with the highest overall accuracy included estimates of the 10<sup>th</sup>-percentile of creatine in regions with CN1 greater than 2; the volume of ADC greater than 1.5x that of NABT divided by the T2ALL volume; the median ADC in the T2ALL region; as well as the 10<sup>th</sup>-percentile FSE in the T2ALL. This model had a similar performance to several others, with a predictive accuracy of 76.04%, with a 10.42% false-negative and 13.54% false-positive rate (see Supplementary Figure 1). Lesions that were misclassified corresponded to 17% of the astrocytomas, 20% of the oligogastrocytomas and 35% of the oligodendrogliomas, suggesting that it may be possible to generate better models by considering the histological sub-types separately.

### ***Differences in histopathological parameters with grade and sub-type***

To examine the histopathological features associated with recurrent LGG, we produced a heatmap based on the neuropathology assessment of each of the image guided tissue samples (see Figure 4.4). As expected, tissue samples that had undergone MT were characterized by increased measures of relative tumor content (T-score), proliferation (MIB-1), and axonal disruption (SMI-31). Interestingly, several image-guided tissue samples from WHO Grade II oligodendrogliomas contained very elevated MIB-1 scores between 10-20%, two of which were greater than 20%. Thus, image-guided sampling identified tumor regions with MT that clinical sampling did not. Anaplastic glioma and

secondary GBM samples were characterized by increased hypoxic conditions (CA-9), the presence of neovascularization and necrosis, the latter of which was found primarily in GBM samples.

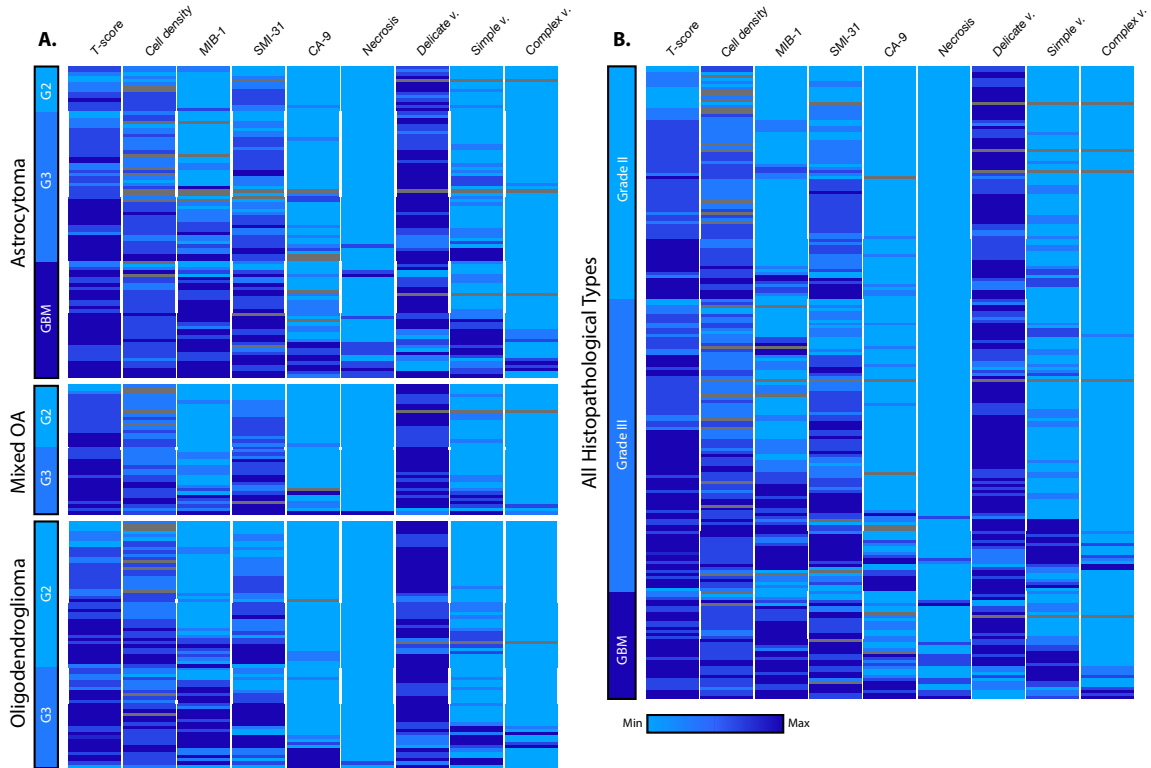


**Figure 4.4 Heatmap of image-guided tissue samples.** (A) To assess the biological features of within each distinct histology, the neuropathology data were separated by glioma subtype and used hierarchical clustering within each grade. Based on image-guided targeting criteria, several Grade II samples were identified that had an unusually high MIB-1 score, and two Grade III astrocytomas or mixed oligoastrocytomas that had necrosis present. Although few in number, these examples highlight the utility of image-guidance to improve tumor sampling. A portion of Grade III oligodendroglioma patients had elevated CA-9 scores of hypoxia. When evaluating the entire mixed population of glioma histologies (B), we observed a decrease in normal, delicate vasculature (delicate v.) and an increase in the presence of simple and complex neovascularization (simple & complex v.) were noted within a subset of tumors that had undergone malignant transformation.

### ***Correlation of histopathology and in vivo imaging parameters***

Analysis of imaging intensities that were calculated at the spatial location of the tissue sample excision with histopathology scores provided insight to the biological underpinnings of specific MR based imaging measurements (see Supplementary Table 4.2). ADC values from the DWI were inversely correlated with cell proliferation. Non-linear CBV and non-parametric PH were correlated with cell density, mitotic figures, and hypoxia. T<sub>1</sub>-imaging metrics (T1c, T1s) were also correlated with mitotic figures and simple vascular hyperplasia, while T<sub>1</sub>-contrast enhancement was correlated with necrosis.

Visual network maps that were generated based on Kendall's-tau correlations are presented in Figure 5. We observed high levels of connectivity and decreased average edge length within diffusion ( $\lambda$ -rad, ADC), perfusion (PH, CBV, %-rec), and anatomic T<sub>1</sub>-imaging metrics (T1c, T1s), as well as MRSI measures of excess choline-to-creatine indices (exCCRI) in the complete multi-modal imaging and histopathology network (Fig. 4.5A). Due to increased centrality and connectivity in these parameters, it is possible that these metrics may provide an increasingly objective assessment of tumor histopathology.

To better assess the specific nature of the various imaging modalities, we generated modality specific networks (Fig. 4.5B-E). The anatomic imaging metrics were highly central and shared edges with several pathological measures of tumor, however the T<sub>1</sub>-imaging correlated more specifically with necrosis and vascularization and the FSE with hypoxia. The diffusion network consisted of two major clusters, with the larger containing



both ADC and  $\lambda$ -rad, and being associated with several measures of proliferative tumor. The presence of normal, delicate vasculature was correlated with ADC values, while necrosis shared a node with  $\lambda$ -rad and the second, smaller cluster around FA, T-score, and SMI-31. In the perfusion network, non-linear CBV held common edges with all histopathology parameters, while PH and %-REC were each correlated with several distinct nodes. In the metabolic imaging correlation network, measures of CCRI and exCCRI had the highest levels of connectivity with histopathology, and increased dispersion and specificity being observed among the other metabolites.

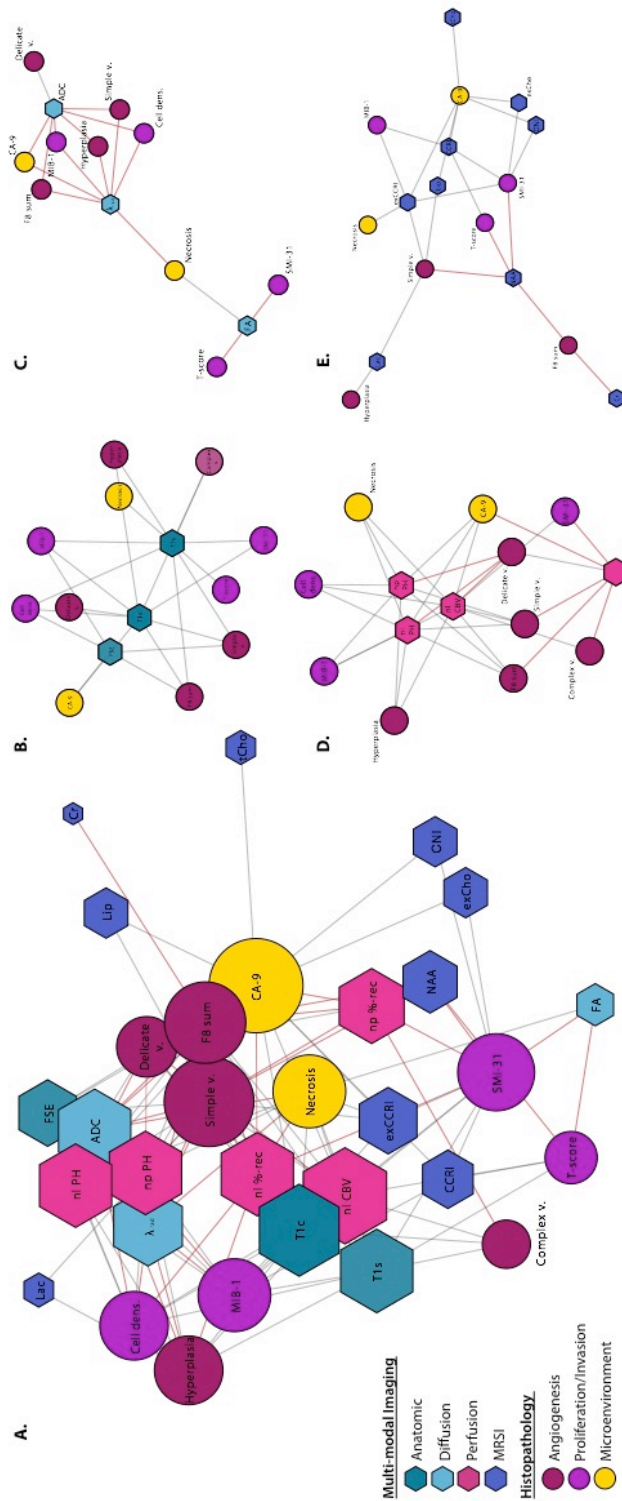


**Figure 4.5 Network linkage map of histopathology and advanced imaging of image guided tissue samples.** Nodes were colored coded using meta-labels of angiogenesis, proliferation & invasion, and microenvironment for histopathology parameters as well as by modality for imaging parameters. Node size corresponds with average shortest path length. Imaging nodes are presented as hexagons and histopathology nodes as circles. Although imaging and histopathology parameters were intra-correlated, only edges between histopathology and imaging were generated for clarity of network visualization. Red connections denote negative correlation. We noted increased connectivity between DWI, anatomic T<sub>1</sub>-imaging metrics, perfusion MIB-1 and CBV, as well as MRSI measures of exCCRI.

## **Discussion**

This study demonstrated the feasibility of utilizing multiparametric MR imaging to identify patients with recurrent LGG whose lesions have undergone malignant transformation. Quantitative analysis of anatomic, diffusion, perfusion and metabolic images provided parameters that described lesion volumes and the magnitude of abnormal intensities relative to normal appearing brain within the same individual. A bioinformatics approach was applied for data visualization, with heatmaps and networks proving helpful in summarizing and interpreting variations in the relatively large number of parameters and complex information contained within the data. The tools that were developed and the metrics that they produce may be helpful in allowing clinicians to make more informed treatment decisions and will aid in evaluating temporal changes within the lesion during routine patient follow-up, or when surgical resection is not feasible.

When considering all patients as a single group, we found many multivariate models with similar predictive accuracy for predicting Grade II versus transformation from Grade II→III or Grade II→IV. The model with the lowest error rate assessed by cross validation had an accuracy of 76%. Given that there were differences in imaging and histological parameters between different sub-types and that transformation to Grade IV had the biggest impact upon survival, a second cohort of patients are now being accumulated to allow further tests of these models and exploratory analyses that include partitioning patients into more specific sub-groups.

The imaging heterogeneity found within this patient population illustrates the challenges that exist for clinicians in interpreting imaging findings from a suspected to be

recurrence, where the results obtained are reflective of both inherent and therapy-driven features of the tumor [26]. Based on the heterogeneity of the histological findings for the image-guided tissue samples, it is clear that surrogate non-invasive markers of proliferation, angiogenesis and invasion are likely to be important for making decisions about both upgrade status the effectiveness of different treatments. The correlations between imaging and histological parameters observed in our study provide strong evidence that integrating metrics derived from multiparametric imaging can be helpful for assessing spatial heterogeneity within the lesion. Of particular interest is the ability to use maps of CBV, ADC and CNI from the pre-surgery imaging examination to target tissue sampling to regions that are likely to be the most malignant. The criteria that was used in our study was to select regions where  $CBV > 2$ ,  $ADC < 1.5$  and  $CNI > 3$ . While it was not always possible to obtain tissue from these exact locations the relatively high yield with positive tumor scores (201/212) indicates that this was a successful strategy. Our previous work in patients with high grade gliomas showed that several of the imaging metrics used in the current study were associated with PFS and OS [15]. It is too early to say whether the subset of lesions that remained Grade II but had similar imaging characteristics as those that upgraded had worse OS. Although the current definition of tumor grade based upon WHO II criteria has been driving decisions about when to use more aggressive therapy, recent studies have suggested that molecular markers such as *IDH* and *TERT* mutations provide a better assessment of prognosis [27, 28]. Because the majority (79%) of the patients in our study were *IDH*-mutated, it was not possible to determine whether *IDH*-status was an important factor in driving outcome. Future studies will be designed to include a full analysis of genomic and epigenetic markers that have been shown to be relevant to the natural history and response to treatment for LGG. This will shed light on the nature of the clonal outgrowths

present in recurrent lesions and how they influence imaging. The long term goal of this and future studies is to improve our understanding of the evolution of malignant glioma and the clinical management of such patients.

### **Funding sources**

This work was supported as a project in the NCI Brain Tumor SPORE grant, number P50CA097257.

### **Acknowledgements**

We would like to acknowledge support from the Brain Tumor Research Center at UCSF in collecting and analyzing the tissue samples, as well as from staff in the Margaret Hart Surbeck Laboratory for Advanced Imaging. We would particularly like to express our gratitude to J. Kurhanewicz, S. Ronen, D. Vigneron, J. Costello, J. Crane, and N. Strauli, for their technical assistance and guidance during this project.

### **References**

- [1] Riemenschneider MJ, Reifenberger G. Molecular neuropathology of low-grade gliomas and its clinical impact. *Adv Tech Stand Neurosurg.* 2010; 35:35–64.
- [2] Grier JT, Batchelor T. Low-grade gliomas in adults. *Oncologist.* 2006; 11:681–693.
- [3] Yan H, Parsons DW, Jin G, McLendon R, Rasheed BA, Yuan W, et al. IDH1 and IDH2 mutations in gliomas. *N Engl J Med.* 2009; 360: 765–73.

- [4] Houillier C, Wang X, Kaloshi G, Mokhtari K, Guillevin R, Laffaire J, et al. IDH1 or IDH2 mutations predict longer survival and response to temozolomide in low-grade gliomas. *Neurology*. 2010; 75:1560–66.
- [5] Li S, Chou AP, Chen W, Chen R, Deng Y, Phillips HS, et al. Overexpression of isocitrate dehydrogenase mutant proteins renders glioma cells more sensitive to radiation  
*Neuro Oncol*. 2013; 15(1):57-68.
- [6] Dang L, White DW, Gross S, Bennett BD, Bittinger MA, Driggers EM, et al. Cancer-associated IDH1 mutations produce 2-hydroxyglutarate. *Nature*. 2009; 462:739–744.
- [7] Kernytsky A, Wang F, Hansen E, Schalm S, Straley K, Gliser C, et al. IDH2 mutation-induced histone and DNA hypermethylation is progressively reversed by small-molecule inhibition. *Blood*. 2015; 125(2):296-303.
- [8] Turcan S, Fabius AW, Borodovsky A, Pedraza A, Brennan C, Huse J, et al. Efficient induction of differentiation and growth inhibition in IDH1 mutant glioma cells by the DNMT Inhibitor Decitabine. *Oncotarget*. 2013; 4(10):1729-36.
- [9] Yen KE, Bittinger MA, Su SM, Fantin VR. Cancer-associated IDH mutations: biomarker and therapeutic opportunities. *Oncogene*. 2010; 29(49):6409-17.
- [10] Park I, Chen AP, Zierhut ML, Ozturk-Isik E, Vigneron DB, Nelson SJ. Implementation of 3T lactate-edited 3D 1H MR spectroscopic imaging with flyback echo-planar readout for gliomas patients. *Ann Biomed Eng*. 2011; 39:193–204.
- [11] Basser PJ, Pierpaoli C. Microstructural and physiological features of tissues elucidated by quantitative-diffusion-tensor MRI. *J Magn Reson*. 1996; 111:209–19.
- [12] Hartkens T, Rueckert D, Schnabel JA, Hawkes DJ, Hill DLG. VTK CISG Registration Toolkit: An open source software package for affine and non-rigid registration of single- and multimodal 3D images. BVM Leipzig, Germany, Springer-Verlag 2002; 185.

- [13] Lee MC, Cha S, Chang SM, Nelson SJ. Dynamic susceptibility contrast perfusion imaging of radiation effects in normal-appearing brain tissue: changes in the first-pass and recirculation phases. *J Magn Reson Imaging*. 2005; 21:683–93.
- [14] Lupo JM, Cha S, Chang SM, Nelson SJ. Dynamic susceptibility weighted perfusion imaging of high-grade gliomas: characterization of spatial heterogeneity. *Am J Neuroradiol*. 2005; 26:1446–54.
- [15] Li Y, Lupo JM, Parvataneni R, Lamborn KR, Cha S, Chang SM, et al. Survival analysis in patients with newly diagnosed glioblastoma using pre- and postradiotherapy MR spectroscopic imaging. *J Neurooncol*. 2013; 15(5):607-617.
- [16] Crane JC, Olson MP, Nelson SJ (2013) SIVIC: Open-Source, Standards-Based Software for DICOM MR Spectroscopy Workflows. *Int J Biomed Imaging*. 2013: 169526–12. doi:10.1155/2013/169526.
- [17] Elkhaled A, Jalbert LE, Phillips JJ, Yoshihara HAI, Parvataneni R, Srinivasan R, et al. Magnetic resonance of 2- hydroxyglutarate in IDH1-mutated low-grade gliomas. *Sci Transl Med*. 2012; 4, 116ra5.
- [18] Elkhaled A, Jalbert L, Constantin A, Yoshihara HA, Phillips JJ, Molinaro AM, et al. Characterization of metabolites in infiltrating gliomas using ex vivo <sup>1</sup>H high-resolution magic angle spinning spectroscopy. *NMR Biomed*. 2014 May;27:578-93.
- [19] Constantin A, Elkhaled A, Jalbert L, Srinivasan R, Cha S, Chang SM, et al. Identifying malignant transformations in recurrent low grade gliomas using high resolution magic angle spinning spectroscopy. *Artif Intell Med*. 2012; 55:61-70.
- [20] Capper D, Zentgraf H, Balss J, Hartmann C, Von Deimling A. Monoclonal antibody specific for IDH1 R132H mutation. *Acta Neuropathol*. 2009; 118: 599–601.
- [21] Lupo JM, Wen Q, Phillips JJ, Chang SM, Nelson SJ. Weighted-average model curve preprocessing strategy for quantification of DSC perfusion imaging metrics from image-

guided tissue samples in patients with brain tumors. *Proc Intl Soc Mag Reson Med.* 2015; 4392.

[22] Perez-Llamas C, Lopez-Bigas N. Gitools: Analysis and Visualisation of Genomic Data Using Interactive Heat-Maps. *PLoS ONE.* 2011; 6.

[23] StataCorp. 2009. *Stata Statistical Software: Release 11.* College Station, TX: StataCorp LP.

[24] R Core Team. R: A language and environment for statistical computing. R Foundation for Statistical Computing. 2013 ISBN 3-900051-07-0

[25] Shannon P, Markiel A, Ozier O, Baliga NS, Wang JT, Ramage D, et al. Cytoscape: a software environment for integrated models of biomolecular interaction networks. *Genome Research.* 2003; 11:2498-504.

[26] Johnson BE, Mazar T, Hong C, Barnes M, Aihara K, McLean CY, et al. Mutational Analysis Reveals the Origin and Therapy-driven Evolution of Recurrent Glioma. *Science.* 2014; 343:189-93.

[27] Eckel-Passow JE, Lachance DH, Molinaro AM, Walsh KM, Decker PA, Sicotte H, et al. Glioma Groups Based on 1p/19q, *IDH*, and *TERT* Promotor Mutations in Tumors. *N Engl J Med.* 2015; 372:2499-508

[28] The Cancer Genome Atlas Research Network. Comprehensive, Integrative Genomic Analysis of Diffuse Lower-Grade Gliomas. *N Engl J Med.* 2015; 372:2481-98

### **Supplementary Figure and Table Legends**

**Supplementary Figure 4.S1 Multivariate logistical regression model of malignant transformation.** The component parameters of the model included volumetric and intensity measurements selected through an AIC forwards-backwards selection process and had a predictive accuracy of 76.04% in predicting MT versus non-MT lesions, with a



10.42% false-negative and 13.54% false-positive rate.

**Supplementary Table 4.S1 MR intensity and volumetric parameters for malignant transformation and *IDH*-mutation in recurrent LGG.** Parameters were evaluated by Wilcoxon rank-sum test ( $p < 0.05$ ).

**Supplementary Table 4.S2 Correlations of *in vivo* imaging of tissue sample targets.** A Kendell tau rank test was performed with a stringent  $p$  value cutoff of  $p < 0.00008$  as determined using a Holmes Step-Down algorithm. Imaging correlates and anticorrelates with histopathology scores are presented.

**Supplementary Figure and Tables**

**Supplementary Figure 4.S1 Multivariate logistical regression model of malignant transformation.**

		Predicted G2	Predicted MT	
Actual G2	25	13		<u>Model components:</u> - Cr (10%) in CNI>2 - Volume ADC > 1.5 NABT / volume of T2ALL - ADC (med) in T2ALL - FSE (10%) in T2ALL
Actual MT	10	48		

**76% Accuracy**

**Supplementary Table 4.S1 MR intensity and volumetric parameters for malignant transformation and *IDH*-mutation in recurrent LGG were evaluated by Wilcoxon rank-sum test ( $p < 0.05$ ).**

	<b>Malignant Transformation</b>			
	<i>volumetric</i>		<i>intensity</i>	
	<i>parameter</i>	<i>p value</i>	<i>parameter</i>	<i>p value</i>
<b>Anatomic</b>	T2ALL	$p < 0.001$	T1c (90%)	$p < 0.001$
	CEL	$p < 0.001$	T1c (med)	$p = 0.002$
	NEL	$p < 0.001$	T1s (med)	$p = 0.015$
	NEC	$p = 0.008$	T1s (90%)	$p = 0.006$
	T1c12c	$p < 0.001$		
	T1s1	$p < 0.001$		
<b>DWI</b>	ADC125	$p < 0.001$	ADC (10%)	$p = 0.014$
	ADC15	$p < 0.001$	$\lambda$ -rad (10%)	$p = 0.046$
<b>PWI</b>	CBV2	$p < 0.001$	nl CBV (90%)	$p = 0.007$
	CBV3	$p < 0.001$	np PH (75%)	$p = 0.017$
	PH2	$p < 0.001$		
	PH3	$p = 0.004$		
<b>MRSI</b>	CNI2t	$p = 0.004$	exCho (med)	$p = 0.023$
	CNI2m	$p = 0.006$	exCho (90%)	$p = 0.031$
	CNI3t	$p = 0.004$	exCho (max)	$p = 0.003$
	CNI3m	$p = 0.005$	CCRI (90%)	$p = 0.038$
			CCRI (max)	$p = 0.002$
			CNI (max)	$p = 0.003$
			tCho (max)	$p = 0.004$
			Cr (min)	$p = 0.012$
			Cr (10%)	$p = 0.018$

**Supplementary Table 4.S2 Correlations of *in vivo* imaging of tissue samples targets.**

<b>Histopathology Parameter</b>	<b>Imaging Correlates</b>	<b>Imaging Anticorrelates</b>
Cells / field	np PH, nl CBV	—
MIB-1	T1c, T1s, nl CBV, np PH	ADC
Simple vasculature	T1c, T1s	—
Factor 8 sum	T1s	—
CA9	nl CBV, np PH	nl %-rec
Necrosis	T1c	—

## CHAPTER 5: Metabolic Profiling of Malignant Transformation and *IDH*-mutation in Diffuse Infiltrating Gliomas

---

In this project, *ex vivo* high-resolution magic angle spinning spectroscopy (HR-MAS) was utilized to obtain the metabolic profiles of patients with infiltrating glioma, in order to characterize the metabolic differences associated with malignant transformation and *IDH*-mutation. Distinct metabolic differences in patients that had undergone MT were observed, as well as in those patients with an *IDH*-mutated genotype. These findings may improve the understanding of the physiological differences present in these lesions, as well as aid in designing non-invasive *in vivo* sequences for improved diagnosis and monitoring.

---

Authors:

Llewellyn E. Jalbert, Adam Elkhaled, Joanna J. Phillips, Evan Neill, Marram P. Olson, Mitchel S. Berger, Sabrina Ronen, John Kurhanewicz, Susan M. Chang, and Sarah J. Nelson

## **Abstract**

Infiltrating low grade gliomas are heterogeneous in nature and highly complex in their clinical management. Aggressive treatments are typically reserved for patients that have undergone malignant transformation (MT) to a high-grade anaplastic glioma or secondary glioblastoma multiforme (GBM). Patients with mutations in the *isocitrate dehydrogenase 1 and 2 (IDH1/2)* oncogenes have been associated with favorable outcome and treatment sensitivity. In this study, the *ex vivo* metabolic profiles of image-guided tissue samples from patients with low grade gliomas were investigated using high-resolution magic angle spinning (HR-MAS). Distinct spectral profiles were observed for lesions that had undergone MT, as well as for tumors that had *IDH*-mutated genotypes. Levels of 2-hydroxyglutarate (2HG) levels were correlated with mitotic activity, as well as several brain tumor metabolites. The information obtained may be used to develop strategies for *in vivo* characterization of infiltrative glioma in order to improve diagnosis and assist in monitoring response to therapy.

## **Introduction**

Diffuse infiltrating gliomas comprise 80% of malignant brain tumors and consist primarily of astrocytes and oligodendrocytes. Tumor grade is assessed according to criteria set by the World Health Organization (WHO) [1]. Patients who are diagnosed with Grade II glioma are considered to be low grade (LGG), and can survive for years or even decades [2,3]. In making decisions about clinical management, it is necessary to strike a balance between treating the tumor and impacting quality of life. More aggressive treatments are often reserved for tumor recurrence, when lesions may undergo

malignant transformation (MT) to Grade III (anaplastic glioma) or a Grade IV glioma (secondary GBM) [4]. Unfortunately, at the current time, there is a significant lack of diagnostic and prognostic biomarkers that are able to non-invasively assess MT and predict clinical outcome.

In 2009, Yan et al. discovered novel missense mutations in the *isocitrate dehydrogenase 1 & 2 (IDH1/2)* oncogenes, which are present in upwards of 70-80% of lesions that arise from low-grade lineage and conferred a significant survival advantage over wild-type tumors [5]. Interestingly, *IDH1/2* mutations were found to be conserved across mutually exclusive pathways of *TP53* mutation and 1p19q chromosomal loss and have been implicated as the earliest known mutation event in gliomagenesis [6]. Given the limited therapeutic options available for LGGs, *IDH*-mutations have garnered significant attention as a targetable therapeutic pathway with several novel therapies currently in development and testing in clinical trials [7-9].

The *IDH1/2* genes natively encode the isocitrate dehydrogenase (IDH) enzymes required for the decarboxylation of isocitrate to  $\alpha$ -ketoglutarate in several locations in the cell. The heterozygosity of *IDH*-mutations results in an amino-acid substitution at one of two enzymatic active sites, most commonly arginine to histidine, creating a wild-type and mutant heterodimer. The wild-type position continues the production of  $\alpha$ -ketoglutarate, while the mutant portion develops the gain-of-function ability to further convert  $\alpha$ -ketoglutarate to D-2-hydroxyglutarate (2HG), an otherwise scarce metabolite in normal cells [10]. 2HG accumulates to milli-molar concentrations in *IDH*-mutant tumors and has profound effects on the epigenetic landscape and processes within the cell [11].

High-resolution Magic Angle Spinning (HR-MAS) is a powerful spectroscopy technique

for interrogating the biochemical properties of tissue [12]. While 2HG is detectable using HR-MAS, it has proved to be a difficult biomarker *in vivo* owing to low signal-to-noise and significant overlap with neighboring metabolites at clinical field strengths. Given that metabolic differences have previously been shown to differentiate between cancer types and histological grades [13,14], it is hypothesized that there are differences in metabolite levels for lesions that have undergone MT, as well as those that contain the *IDH*-mutated genotype.

The objective of this study was to characterize the *ex vivo* metabolic profiles from patients previously diagnosed with an infiltrating glioma at the time of their recurrence,. The profiles obtained were related to findings from histological analysis of the tissue samples with respect to variations in tumor grade, histological subtype, and *IDH*-mutation status. The long term goal was to use the information obtained in order to design *in vivo* metabolic imaging methods that could improve the characterization of this disease, and provide biomarkers for non-invasive monitoring of disease progression for such patients.

## **Methods**

### ***Patient population***

This study was approved by the Institutional Review Board prior to patient recruitment and informed consent was obtained from each participating subject. A total of one hundred and twenty-six patients were included. Ninety patients had an initial diagnosis of WHO grade II glioma and were presenting for surgical resection owing to suspected recurrence, when MT is often observed. Thirty-six of the patients had newly diagnosed, non-enhancing lesions.

### ***Presurgical In vivo MR imaging and spectroscopy***

MR examinations were performed on either a 1.5 T or 3 T scanner (GE Healthcare Technologies) using an eight-channel phased-array headcoil (MRI Devices). Standard anatomical imaging included T<sub>2</sub>-weighted (FLuid Attenuated Inversion Recovery (FLAIR) and Fast Spin Echo (FSE)) as well as T<sub>1</sub>-weighted pre- and post-gadolinium contrast images. Diffusion Weighted Imaging (DWI) was obtained in the axial plane with 6 gradient directions and two-fold acceleration with sensitivity encoding parallel imaging [repetition time (TR)/echo time (TE) = 1000/108 ms, voxel size = 1.7 × 1.7 × 3 mm<sup>3</sup>, b = 1000 s/mm<sup>2</sup>]. Dynamic Susceptibility Contrast (DSC) Perfusion Weighted Imaging (PWI) was obtained with a 5ml/s bolus injection of 0.1mmol/kg body weight gadolinium diethyltriamine pentaacetic acid (Gd-DTPA) acquired using a series of T<sub>2</sub>\*-weighted echo-planar images [TR/TE/Flip-angle = 1250-1500/35-54 ms/30-35 degrees, 128 × 128 matrix, slice thickness = 3-5mm, 7-15 slices with 60-80 time points] before, during, and after injection. Lactate-edited 3D proton MR spectroscopic imaging (MRSI) was applied using point-resolved spectroscopic selection (PRESS) for volume localization and very selective saturation (VSS) pulses for lipid signal suppression [approximate excited volume = 80 × 80 × 40 mm<sup>3</sup>, TR/TE = 1104/144 ms, overpress factor = 1.5, field of view = 16 × 16 × 16 cm<sup>3</sup>, nominal voxel size = 1 × 1 × 1 cm<sup>3</sup>, flyback echo-planar readout gradient in the SI direction, 988 Hz sweep width and 712 dwell points] [15].

### ***Post processing of MR data***

The MR data were de-identified and transferred to a local Linux workstation. Software developed in house was applied to estimate relevant DWI, PWI, and MRSI parameters



and normalize between field strengths using estimates from Normal Appearing Brain Tissue (NABT). Maps of the normalized Apparent Diffusion Coefficient (ADC) were generated on a voxel-by-voxel basis according to a published algorithm [16]. Perfusion datasets were non-rigidly aligned using the VTK CISG software package [17]. Normalized Cerebral blood volume (CBV), percent  $\Delta R2^*$  signal recovery (%-REC),  $\Delta R2^*$  peak height (PH), and recirculation factor were calculated for each voxel using software developed by our lab. CBV intensities and PH parameters were obtained by fitting the dynamic perfusion data by a modified gamma-variate function with a recirculation parameter [18]. Peak height and percent recovery values were also estimated using a simplified nonparametric procedure [19].

Lactate-edited MRSI data were reconstructed and the signal from the individual channels combined to quantify total choline (tCho), N-acetyl-aspartate (NAA), creatine (Cr), lactate (Lac) and lipid (Lip) levels. The choline-to-N-acetyl-aspartate index (CNI) was generated from a linear regression based algorithm [20], which represents changes in choline and NAA levels compared to voxels in NABT. Imaging data were aligned to the post-Gadolinium  $T_1$ -weighted images using FMRIB's Linear Image Registration Tool (FLIRT). Anatomic imaging was resampled for overlay with DWI, PWI, and MRSI and the SIVIC software package was used to select target locations for intra-operative tissue sampling [21].

### ***Tissue sample acquisition***

Tissue sample targets were planned for each patient based on surgically accessible regions of abnormally decreased ADC, decreased %-REC and increased PH and CBV,

as well as elevated CNI, which are expected to represent viable, cellular regions of tumor with elevated proliferation and neovascularization. These locations were designated as 5-mm-diameter spherical targets on co-registered MR images using the surgical navigation software (BrainLAB Inc.). Intra-operative navigation guided the neurosurgeons to these designated locations and tissue samples were excised if it was possible to do so safely. Samples were immediately bisected with half being fixed in 10% zinc formalin, dehydrated by graded ethanols, and embedded in Paraplast Plus wax (McCormick Scientific) using standardized techniques for tissue processing and immunohistochemistry and the other half being snap-frozen in liquid nitrogen and stored at 80°C for <sup>1</sup>H HR-MAS.

### ***Histopathology and IDH-analysis***

Tissue samples were reviewed and scored for standard WHO criteria by a board-certified neuropathologist. Antibodies used in the assessment of the samples included rabbit polyclonal MIB-1 anti-Ki67 (30-9) (Ventana Medical Systems) at 2 µg/ml for 23 min at 37°C; mouse anti-SMI-31 (Covance) at 1.5 µg/ml for 8 min at 37°C; rabbit polyclonal Factor VIII (Dako) at 1.2 µg/ml for 20 min at 37°C; and mouse monoclonal anti-*IDH1*R132H (DIA H09) (Dianova) at 1:50 µg for 32 min at 37°C [22]. Heat antigen retrieval for MIB-1 was performed for 30 min in citrate buffer at pH 6. *IDH1*R132H and Factor VIII staining was performed in Tris-EDTA buffer at pH 8. Following antigen retrieval, sections were treated with 3% methanol-hydrogen peroxide for 16 min at 22°C. All immunohistochemistry assays were performed on the Ventana Medical Systems Benchmark XT.

Slides stained with H&E, MIB-1, SMI-31, and *IDH1*R132H were scored to assess histological characteristics. For the H&E-stained slides, a tumor score was given on the basis of the contribution of tumor cellularity to total cellularity. A score of 0 denoted neuropil without tumor; 1 indicated an infiltrating tumor margin containing detectable but not abundant—numbers of tumor cells; 2 denoted a more cellular-infiltrated zone; 3 denoted highly cellular tumor with few non-neoplastic cells. Tissue samples with a tumor score of 0 were excluded from analysis. Total cell-density was also determined as an average number of cells per 200x field. For MIB-1-stained slides, a labeling index [(MIB-1-positive nuclei per total tumor cells counted per 200x field) x 100%] was calculated based on the evaluation of at least three fields and >1000 cells. A score was generated by subdividing the labeling index according to approximate grade ranges for mitotic activity: 1 (<4); 2 (4-10); 3 (10-20); 4(>20). For SMI31- stained slides, a score was assigned to each slide on the basis of the extent of disruption of the normal axonal architecture. A score of 0 denoted no disruption; 1 denoted minimal disruption; 2 denoted mild disruption; 3 denoted severe disruption.

Microvascular morphology was graded based upon H&E staining and Factor VIII immunohistochemistry as delicate (resembling normal cerebral vessels), simple vascular hyperplasia (circumferential hyperplasia with definitive lumen), or complex microvascular hyperplasia (glomeruloid-type vessels). An overall score for each vascular component (delicate, simple vascular hyperplasia, and complex microvascular hyperplasia) based on Factor VIII was derived from its relative contribution to total vascularity using a four-tier ordinal scale (0, no contribution; 1, minimal; 2, prevalent; 3, extensive) at a magnification of 200x. A sum of Factor VIII score across all vascular components was

calculated as a measure of total extent of vascularization. Digital images were captured using a microscope (Olympus, Model BX41TF) and digital camera (Olympus, Model DP70). Continuous values of cell density were converted into an ordinal scale defined as the following: 0 = 0-100 cells/field, 1 = 100-200 cells/field, 2 = 200-400 cells/field, 3 = 300-400 cells/field.

### ***Ex vivo HR-MAS spectroscopy***

Image-guided tissue samples were loaded into a 35-ml zirconia rotor (custom-designed by Varian) with 3 ml of 99.9% atom-D deuterium oxide containing 0.75 wt % 3-(trimethylsilyl)propionic acid (Sigma-Aldrich) for chemical shift referencing. Data were acquired at 11.7 T, 1°C, 2250 Hz spin rate in a 4-mm gHX nanoprobe with a Varian INOVA 500 MHz multinuclear spectrometer. The nanoprobe gHX is an inverse probe, optimized for the direct detection of protons and the indirect detection of X-nuclei ( $^{13}\text{C}$ ,  $^{31}\text{P}$ ,  $^{15}\text{N}$ ) and was equipped with a magic angle gradient coil. A rotor-synchronized T2-weighted Carr-Purcell-Meiboom-Gill (CPMG) [23] pulse sequence was chosen for its ability to eliminate broad macromolecular signals, and run with a TR/TE = (4 s)/(144 ms), 512 scans, 40,000 acquired points, 90° pulse, and 20 kHz spectral width for a total time of 35 min.

Preprocessing of HR-MAS spectra was done in the time domain using the Java-based magnetic resonance user interface (jMRUI) [24]. Data was normalized by tissue sample weight and quantification of relative 1D metabolite levels was achieved with the semi-parametric algorithm HR-QUEST, which fits a customized basis set of metabolites to a given spectrum [25]. The HR-QUEST basis set used in this study was composed of spectra from 27 metabolites that are commonly studied in human brain tumors.

Metabolite levels with less than 13% Cramer-Rao error estimates were included for statistical analysis. Spectral averages were produced using in house algorithms that frequency-shifted each post-processed spectrum and normalized by tissue size. Two experienced spectroscopists evaluated each spectrum to qualitatively assess goodness of metabolite fits, the presence of 2HG levels, and whether low resolution or SNR compromised its analysis. Patients were treated as entirely *IDH*-mutated if 2HG was determined to be present in any tissue sample or if immunohistochemistry for *IDH1R132H* was positive. This reduced the risk of false-negatives based on the other mutational variants of *IDH1* and *IDH2*.

### ***Heatmap generation***

A spectral heatmap was generated from the HR-MAS data using the following procedure: each metabolite was normalized by the 90<sup>th</sup>-percentile for relative visualization, the tissue samples were categorized by grade, the data were imported into Gitools version 2.2.1 ([www.gitools.org](http://www.gitools.org)) [26] and a linear, hierarchical clustering algorithm was performed at the tissue sample level.

### ***Statistical Analysis***

All statistical testing was performed in R (version 3.1.2). Mixed effect modeling was used to determine the significant differences in measured metabolite values among groups that had undergone MT versus those that had not, as well as by *IDH*-mutation status. Measured metabolite levels were iteratively used as predictors for a binary outcome in the mixed effect model and accounted for clustering of observations by biopsy event. Odds ratios and Wald statistic *p* values were reported together with a 95% confidence

interval for each metabolite and group comparison.

The Kendall tau rank correlation test was used to assess the pair-wise correlations between 2HG levels and other metabolites. In order to address the clustering of observations by biopsy event, each correlation was run fifty times with a random iterative selection of patient samples. The mean and standard deviation of the Tau estimates were reported with the median  $p$  value of all tests. Non-corrected correlations were also reported. In all cases, a Bonferroni alpha-correction was used in assessing statistical significance.

## **Results**

### ***Characterization of the patient population***

A summary of the patient population is presented in Table 5.1. There were 162 tissue samples from the 90 patients who presented at the time of suspected disease recurrence and 57 tissue samples from the 36 patients who had non-enhancing, newly diagnosed WHO Grade II or WHO Grade III glioma. Fifty-one percent of the population was found to have undergone MT and forty-nine percent remained Grade II. The majority of the patients (108 patients, 88%) were found to harbor *IDH*-mutations. These lesions were distributed across all histological subtypes, including 52 patients with an astrocytoma (AS), 44 patients with an oligodendroglioma (OD), and 30 patients with a mixed oligoastrocytoma (OA).

### ***Metabolic differences associated with MT and IDH-mutation***

There was a significant elevation of several metabolites in samples from lesions that had

undergone MT. The magnitude of the observed differences varied based on tumor grade and histological subtype as presented in Figure 5.1. Lesions that had undergone MT displayed statistically significant elevations of phosphocholine (PC) and total choline (tCho). Elevated levels of taurine (Tau) were found to be associated with Grade III and Grade IV lesions, and elevated levels of hypo-taurine (hTau) with Grade IV. Increased glycine (Gly), glutamate (Glu), glutathione (GSH), alanine (Ala), aspartate (Asp), and betaine (Bet) were found to be significantly elevated in lesions that had undergone MT to Grade IV compared with all other grades, while glutamine (Gln), glucose (Glc) were increased in Grade IV tumors when compared to Grade II lesions. 2HG levels were elevated in Grade IV lesions across all histologies. *IDH*-mutated lesions were found to have increased levels of 2HG and decreased levels of Glu. Figure 5.2 presents averaged spectra for Grade II and III lesions (A), Grade III and IV (B), as well as *IDH*-mutated versus wild-type tumors. A spectral heatmap produced from the dataset is presented in Figure 5.3, and displays normalized spectral intensities across all tissue samples. Intra-grade clustering provided visualization of the entire population and distribution of metabolite levels in individual samples.

When assessed by AS or OD histological subtype, there were distinct differences in MT for each tumor type. Anaplastic ASs displayed marked elevations of PC and free choline (Cho), while anaplastic ODs displayed elevations of glycerophospholine (GPC). In AS lesions, increased phosphoethanolamine (PE) and Gln was observed in Grade III versus Grade II lesions, while elevated Glutamate was observed in Grade IV tumors. 2HG was found to be elevated in Grade IV astrocytoma lesions and Grade III oligodendrogliomas. Other metabolites that were increased in anaplastic OD included Tau, Gly, Gln, and Bet. Supplementary Figure 5.2 presents differences between AS and OD histological types in Grade II and III lesions. In OD tumors, there was elevated PC and Cho in Grade II samples, increased 2HG and GPC in Grade III samples, and elevated Eth when Grade II and III samples were combined. Mixed oligoastrocytomas were excluded from histological subtype analysis due to the uncertainty in how to classify them.

Grade	Total patients (samples)	IDH-wt (samples)	IDH-mut (samples)	IDH-uncertain (samples)
All	126 (219)	15 (26)	108 (190)	3 (3)
II	62 (103)	10 (16)	50 (85)	2 (2)
III	50 (89)	2 (4)	47 (84)	1 (1)
IV	14 (27)	3 (6)	11 (21)	—
AS	52 (83)	8 (12)	42 (69)	2 (2)
OA	30 (57)	5 (10)	24 (46)	1 (1)
OD	44 (79)	2 (4)	42 (75)	—

**Table 5.1 Recurrent LGG patient and tissue sample population by grade, histological subtype, and IDH-mutation status.** The patient population comprised astrocytoma, oligodendroglioma, and oligoastrocytoma histological subtypes. The majority of patients (88%) patients harbored IDH-mutant lesions and at the time of recurrence and 64 patients (51%) had undergone MT. It is of note that 10 patients were scanned at two distinct recurrences



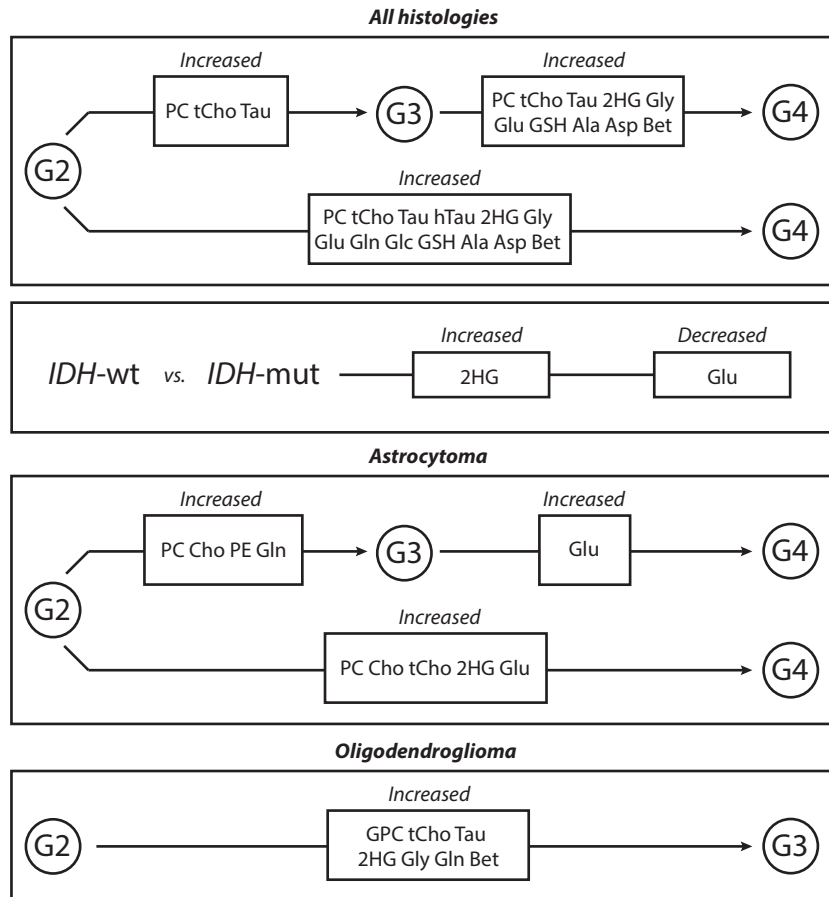


**Figure 5.1 Flow diagram of metabolite differences associated with MT and *IDH*-mutation status.** Here we present the metabolic differences associated with malignant transformation found across all histologies, as well as within individual astrocytoma and oligodendroglioma subtypes. We found significant elevations in several metabolite levels in tumors that had undergone MT versus those that did not, as well as elevations in 2HG and decreases in Glu in lesions that harbored *IDH*-mutations.

**Correlation of 2HG with metabolite levels and histopathology parameters**

Given that the study population was primarily *IDH*-mutated, this provided a unique opportunity to investigate correlations of 2HG levels with other brain tumor metabolites

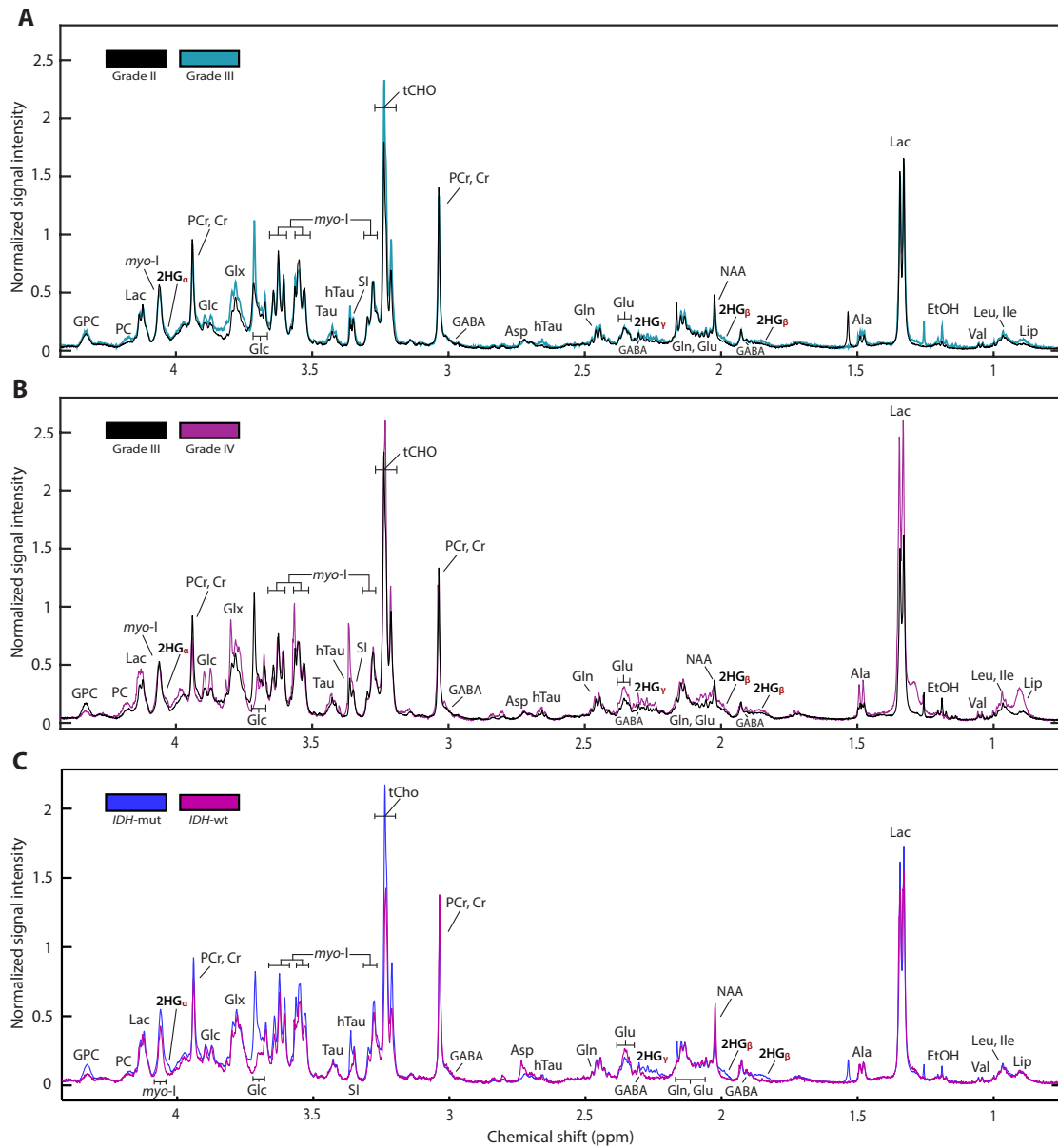


**Figure 5.2 Averaged HR-MAS spectral profile from individual histological grades and *IDH*-mutation status.** We normalized by tissue weight and produced an averaged spectrum at the tissue sample level for individual grades and *IDH*-genotypes. Spectral profiles demonstrate elevations in metabolites associated with MT (A and B), as well as increases in 2HG and decreases in Glu associated with *IDH*-mutation (C).

and histopathology parameters in these tumors. These results are presented in Table 5.2 and Supplementary Figure 5.2. There were positive correlations of 2HG levels and all of the choline-containing compounds (Cho, GPC, PC, and tCho), PE, GSH, Tau, hTau, Glu, Gln, Asp, Ala, myo-I, SI, GABA, PCr/Cr, Gly, Bet, and Thr. In addition, there were correlations with 2HG levels and mitotic activity as measured by MIB1 antibody

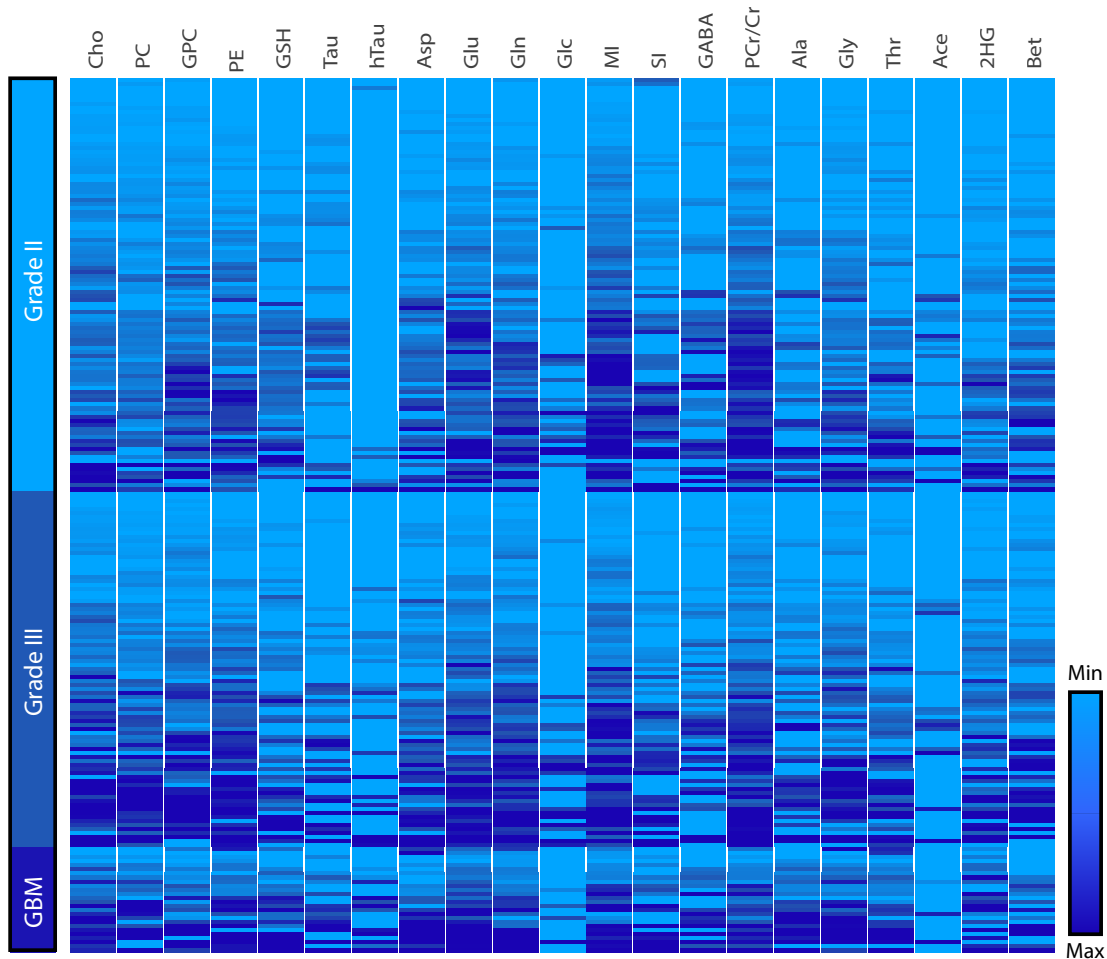


**Figure 5.3 Metabolic spectral heatmap across histological grades.** The heatmap was generated from the HR-QUEST quantification of individual tissue sample spectra (rows) and organized by metabolite (columns). Data were normalized by the 90<sup>th</sup>-percentile across columns and hierarchically clustered within each grade providing comprehensive visualization of the entire dataset and distribution of metabolite levels across histological grades. We observed intra-patient heterogeneity of tissue samples, as well as the global elevation in the key metabolites associated with MT.

staining. No other histopathology measurements were significantly correlated with 2HG.

Variable correlated	Number of samples	Regression Coefficient	<i>p</i> value
<b>Ex vivo metabolites</b>			
Cho	115	0.098	<i>p</i> < 0.001
GPC	121	0.16	<i>p</i> < 0.001
PC	111	0.15	<i>p</i> < 0.001
tCho	126	0.098	<i>p</i> < 0.001
PE	108	0.15	<i>p</i> < 0.001
GSH	83	0.27	<i>p</i> < 0.001
Tau	57	0.31	<i>p</i> < 0.001
hTau	35	4.0	<i>p</i> = 0.006
Glu	118	0.087	<i>p</i> < 0.001
Gln	115	0.12	<i>p</i> < 0.001
Asp	85	0.11	<i>p</i> < 0.001
Ala	66	0.15	<i>p</i> = 0.009
myo-I	125	0.041	<i>p</i> < 0.001
SI	74	0.67	<i>p</i> < 0.001
GABA	53	1.7	<i>p</i> = 0.001
PCr / Cr	126	0.1	<i>p</i> < 0.001
Gly	104	0.095	<i>p</i> < 0.001
Bet	83	5.5	<i>p</i> < 0.001
Thr	90	0.31	<i>p</i> < 0.001
<b>Histopathology parameters</b>			
Mitosis (MIB1)	99	0.00018	<i>p</i> < 0.001

**Table 5.2 Metabolite and histopathology correlations with 2HG levels.** Each of the study parameters correlated with 2HG is presented. This statistical method used was a Kendall correlation test with a *p* value cutoff of *p* < 0.05. Here we present the correlated parameters with their associated number of tested pairs, regression coefficients, and *p* values.

### **Discussion**

This study found that there were distinctive metabolic profiles in gliomas that had undergone malignant transformation and in *IDH*-mutated compared to *IDH*-wild-type gliomas. Several metabolites including the cholines, glutamate, and glutamine were also found to be correlated with levels of 2HG and with histopathological parameters. The results obtained provide improved characterization of the metabolic pathways in these lesions and, given that many of these metabolites are measurable *in vivo*, may allow for

improved monitoring and diagnosis of patients in a clinical setting.

When considering all histological subtypes, choline-containing compounds were found to be elevated in transformed lesions. Previous studies in our group have shown increases in PC associated with Grade III and Grade IV lesions [13]. These results show that tCho is also elevated and could be an *in vivo* biomarker for MT. The association of AS lesions with PC and Cho, and of OD lesions with GPC, may reflect alterations in the phospholipid metabolism found in the choline kinase pathway for the individual subtypes.

Increases in Glu and Gln that were associated with transformation to GBM may be a product of elevated glutaminolysis, which leads to the subsequent production of alanine and aspartate [28]. Considering that Glu, Gln, Ala, and Asp were elevated in Grade IV lesions, it may also be possible to detect such changes in the corresponding *in vivo* spectral profiles. The recent development of hyperpolarized  $^{13}\text{C}$  spectroscopic imaging [29] may also be of interest for interrogating this pathway.

The production of reactive oxygen species (ROS) promotes genomic instability in tumors. Glutathione is one of several molecules involved in eliminating ROS. While its role in brain tumors remains to be elucidated, it may play a role in therapy sensitivity and resistance [30]. Increased production of GSH found in the current study may be linked to the increased oxidative stress, dysregulation of the GSH pathway, or treatment related changes.

Glycine and other amino-acid metabolites have been previously reported to be elevated in Grade IV lesions [31], and are consistent with the demands for nucleotide synthesis present in highly proliferative cells. The results of this study corroborate the prior data and further demonstrate significantly elevated Gly in anaplastic oligodendrogliomas. As

this metabolite is measurable using *in vivo* techniques, Gly may be able to serve as a biomarker for MT in glial tumors.

The elevation of 2HG in *IDH*-mutated lesions was observed in previous studies [32-34]. Given the equilibrium between alpha-ketoglurate and glutamate, it has been predicted that there would be a decrease in glutamate, but it has been difficult to assess this using *in vivo* methods. The results from the current study confirm that there are reductions in glutamate in *IDH*-mutated lesions, which is likely depleted as a result of altered metabolism. Interestingly, the correlation between 2HG levels and mitotic activity is suggestive of increasing cellularity being associated with the production of 2HG.

There is a clear need for diagnostic and treatment biomarkers for the *IDH*-pathway that can keep pace with the development of novel therapies. While measuring 2HG using spectroscopic techniques *in vivo* would likely provide the most specific marker for these lesions, the clinical development of such sequences is still under investigation. While the approaches presented so far are promising, achieving the necessary signal-to-noise and reliably resolving 2HG from overlapping metabolites may be difficult at clinical field strengths. There are also likely to be issues in the case of residual disease, where the tumor volume may be too low to provide an accurate measurement. Given these constraints, surrogate markers for 2HG levels such as those presented in this study should also be investigated.

The ultimate goal of this work is to improve the clinical management of patients with glioma. The spectral profiles obtained in this study may aid in developing non-invasive MRSI methods to better diagnose and monitor patients based on underlying tumor metabolism, and further characterize the *IDH*-mutated molecular subtype. Most

importantly, it is hoped that this study will lead to improved outcome and quality of life for these patients.

## **References**

- [1] Riemenschneider MJ, Reifenberger G. Molecular neuropathology of low-grade gliomas and its clinical impact. *Adv Tech Stand Neurosurg.* 2010; 35:35–64.
- [2] Young RM, Jamshidi A, Davis G, Sherman JH. Current trends in the surgical management and treatment of adult glioblastoma. *Ann Transl Med.* 2015; 3: 121
- [3] Claus EB, Walsh KM, Wiencke JK, Molinaro AM, Wiemels JL, Schildkraut JM, Bondy ML, Berger M, Jenkins R, Wrensch M. Survival and low-grade glioma: the emergence of genetic information. *Neurosurg Focus.* 2015. 38, E6
- [4] Grier JT, Batchelor T. Low-grade gliomas in adults. *Oncologist.* 2006; 11:681–693.
- [5] Yan H, Parsons DW, Jin G, McLendon R, Rasheed BA, Yuan W, et al. IDH1 and IDH2 mutations in gliomas. *N Engl J Med.* 2009; 360: 765–73.
- [10] H.E. Leeper, A. A. Caron, P. A. Decker, R. B. Jenkins, D. H. Lachance, C. Giannini. IDH mutation, 1p19q codeletion and ATRX loss in WHO grade II gliomas. *Oncotarget,* (2015).
- [7] Rohle D, Popovici-Muller J, Palaskas N, Turcan S, Grommes C, Campos C, et al. An Inhibitor of Mutant IDH1 Delays Growth and Promotes Differentiation of Glioma Cells. *Science.* 2013: 340 (6132): 626-630
- [8] Turcan S, Fabius AW, Borodovsky A, Pedraza A, Brennan C, Huse J, et al. Efficient induction of differentiation and growth inhibition in IDH1 mutant glioma cells by the DNMT Inhibitor Decitabine. *Oncotarget.* 2013; 4(10):1729-36.
- [9] Yen KE, Bittinger MA, Su SM, Fantin VR. Cancer-associated IDH mutations: biomarker and therapeutic opportunities. *Oncogene.* 2010; 29(49):6409-17.

- [10] Dang L, White DW, Gross S, Bennett BD, Bittinger MA, Driggers EM, et al. Cancer-associated IDH1 mutations produce 2-hydroxyglutarate. *Nature*. 2009; 462:739–744.
- [11] Turcan S, Rohle D, Goenka A, Walsh LA, Fang F, Yilmaz E, et al. IDH1 mutation is sufficient to establish the glioma hypermethylator phenotype. *Nature*. 2012; 483:479-83
- [12] Andrew ER, Bradbury A, Eades RG. Nuclear magnetic resonance spectra from a crystal rotated at high speed. *Nature*. 1958; 182:1659
- [13] Elkhaled A, Jalbert L, Constantin A, Yoshihara HA, Phillips JJ, Molinaro AM, et al. Characterization of metabolites in infiltrating gliomas using ex vivo <sup>1</sup>H high-resolution magic angle spinning spectroscopy. *NMR Biomed*. 2014 May; 27:578-93.
- [14] Tessem MB, Swanson MG, Keshari KR, Albers MJ, Joun D, Tabatabai ZL, et al. Evaluation of lactate and alanine as metabolic biomarkers of prostate cancer using <sup>1</sup>H HR-MAS spectroscopy of biopsy tissues. *Magn Reson Med*. 2008; 60(3):510-6
- [15] Park I, Chen AP, Zierhut ML, Ozturk-Isik E, Vigneron DB, Nelson SJ. Implementation of 3T lactate-edited 3D <sup>1</sup>H MR spectroscopic imaging with flyback echo-planar readout for gliomas patients. *Ann Biomed Eng*. 2011; 39:193–204.
- [16] Basser PJ, Pierpaoli C. Microstructural and physiological features of tissues elucidated by quantitative-diffusion-tensor MRI. *J Magn Reson*. 1996; 111:209–19.
- [17] Hartkens T, Rueckert D, Schnabel JA, Hawkes DJ, Hill DLG. VTK CISG Registration Toolkit: An open source software package for affine and non-rigid registration of single- and multimodal 3D images. *BVM* Leipzig, Germany, Springer-Verlag 2002; 185.
- [18] Lee MC, Cha S, Chang SM, Nelson SJ. Dynamic susceptibility contrast perfusion imaging of radiation effects in normal-appearing brain tissue: changes in the first-pass and recirculation phases. *J Magn Reson Imaging*. 2005; 21:683–93.



- [19] Lupo JM, Cha S, Chang SM, Nelson SJ. Dynamic susceptibility weighted perfusion imaging of high-grade gliomas: characterization of spatial heterogeneity. *Am J Neuroradiol.* 2005; 26:1446–54.
- [20] Li Y, Lupo JM, Parvataneni R, Lamborn KR, Cha S, Chang SM, et al. Survival analysis in patients with newly diagnosed glioblastoma using pre- and postradiotherapy MR spectroscopic imaging. *J Neurooncol.* 2013; 15(5):607-617.
- [21] Crane JC, Olson MP, Nelson SJ (2013) SIVIC: Open-Source, Standards-Based Software for DICOM MR Spectroscopy Workflows. *Int J Biomed Imaging.* 2013: 169526–12. doi:10.1155/2013/169526.
- [22] Capper D, Zentgraf H, Balss J, Hartmann C, Von Deimling A. Monoclonal antibody specific for IDH1 R132H mutation. *Acta Neuropathol.* 2009; 118: 599–601.
- [23] Meiboom S, Gill D. Modified spin-echo method for measuring nuclear relaxation times. *Rev Sci Instrum.* 1958; 29:688-691
- [24] Stefan D, Di Cesare F, Andrasescu A, Popa E, Lazariev A, Vescovo E, Strbak O, Williams S, Starcuk Z, Cabanas M, Van Ormondt D, Graveron-Demily D. Quantification of magnetic resonance spectroscopy signals: the jMRUI software package. *Meas Sci Technol.* 2009; 20: 104035
- [25] Ratiney H, Albers MJ, Rabeson H, Kurhanewicz J. Semi-parametric time-domain quantification of HR-MAS data from prostate tissue. *NMR Biomed.* 2010; 23(10): 1146-1157
- [26] Perez-Llamas C, Lopez-Bigas N. Gitools: Analysis and Visualisation of Genomic Data Using Interactive Heat-Maps. *PLoS ONE.* 2011; 6.
- [27] R Core Team. R: A language and environment for statistical computing. R Foundation for Statistical Computing. 2013 ISBN 3-900051-07-0
- [28] Marie SKN, Shinjo SMO. Metabolism and Brain Cancer. *Clinics.* 2011; 66:33-43

- [29] Chaumeil MM, Larson PE, Woods SM, Cai L, Eriksson P, Robinson AE, Lupo JM, Vigneron DB, Nelson SJ, Pieper RO, Phillips JJ, Ronen SM. *Cancer Res.* 2014; 74(16):4247-57
- [30] Backos DS, Franklin CC, Reigan P. The role of glutathione in brain tumor drug resistance. *Biochem Pharmacol.* 2012; 83(8):1005-12
- [31] Chinnaiyan P, Kensicki E, Bloom G, Prabhu A, Sarcar B, Kahali S, Eschrich S, Qu X, Forsyth P, Gillies R. The metabolomics signature of malignant glioma reflects accelerated anabolic metabolism. *Cancer Res.* 2012; 72(22):5878-88
- [32] Elkhaled A, Jalbert LE, Phillips JJ, Yoshihara HA, Parvataneni R, Srinivasan R, Bourne G, Berger MS, Chang SM, Cha S, Nelson SJ. Magnetic resonance of 2-hydroxyglutarate in IDH1-mutated low-grade gliomas. *Sci Transl Med.* 2012; 4(116):116ra5
- [33] Andronesi OC, Kim GS, Gerstner E, Batchelor T, Tzika AA, Fantin VR, Vander Heiden MG, Sorensen AG. Detection of 2-hydroxyglutarate in IDH-mutated glioma patients by in vivo spectral-editing and 2D correlation magnetic resonance spectroscopy. *Sci Transl Med.* 2012; 4(116):116ra4
- [34] Choi C, Ganji SK, DeBerardinis RJ, Hatanpaa KJ, Rakheja D, Kovacs Z, Yang XL, Mashimo T, Raisanen JM, Marin-Valencia I, et al. *Nat Med.* 2012; 18(4):624-9

### **Acknowledgements**

We would like to acknowledge support from the Brain Tumor Research Center at UCSF in collecting and analyzing the tissue samples, as well as from staff in the Margaret Hart Surbeck Laboratory for Advanced Imaging. We would particularly like to express our

gratitude to S. Ronen, D. Vigneron, and J. Crane for their technical assistance and guidance during this project.

### **Funding sources**

This work was supported as a project in the NCI Brain Tumor SPORE grant, number P50CA097257.

### **Supplementary Figure Captions**

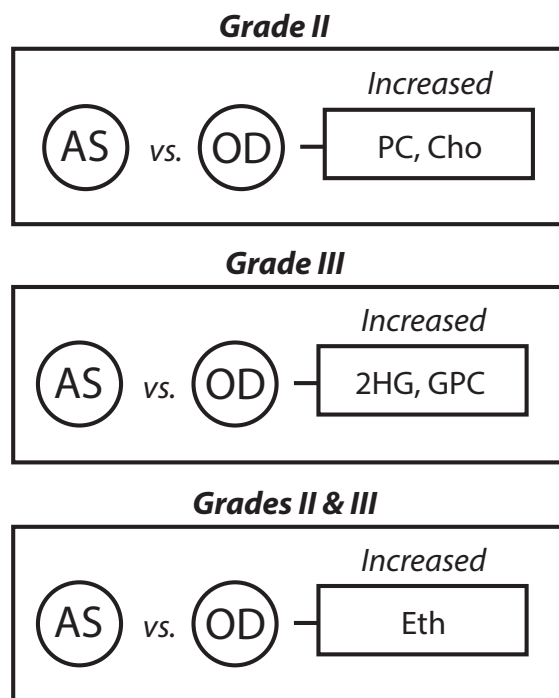
**Supplementary Figure 5.S1 Flow diagram of metabolite differences between astrocytoma and oligodendroglioma subtypes within histological grades.** When compared within each histological grade, we observed several metabolites that were elevated in oligodendroglial lesions when compared with astrocytomas.

Oligoastrocytomas were excluded from this comparison. These included PC and Cho (Grade II), 2HG and GPC (Grade III), and Eth (Grades II and III combined).

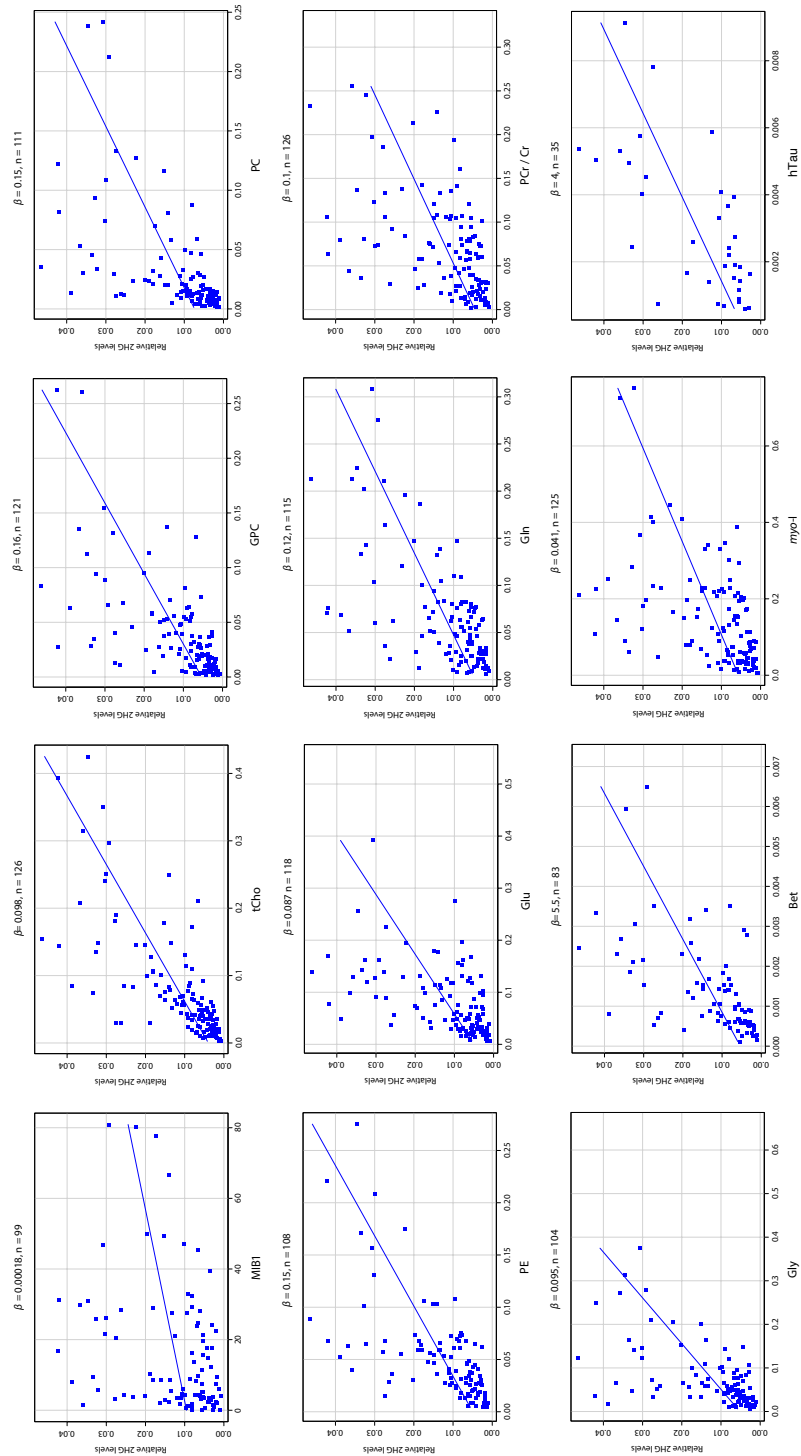
**Supplementary Figure 5.S2 Correlation scatterplots of 2HG levels with other metabolites and histopathological measures.** A Kendall's tau correlation test was performed to assess the strength of the relationship between 2HG levels and other metabolite levels and histopathology scores. We found significant correlation between 2HG levels and mitosis as measured by the MIB-1 antibody. We additionally found several metabolites that were correlated with 2HG levels and are presented here and in Table 2.

**Supplementary Figures**

**Supplementary Figure 5.S1 Flow diagram of metabolite differences between astrocytoma and oligodendroglioma subtypes within histological grades.**



**Supplementary Figure 5.S2 Correlation scatterplots of 2HG levels with other metabolites and histopathological measures.**



## Chapter 6: Summary

---

Advances in non-invasive imaging are critically needed in order to keep pace with progress in the cancer research field. This is especially true for infiltrating gliomas, where clinical management requires the ability to better diagnose distinct molecular subtypes and rapidly monitor physiological changes in tumor aggressiveness. The goal of this dissertation project was to develop and apply advanced physiological imaging techniques to enhance our understanding of this devastating disease, and provide valuable biomarkers and metabolic information that can be used for improved patient care.

This work supports integration of metabolic spectroscopic imaging into standard clinical exams as well as utilization in a research setting to better characterize this disease. Magnetic resonance spectroscopy provides a feasible method of non-invasive genotyping of *IDH*-mutations, and although preliminary in nature, several approaches are currently being tested at clinical research institutions. The results of this dissertation encourage the use of MR spectroscopy to enhance our ability to diagnose *IDH*-mutations and stratify patients to the most appropriate treatment regimens.

These projects further highlight the ability to assess malignant transformation using advanced *in vivo* and *ex vivo* MR spectroscopy techniques. The volumetric and intensity imaging findings shed new light on the imaging features of recurrent glioma, and the

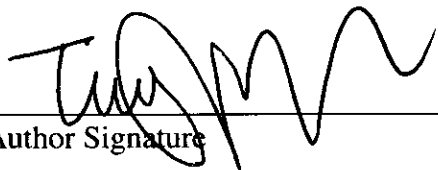
distinct spectral profiles found in these studies may allow for the development of novel *in vivo* methodology to aid in the clinical management of these patients. Taken together, these results may ultimately provide additional information as to the grade, histological subtype, and genotype of a glioma, and could allow for more informed treatment decisions and improved outcome and quality of life for these patients.

**Publishing Agreement**

*It is the policy of the University to encourage the distribution of all theses, dissertations, and manuscripts. Copies of all UCSF theses, dissertations, and manuscripts will be routed to the library via the Graduate Division. The library will make all theses, dissertations, and manuscripts accessible to the public and will preserve these to the best of their abilities, in perpetuity.*

***Please sign the following statement:***

*I hereby grant permission to the Graduate Division of the University of California, San Francisco to release copies of my thesis, dissertation, or manuscript to the Campus Library to provide access and preservation, in whole or in part, in perpetuity.*

  
\_\_\_\_\_  
Author Signature

11/30/15  
\_\_\_\_\_  
Date